

CSDL-T-1083**MULTIVARIABLE CONTROL OF THE
SPACE SHUTTLE REMOTE
MANIPULATOR SYSTEM USING
H₂ AND H_∞ OPTIMIZATION****by
Om Prakash II****May 1991****Master of Science Thesis
Massachusetts Institute of Technology**

(NASA-CR-105661) MULTIVARIABLE CONTROL OF
THE SPACE SHUTTLE REMOTE MANIPULATOR SYSTEM
USING H₂ AND H(INFINITY) OPTIMIZATION M.S.
Thesis - Massachusetts Inst. of Tech.
(Draper (Charles Stark) Lab.) 119 pCSCL 131 63/37

901-87450

Unclass
0019379

The Charles Stark Draper Laboratory, Inc.
555 Technology Square, Cambridge, Massachusetts 02139-3563

Multivariable Control of the Space Shuttle Remote Manipulator System Using H_2 and H_∞ Optimization

by

Om Prakash II

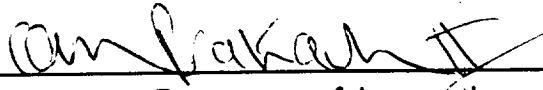
B.S., Engineering Sciences,
United States Air Force Academy
(1989)

SUBMITTED TO THE DEPARTMENT OF AERONAUTICS AND
ASTRONAUTICS IN PARTIAL FULFILLMENT OF THE
REQUIREMENTS FOR THE DEGREE OF

MASTER OF SCIENCE
at the
MASSACHUSETTS INSTITUTE OF TECHNOLOGY
May, 1991

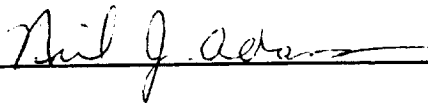
© Om Prakash II, 1991. All rights reserved.

Signature of Author _____



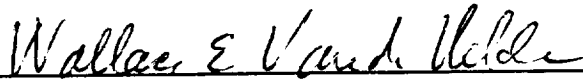
Department of Aeronautics and Astronautics
May, 1991

Certified by _____



Neil J. Adams
Technical Staff, C. S. Draper Labs
Technical Supervisor

Certified by _____



Wallace E. VanderVelde
Professor of Aeronautics and Astronautics
Thesis Supervisor

Accepted by _____

Professor Harold Y. Wachman
Chairman, Departmental Graduate Committee

Multivariable Control of the Space Shuttle Remote Manipulator System Using H_2 and H_∞ Optimization

by

Om Prakash II

Submitted to the Department of Aeronautics and
Astronautics on May 10, 1991 in partial fulfillment of the
requirements for the degree of Master of Science

Abstract

Three linear controllers are designed to regulate the end effector of the Space Shuttle Remote Manipulator System (SRMS) operating in Position Hold Mode. In this mode of operation, jet firings of the Orbiter can be treated as disturbances while the controller tries to keep the end effector stationary in an Orbiter-fixed reference frame. The three design techniques used include: the Linear Quadratic Regulator (LQR), H_2 optimization, and H_∞ optimization.

The nonlinear SRMS is linearized by modelling the effects of the significant nonlinearities as uncertain parameters. Each regulator design is evaluated for robust stability in light of the parametric uncertainties using both the small gain theorem with an H_∞ norm and the less conservative μ -analysis test.

All three regulator designs offer significant improvement over the current system on the nominal plant. Unfortunately, even after dropping performance requirements and designing exclusively for robust stability, robust stability cannot be achieved. The SRMS suffers from lightly damped poles with real parametric uncertainties. Such a system renders the μ -analysis test, which allows for complex perturbations, too conservative.

Technical Supervisor: Neil J. Adams
Technical Staff, Manned Space Systems Division,
The Charles Stark Draper Laboratory, Inc.

Thesis Supervisor: Dr. Wallace E. VanderVelde
Professor of Aeronautics and Astronautics

Acknowledgements

An ocean of patience, a mountain of insight,
Captains a craft through the storm, guides the ornithopter through the night.
The chaos of my thoughts you ordered with ease,
And extracted a thesis as effortless as a breeze.
Neil I am grateful and in your debt will always be,
And I truly understand why you're the star of EGC.

Amazed at the circus, my mouth open wide,
As the trapeze artist casts gravity aside,
And the great Nabakov with his mastery of words,
Or the mighty strokes of Mozart as he conjures the chords.
The hard work and dedication that these Masters represent,
Is personified in Controls by the Oracle, or Brent.

Take the legendary Conan and a Trumpful of greed,
Be liberal with cynicism, and some virtuosity you'll need.
Combine all of these things with generous portions of heart,
And you'll come up with Naz, at least in part.

Thanks Professor VanderVelde for your careful reading and valuable suggestions,
And Don's 'divide by 12' answered many of my questions.

Dave I reserve a special place for you,
Full of honest ideals and compassion too.
So don't harass my friend or get on his case,
Dave knows it's not the kill, but the thrill of the chase.

Though you may not realize, I know to be true,
That the Odyssey is about Scott, and the Illiad too.
But I hope you remember even Odysseus came back,
And scattered the suitors by piercing many an ax.

Ching, Bill, Karl, Noel, Kris and Steve,
From your company I sadly take my leave:
"HOTMOKD SD, WJ GO KOSRLAYTY NOWJ SR KOSD."

Answers in seclusion have insignificant tangible extensions,
Resist until you understand mankind's intentions.

From my parents flows my body, and from Dharma my mind,
Though it is western religions that put time on a line,
So to express my gratitude during this short sojourn on Earth,
I try to apply my abilities to the best of their worth.

This report was prepared at the Charles Stark Draper Laboratory, Inc. under contract NAS9-18147.

Publication of this report does not constitute approval by the Draper Laboratory or the sponsoring agency of the findings or conclusions contained herein. It is published solely for the exchange and simulation of ideas.

I hereby assign my copyright of this thesis to the Charles Stark Draper Laboratory, Inc., Cambridge, Massachusetts.

Contents

1	Introduction	13
2	Description of the Shuttle Remote Manipulator System	18
2.1	Physical Description	19
2.2	SRMS Control Modes	21
2.3	Position Hold	22
3	Modelling the SRMS	25
3.1	Equations of Motion for the Orbiter/SRMS/Payload System	27
3.1.1	Equations of Motion for the Single Joint Case	27
3.1.2	Equations of Motion for the Six Joint Case	30
3.2	Modelling and Linearization of the Control Servos	32
3.2.1	Control Servo Dynamics	32
3.2.2	Representing the Uncertainties	37
3.3	Comparison of the Linear and Nonlinear Plant	42
3.4	Conclusions	46
4	Design and Analysis Approach	49
4.1	Obtaining a Design Plant	50
4.1.1	Model Reduction	52
4.1.2	Characteristics of the ROM	54
4.2	Analysis Techniques and the Open-Loop Plant	57
4.2.1	Performance	59
4.2.2	Control Effort	59

4.2.3	Stability Robustness	61
4.3	Summary	68
5	LQR Design	69
5.1	LQR Theory	69
5.2	LQR Results	72
5.2.1	LQR Control Effort and Performance	72
5.2.2	LQR Stability Robustness	77
5.3	Summary	79
6	H_2 Design	80
6.1	H_2 Theory	81
6.2	H_2 Results	86
6.2.1	H_2 Control Effort and Performance	86
6.2.2	H_2 Stability Robustness	89
6.3	Summary	95
7	H_∞ Design	96
7.1	H_∞ Theory	97
7.2	H_∞ Results	100
7.2.1	H_∞ Control Effort and Performance	100
7.2.2	H_∞ Stability Robustness	104
7.3	Summary	115
8	Conclusions	116

List of Figures

1.1	Cumulative SRMS Damping Time	14
2.1	Shuttle Remote Manipulator System	19
2.2	Mechanical Arm Assembly	20
2.3	Typical SRMS Maneuver Profile	23
3.1	Block Diagram of the Compensated System	26
3.2	One Joint Illustration: Point Mass on a Massless Flexible Beam	28
3.3	Draper Servo Model	33
3.4	Linearized Servo Model	35
3.5	Linearized SRMS Model	36
3.6	Gearbox Stiffness Curve	38
3.7	Current Limiter	39
3.8	Standard Form for a Compensated Plant with Uncertainty	41
3.9	SSAD in Position Hold	43
3.10	Translation Response of LSAD and Nominal SSAD to an Initial Velocity	44
3.11	Rotational Response of LSAD and Nominal SSAD to an Initial Velocity	45
3.12	Translation Response of LSAD and off-nominal SSAD to an Initial Velocity	47
3.13	Rotational Response of LSAD and off-nominal SSAD to an Initial Velocity	48
4.1	Poles of Open-Loop SSAD	51
4.2	Poles of the Position Hold Open-Loop SSAD	53
4.3	Singular Values from Joint Rate Commands to End Effector State for the ROM and FOM	55
4.4	Poles of the Reduced Order Model	56

4.5	Transmission Zeros of the Reduced Order Model	56
4.6	Performance Singular Values of the Current Position Hold System	60
4.7	Control Effort Singular Values of the Current Position Hold System	62
4.8	Closed-Loop Transfer Function	62
4.9	Closed-Loop System for Robust Stability Analysis	63
4.10	Robust Stability Analysis of the Current Position Hold System	66
4.11	Open-Loop System Near Pole Locations With $K_{G_i} = 0.01$ and $K_{MA} = K_{MA_{max}}$.	67
4.12	Open-Loop System Near Pole Locations With $K_{G_i} = 0.05$ and $K_{MA} = K_{MA_{max}}$.	68
5.1	Plant With Compensator	70
5.2	Control Effort Singular Values of the LQR System	73
5.3	Performance Singular Values of the LQR System	74
5.4	Translational Response of PH System and LQR System to Attitude Thruster Commands	75
5.5	Rotational Response of PH System and LQR System to Attitude Thruster Com- mands	76
5.6	Robust Stability Analysis of the LQR System	77
5.7	LQR Closed-Loop System Near Pole Locations for the Nominal and Off-Nominal System	78
6.1	Plant With Compensator	81
6.2	Control Effort Singular Values of the H_2 System	87
6.3	Performance Singular Values of the H_2 System	88
6.4	Translational Response of PH System and H_2 System to Attitude Thruster Com- mands	90
6.5	Rotational Response of PH System and H_2 System to Attitude Thruster Com- mands	91
6.6	Robust Stability Analysis of the H_2 System	92
6.7	Closed-Loop Poles of the Nominal H_2 System	92
6.8	Closed-Loop Poles of the Off-Nominal H_2 System: 1	93
6.9	Closed-Loop Poles of the Off-Nominal H_2 System: 2	93
6.10	Closed-Loop Poles of the Off-Nominal H_2 System: 3	94

6.11 Closed-Loop Poles of the Off-Nominal H_2 System: 4	94
7.1 Plant With Compensator	97
7.2 Control Effort Singular Values of the H_∞ System	101
7.3 Performance Singular Values of the H_∞ and Position Hold Systems	102
7.4 Performance Singular Values of the H_∞ and H_2 Systems	103
7.5 Translational Response of PH, H_2 , and H_∞ Systems to Attitude Thruster Com- mands	105
7.6 Rotational Response of PH, H_2 , and H_∞ Systems to Attitude Thruster Commands	106
7.7 Robust Stability Analysis of the H_∞ System	107
7.8 Closed-Loop Poles of the Nominal H_∞ System	108
7.9 Closed-Loop Poles of the Off-Nominal H_∞ System: 1	108
7.10 Closed-Loop Poles of the Off-Nominal H_∞ System: 2	109
7.11 Closed-Loop Poles of the Off-Nominal H_∞ System: 3	109
7.12 Closed-Loop Poles of the Off-Nominal H_∞ System: 4	110
7.13 Standard Form for a Compensated Plant with Uncertainty	111
7.14 Closed-Loop Transfer Function	111
7.15 Robust Stability Analysis of the ' G_{11} ' H_∞ System	113
7.16 Control Effort Singular Values of the ' G_{11} ' H_∞ System	113
7.17 Performance Singular Values of the ' G_{11} ' H_∞ System	114

List of Tables

3.1	Variable Notation for One Joint EOM	28
3.2	Variable Notation for Six Joint EOM	30
3.3	Variable Notation for Servo Parameters	34
4.1	Gramian Singular Values	58
4.2	Joint Rate Limits	61

Chapter 1

Introduction

Future Space Shuttle operations include the on-orbit assembly of the Space Station Freedom (SSF). This assembly process will require the Shuttle Remote Manipulator System (SRMS) to manipulate many separate elements of the SSF toward its ultimate construction. Experience in SRMS payload operations gained over the last decade indicate deficiencies in current operations. Some of these deficiencies are of particular concern for the assembly of the SSF. One such concern is the long durations of time required to damp vibrations of the SRMS and attached payload after a given maneuver. Attitude thruster firings of the Shuttle Flight Control System (SFCS) during SRMS operations is another source of undesired excitations. The time spent waiting for these undesired vibrations to damp out can consume a significant fraction of the total mission time. For example, the estimated time spent waiting for the SRMS to damp during the first sixteen Shuttle flights required for the SSF assembly task is illustrated in Figure 1.1 [1].

The SRMS consists of six joints connected via tubular structural members with a grapple at the end effector for grasping payloads. Some of these structural members are longer than 6 meters. The total length of the extended arm is over 15 meters, making for a very flexible structure. Control of the arm is performed by six motor rate feedback servos, one for each joint. In order to perform end effector or payload maneuvers, the SRMS has five modes of operation. These modes include the Automatic Mode, the Manual Augmented Mode, the Single Joint Mode, the Direct Drive Mode, and the Backup Drive Mode. The Direct Drive Mode and the Backup Drive Mode are both contingency modes that allow the SRMS to operate even if certain system failures occur. After the SRMS completes a maneuver in one of the three regular modes, each servo is initially given a zero rate command. After the zero rate command state, the SRMS

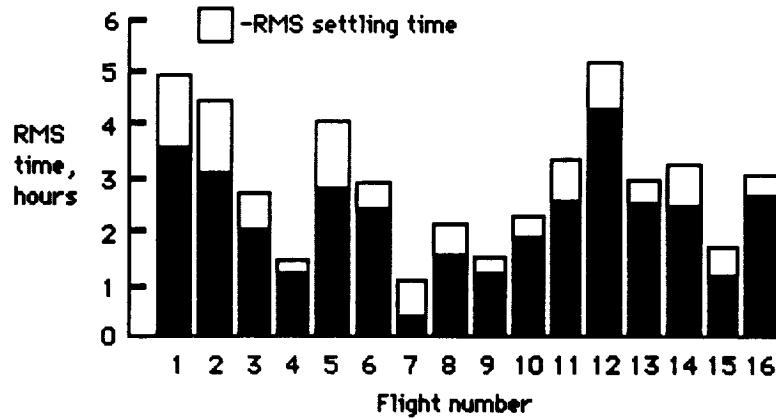


Figure 1.1. Cumulative SRMS Damping Time

drops into Position Hold. In Position Hold, as the name implies, the system tries to maintain its final end-point position and attitude. The design philosophy for the SRMS is discussed in detail by Ravindran [2].

Currently, the SRMS maintains Position Hold end-point control using the joint control servos. In Position Hold, each joint is equipped with a controller that supplies joint rate commands based upon angle feedback from joint encoders. However, since boom flexibility is not observable in the joint angle feedback measurements, no active vibration suppression currently exists for control of the SRMS and attached payload. Simple movements of the SRMS with a heavy payload attached can cause vibration of the arm with frequencies inside the control bandwidth. An even larger source of excitation is Shuttle attitude control thruster firings that are required to support payload operation constraints such as: lighting, contamination, and release or tip-off requirements. The system must wait for these vibrations to die out since it is not actively damping them. Current control system design technology offers the opportunity to design controllers that will actively damp such undesired vibrations. The key is to provide such controllers with information about the structural flexibility of the SRMS.

Gilbert, et al. [1] investigated active damping of the SRMS using a Linear Quadratic Gaussian (LQG) controller. Gilbert approached the problem by replacing the zero rate command state with a LQG controller after the SRMS finishes a maneuver. Assuming linear accelerometers on the end effector, this controller damps the joint rate commands to a specified level before falling into Position Hold. Gilbert has applied this technique to the Single Joint and

Manual Augmented Modes of operation.

Engineering simulations have shown that Position Hold itself can be unstable, particularly with heavy payloads associated with the SSF assembly task. There are several advantages in providing compensation for the current Position Hold mode. Since Position Hold is universal to the three standard control modes, improving its performance improves the SRMS over its full range of normal operations. Furthermore, the joint deflections are relatively small in Position Hold. Therefore, the nonlinear plant associated with a six degree-of-freedom robotic manipulator is operating in a fairly linear region. Significant nonlinearities come from the servos rather than the kinematics associated with the geometry. The servo nonlinearities are easier to characterize using linear control design techniques.

This thesis provides a survey of several linear control design techniques as applied to vibration damping and disturbance rejection of the SRMS while operating in Position Hold. Rather than damping the joint angles, the end effector position and attitude are damped since reducing oscillations of the payload itself is more crucial. Design methodologies examined include: Linear Quadratic Regulator (LQR) synthesis, Linear Quadratic Gaussian or H_2 optimization, and H_∞ optimization derived compensation. Designs are compared with the current SRMS Position Hold controller in both the frequency and time domains. Regulators are designed to maintain the SRMS end effector position and attitude relative to an Orbiter-fixed reference frame while being subjected to Shuttle thruster firings.

There are several significant obstacles to overcome before linear control design techniques can be applied to this problem. First, the nonlinear system must be linearized. Because the arm is essentially in a fixed configuration during Position Hold, the six servos of the SRMS are the main sources of nonlinearities. These nonlinearities include: current and torque limiters, trim integrators, gearbox stiffness, digital and analog tachometers, and joint motor stiction/frictions. The effect of these nonlinearities must either be deemed insignificant, or somehow linearized to a nominal value. One method to model the effects of the significant nonlinearities on the linearized system is to represent them as parameter uncertainties. In this manner, it is possible to perform robust stability analysis via μ -analysis on the linear plant. This analysis will help indicate if the system is stable in face of the nonlinearities present in the system.

These nonlinearities that are modelled as parametric uncertainties pose a significant challenge to any linear controller design. The current Position Hold system is not robustly stable

with these nonlinearities as seen by its limit cycle behavior. In this thesis, each of the three design methodologies, LQR, H_2 , and H_∞ , offer significant performance improvement over the current system. However, none of the designs achieves robust stability. Because the uncertainty of the system is parametric, not unmodeled dynamics, a simple reduction of the bandwidth will not achieve robust stability. The outline of this thesis is as follows:

Chapter 2

This Chapter describes in detail the Shuttle Remote Manipulator System. The Position Hold mode is the focus of discussion to illuminate the advantages in improving its performance. Aside from a physical description of the SRMS, the five control modes are explored in depth: the Automatic Mode, the Manual Augmented Mode, the Single Joint Mode, the Direct Drive Mode, and the Backup Drive Mode.

Chapter 3

This Chapter presents the development of the SRMS model. The equations of motion are derived for a simple one joint case and then extended to six joints. A nonlinear servo model is presented and then linearized by eliminating those effects that are negligible. Two nonlinearities that have significant contribution are treated as nominal parameters with uncertainty. The system is placed in a generalized three-block form. Time domain simulations of both the linear model and a higher fidelity nonlinear model of the SRMS are compared to verify the linear model.

Chapter 4

This Chapter starts out by examining the characteristics of the open-loop design plant. Model reduction is applied since six poles are very fast relative to the rest of the system. This reduced order model is used to design new regulators in subsequent Chapters. The performance and control effort criteria are presented that the subsequent regulator designs will be judged by. As a baseline for comparison, the performance of the current system is analyzed. Two techniques for robust stability analysis, the small gain test and μ -analysis, are presented as well. These techniques are applied to the current Position Hold controller to illustrate the

process as well as explore the characteristics of the current regulator. The shortfalls of these techniques when applied to real parametric uncertainty are explored as well.

Chapter 5

In this Chapter, the first new regulator is designed using the Linear Quadratic Regulator (LQR) methodology. This design requires full-state feedback uncorrupted by sensor noise. The basic theory as well as the design process is explored. The resulting regulator's performance is compared to the current system. Robust stability analysis is performed using the techniques developed in Chapter 4.

Chapter 6

An H_2 optimal compensator is developed in this Chapter. The H_2 theory is presented as well. This model-based compensator does not require full-state feedback. The H_2 regulator relies on state estimates obtained from the noisy measurements of the system to minimize the H_2 norm of a transfer function. As before, the resulting regulator's performance is compared to the current Position Hold. Robust stability analysis is performed using the techniques developed in Chapter 4.

Chapter 7

In this Chapter, an H_∞ optimal compensator is developed. Both the theory and the design process parallel the H_2 design of Chapter 6. The H_∞ regulator minimizes the H_∞ norm of a transfer function. The H_∞ regulator is compared to both the current system and the H_2 system to help highlight the difference in the choice of norms. Robust stability is explored as before. In an effort to obtain a robustly stable compensator, a different transfer function whose norm is minimized is selected. In this manner, it is possible to design for robust stability directly.

Chapter 8

This Chapter offers a summary of the conclusions reached during the development of this thesis and recommendations for further work.

Chapter 2

Description of the Shuttle Remote Manipulator System

The Shuttle Remote Manipulator System (SRMS) is an integral subsystem of the Payload Deployment and Retrieval System (PDRS) on board the Space Shuttle. The SRMS is used primarily for the deployment of payloads from the Orbiter cargo bay, as well as retrieving payloads from orbit and stowing them in the cargo bay. Payloads of up to 30,000 kg mass with dimensions of up to 18.3 meters in length and 4.3 meters in diameter can be handled by the system from up to a 15 meter distance in space. Other applications supported by the SRMS include: crew extravehicular activities (EVA); inspection, servicing and repair of spacecraft; transfer of men and equipment; as well as the on-orbit assembly of the Space Station Freedom (SSF) [2].

The SRMS is operated by a mission specialist from the aft port window location of the crew compartment in the Orbiter. The SRMS operator uses a dedicated control system with the aid of direct viewing as well as a closed circuit television. Television cameras are located in the cargo bay as well as being mounted on the arm itself.

SPAR Aerospace Limited in Toronto in conjunction with a team of Canadian companies performed design, development, testing, and manufacture of the SRMS. All of the work was performed under a contract from the National Research Council of Canada (NRCC) working under the auspices of NASA [2].

This Chapter describes the SRMS system in detail so that the motivation for design choices

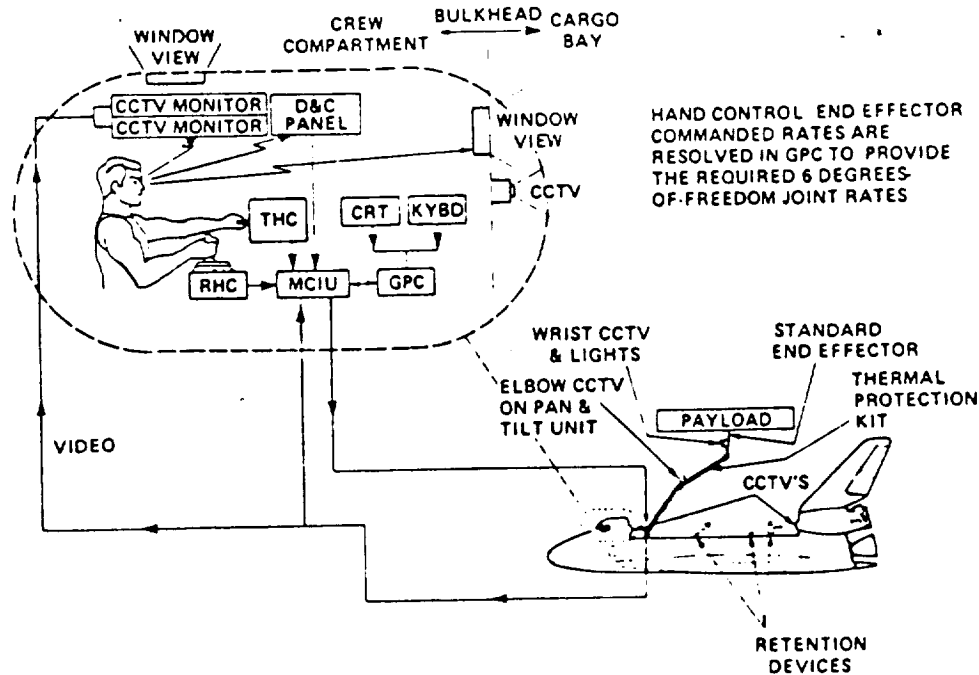


Figure 2.1. Shuttle Remote Manipulator System

can be understood. Section 2.1 details the physical structure of the SRMS. Physical limitations of the arm are also discussed. Section 2.2 explains the five control modes of the SRMS. Of these five control modes, three are for routine Shuttle operations and the remaining two are backup systems. Section 2.3 concentrates on Position Hold and points out its shortcomings.

2.1 Physical Description

The SRMS is comprised of a six degree-of-freedom controlled anthropomorphic man-machine system. This system includes an approximately 15 meter long manipulator arm attached via a swing-out joint to the port longeron of the Shuttle Orbiter cargo bay, a control and display system, a controller interface unit between the manipulator and the Orbiter computers, as well as the closed circuit televisions and lighting systems [3]. A general diagram of the SRMS is shown in Figure 2.1 [2].

The mechanical arm assembly is shown in its stowed position in Figure 2.2. The arm is comprised of six joints connected via structural elements providing a hemisphere of reach for the

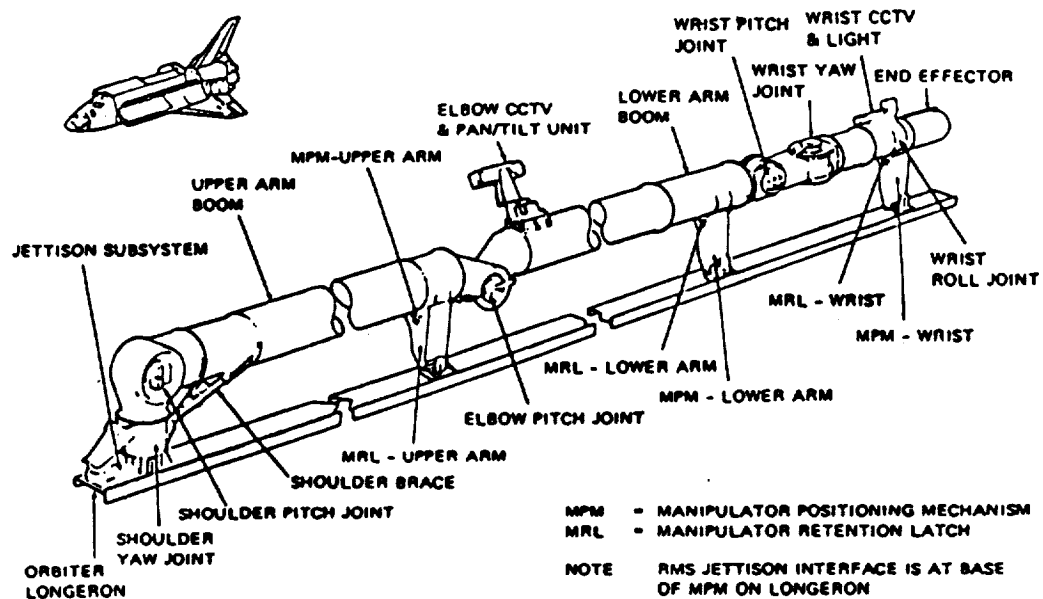


Figure 2.2. Mechanical Arm Assembly

end effector. The joint sequence is as follows: the shoulder yaw and shoulder pitch joints near the arm attachment point; the elbow pitch joint at the arm midsection; and finally three joints, wrist pitch, yaw and roll, near the arm tip. Three dimensional translation of the end effector is provided by the shoulder and elbow joints, whereas the three wrist joints are responsible for its three dimensional orientation [4]. The upper boom of the arm, which is 6.4 meters long, connects the shoulder and elbow joint. Next, the 7 meter lower arm boom connects the elbow joint to the wrist pitch joint. The end effector is attached to the wrist roll joint. The arm booms are made from a graphite/epoxy composite material. They have a thin-walled tubular cross section with internal stiffening rings [3].

The electro-mechanical servos of each joint are similar to each other except for the gear trains. The gear trains vary in their gear ratios with a maximum of 1842:1 for the shoulder joint. All gear trains are designed to provide both forward and backward drive capabilities. Backdrive occurs when a joint is driven by an external torque applied to the output of the gearbox. Backdrive is necessary to limit the loads which can be applied to each joint.

Each servo is comprised of a motor module and a high efficiency, low speed epicyclic gear train. Each motor module has a brushless DC permanent magnet motor, a primary and backup

optical commutator, a tachometer, and an electro-mechanical brake. Angle position feedback is provided from each joint via optical position encoders [2].

The end effector is attached to the wrist roll joint. The end effector is comprised of three snare wires allowing it to grapple a payload and keep it rigidly attached to the Orbiter, or to deploy a payload. Capture or release of a payload is controlled by the arm operator who can view the grapple fixture through a wrist camera [5].

2.2 SRMS Control Modes

There are five control modes of operation for the SRMS; three standard and two back-up modes. The purpose of the SRMS control algorithms is to convert various inputs from several possible sources into rate commands for the six joint servos. The servo rates are the only control input of the system. Currently the only feedback to the control algorithms, besides the operator in the loop, are the joint angles from the high precision position encoders in each joint. Typically the operator desires to control the end effector or some point of resolution (POR) on the payload; either rotationally, translationally, or a combination of both. Inputs to the control algorithms could come from either hand controller inputs made by the arm operator, or an end effector auto sequence trajectory stored in the Orbiter's general purpose computers (GPC) before flight [2].

The five modes of operation of the SRMS are:

1. Manual Augmented Mode
2. Automatic Mode
 - operator commanded
 - preprogrammed auto sequence
3. Single Joint Drive Mode
4. Direct Drive Mode
5. Backup Drive Mode

The Manual Augmented Mode includes the operator in the control loop; this is the normal mode of operation of the arm. The operator commands the end effector (or POR of the payload)

translational and rotational velocity using the two, three-degree-of-freedom hand controllers. Commands from the hand controllers are resolved into joint rate commands by the SRMS computers. The operator has a choice of four different coordinate operating systems [2]. In this mode of operation, all joints can be commanded simultaneously.

Two types of Automatic Modes are available in the SRMS. In the operator commanded auto sequence, the arm is driven along a 'straight line' to coordinates input to the GPC by the operator during flight. During a preprogrammed auto sequence, the operator can select up to four of 20 preprogrammed trajectories to execute at one time. These preprogrammed trajectories, which are verified before flight, are composed of up to 200 straight line elements stored in the GPC. The operator can select any point along the straight line elements as a pausing point for the arm until he or she requests it to complete the trajectory [3].

In the Single Joint Drive Mode the operator can control an individual joint with the full support of the GPC. The operator selects the joint and provides a fixed drive signal. The GPC then interprets the appropriate rate commands. The remaining joints are kept in a Position Hold status as described in Section 2.3 [3].

Direct Drive Mode is the first contingency mode of the SRMS. As in the Single Joint Mode, the operator may command only one joint at a time. In this mode, the remaining joints are deactivated and held in position by their brakes. Commands to the working joint are hardwired to the Motor Drive Amplifiers (MDA). Commands bypass the GPC, data buses, and the servo control loop [2].

The Backup Drive Mode is an additional contingency mode provided to help insure the SRMS is fail-safe. Similar to the Direct Drive Mode, only one joint may be controlled at a time. It is used when no primary drive channels are available. It bypasses all primary channel electronics, including the GPC, and uses a separate Backup Drive Amplifier (BDA) and backup motor commutator driven by a separate power source [3].

2.3 Position Hold

After completion of an SRMS maneuver in one of the three normal modes of operation, each control servo is given a zero rate command for a short period of time (determined by the payload/arm configuration). After the zero rate command, each servo drops into Position

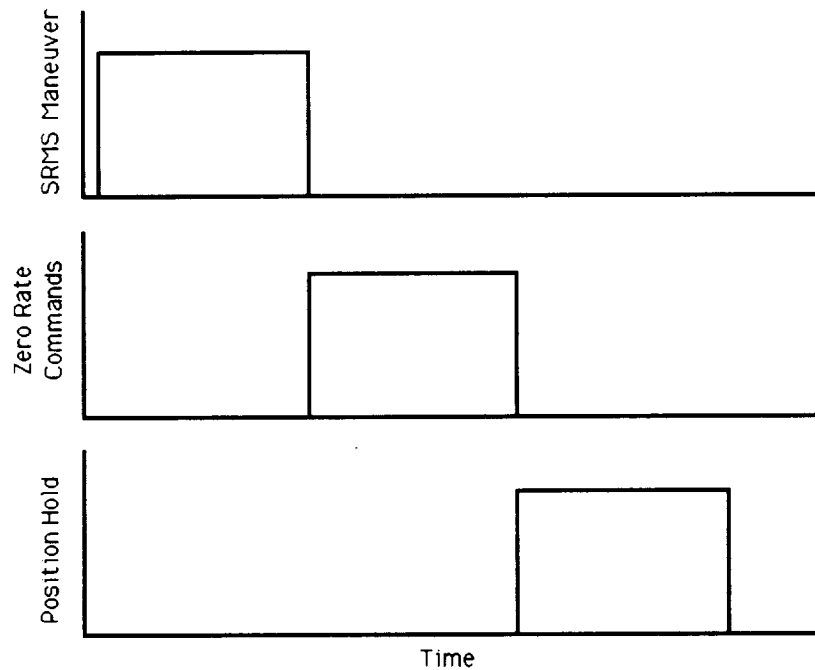


Figure 2.3. Typical SRMS Maneuver Profile

Hold Mode. This zero rate command period is the window in which the controllers designed by Gilbert, et al.[1] reside. It is designed to damp end effector velocities as quickly as possible. A typical SRMS maneuver time profile is shown in Figure 2.3.

As the name implies, the purpose of the Position Hold Mode is too keep the arm in a fixed position. This mode is employed after a maneuver to give the SRMS time to settle and maintain a fixed position and attitude. At this point the operator either moves on to the next maneuver, or has reached the desired final position. This is actually a subtle point; between maneuvers of a given series of maneuvers the operator is not necessarily concerned with a particular end effector position and attitude, rather he or she would like all oscillations to stop before moving on to the next maneuver. However, after the final maneuver of a sequence the end effector position and attitude is the principal concern, especially in operations such as SSF assembly. For this reason, linear controller designs presented subsequently will regulate end effector position and attitude rather than its velocity.

During Position Hold Mode, joint angle positions measured via the joint angle encoders are fed back to the servo control loops. It is important to realize that the joint angles are

converted into joint rate commands via proportional feedback only. With only the joint angles provided to the servo control loops, no information about flexibility in the manipulator booms is available. Currently the operator must wait for the arm structure to damp excitations in the booms resulting from residual energies after a maneuver. Furthermore, while the SRMS is in Position Hold, current guidelines allow Shuttle attitude reaction control system (RCS) firings. In such a situation, Position Hold should maintain the end effector in its current position and attitude relative to an Orbiter-fixed reference frame. However, Shuttle attitude jet firings excite considerable flex in the booms of the SRMS. Furthermore, when heavy payloads (>10K lbs) are deployed on the SRMS, this RCS induced flexure can result in closed-loop Shuttle flight control system instabilities.

If it is desired to reduce the fraction of mission time squandered waiting for the SRMS to settle and to reduce dynamic interaction with other control systems, the benefits of focusing on improving Position Hold Mode are apparent. Position Hold Mode is universal to the three regular control modes; therefore, improving its performance improves the SRMS for its full range of normal operation.

Chapter 3

Modelling the SRMS

Modelling is a delicate task of representing the dynamics of the Orbiter/SRMS/Payload system which are important for the envelope of design while ignoring dynamics which are outside the envelope. We are interested in improving SRMS performance while it is operating in its Position Hold Mode. Position Hold Mode is a regulator; one that desires to subdue initial conditions (residual energies from arm maneuvers), and reject disturbances (introduced by Shuttle attitude jet firings). In this mode, the arm is essentially in a fixed position; therefore, changing mass and inertia matrices associated with changing arm geometries are not a significant factor. However, the six electro-mechanical control servos at the joints do contain substantial nonlinearities in their dynamics which cannot be ignored.

The approach taken to modelling the SRMS is to divide the system into two subsystems. First, the dynamics of the Orbiter/SRMS/Payload (arm) subsystem are considered without the dynamics of the servos. Second, the control servo dynamics are modelled. A block diagram depicts the total system in Figure 3.1.

Inputs to the 'arm dynamics' subsystem include Shuttle attitude thruster firings, sensor noise, as well as the torques on each joint generated by their corresponding control servo. These inputs are combined to determine the end effector acceleration. This acceleration is then integrated to obtain the outputs of this subsystem which are end effector position and attitude as well as the six joint angles. The joint angles are fed back through a proportional feedback gain matrix to the control servos. If we consider the joint angle and end effector perturbations to be small, which is the case in Position Hold, this subsystem is essentially linear.

The control servo subsystem consists of six servos which have as inputs joint rate com-

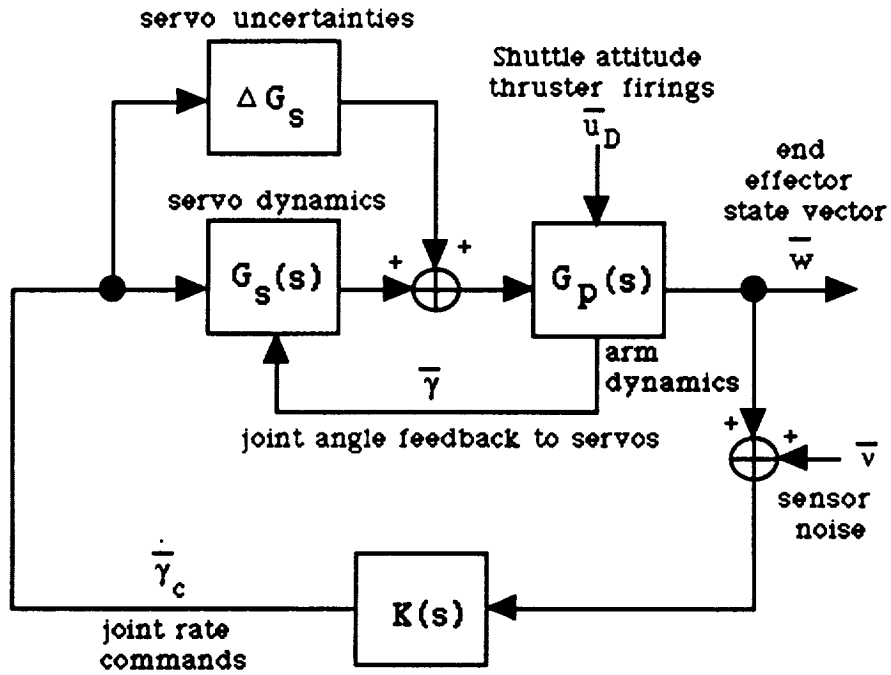


Figure 3.1. Block Diagram of the Compensated System

mands from a designed controller as well as the joint angles determined by the arm dynamics. This subsystem has as outputs the torques generated on each joint. There are several nonlinearities present in each servo, including: current and torque limiters, trim integrator limiter, gearbox stiffness, digital and analog tachometers, as well as joint motor stiction/frictions. The approach taken to linearize this nonlinear subsystem is to treat the nonlinearities as modelling uncertainties on a linear plant.

Section 3.1 generates the equations of motion for the Orbiter/SRMS/Payload system. Equations are generated in an Orbiter-fixed reference frame. The equations of motion are derived for a simplified one joint example and then extended to six joints. Assumptions used in modelling are also outlined.

Section 3.2 begins with a nonlinear model of the joint servos and obtains a simplified linear model. This linear model is then combined with the arm plant in order to generate a linearized model of the complete SRMS. In order to linearize the control servos, certain nonlinearities are ignored which have minimal contribution in Position Hold Mode. The remaining nonlinearities are linearized by selecting 'nominal' values, but their effects are modelled as parameter

uncertainties on the linear plant. The standard three block form of a transfer function used for design and robust analysis is introduced as well. The limitations of the methods used in this Section are also discussed.

The resulting 24 state linearized model is compared with a higher fidelity nonlinear simulation in Section 3.3. This nonlinear simulation has been compared with actual flight data to confirm its accuracy. Comparisons are made in the time domain in Position Hold Mode. The effects of varying the parameter uncertainties of the linear plant in an effort to capture the range of the nonlinear behavior are also investigated. Section 3.4 draws the conclusions of this Chapter. The deficiencies of the major assumptions used in this Chapter are also re-explored.

3.1 Equations of Motion for the Orbiter/SRMS/Payload System

Much of the derivation of the equations of motion in this section is based on the SRMS simulator LSAD¹. LSAD is a higher fidelity nonlinear simulation of the SRMS and flight control system of the Space Shuttle. Details on LSAD and the basis of this section can be found in References [7], [8], and [9].

In deriving the equations of motion, the mass of the connecting structure between the Orbiter and payload can be ignored when a payload mass exceeds 5,000 lbs. Previous simulations have found this assumption to be reasonable. LSAD as well is based on this assumption. Reference [7] has the detailed derivation of the rotational dynamics between two bodies connected via a massless, flexible structure. Rather than derive the six joint case, Section 3.1.1 examines the one joint case and Section 3.1.2 extends it to six joints based on the work in Reference [7].

3.1.1 Equations of Motion for the Single Joint Case

Figure 3.2 represents the case of a single joint in Position Hold. The SRMS has been recast as a point mass, m , oscillating on the end of a massless flexible beam which is attached to a single joint. A joint in Position Hold behaves as a spring with some damping. Table 3.1 defines the essential variables.

¹LSAD stands for Less Singing And Dancing; a take off of Spar Aerospace's ASAD: All Singing And Dancing.

Table 3.1. Variable Notation for One Joint EOM

Variable	Description
p	force acting on the beam
τ_j	torque acting at the joint
w	displacement of the beam tip
w_f	deflection of the beam tip due to flexure
w_j	deflection of the beam tip due to joint angle
a	bending flexibility of the beam
γ_j	joint angle
L	length of the beam

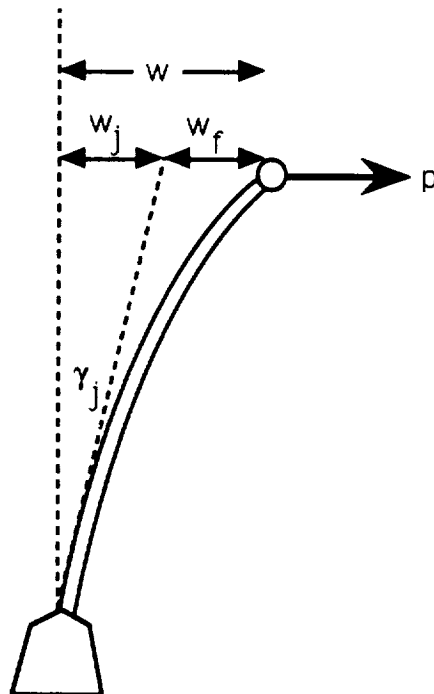


Figure 3.2. One Joint Illustration: Point Mass on a Massless Flexible Beam

From these definitions

$$w = w_f + w_j \quad (3.1)$$

$$w_j = L\gamma_j \quad (3.2)$$

$$w_f = ap \quad (3.3)$$

$$\tau_j = Lp \quad (3.4)$$

Therefore

$$w = L\gamma_j + ap = L\gamma_j + a\frac{\tau_j}{L} \quad (3.5)$$

From Newton's second law, in the absence of external forces, the force at the tip, or the torque over the length, is equal to the acceleration of the mass

$$p = -m\ddot{w} \quad (3.6)$$

When combined with Equation 3.4, this can be recast as

$$w = -\frac{1}{mLs^2} \tau_j \quad (3.7)$$

Combining Equation 3.7 with 3.5 obtains

$$\gamma_j = -\frac{1}{L^2} \left[\frac{1}{ms^2} + a \right] \tau_j \quad (3.8)$$

Equations 3.7 and 3.8 together achieve the objectives of determining the end effector position, w , (position only for the one joint case) and the joint angle position, γ_j , given a torque input to the system, τ_j . These two equations can be rewritten as

$$w = -s^{-2}m^{-1}L^{-1}\tau_j \quad (3.9)$$

$$\gamma_j = -\left[s^{-2}L^{-1}m^{-1}L^{-1} + L^{-1}aL^{-1}\right]\tau_j \quad (3.10)$$

Though this representation seems notationally verbose, it will help motivate the six joint case. The extension of this problem to six joints involves more complex notation, but essentially the same concepts.

3.1.2 Equations of Motion for the Six Joint Case

In extending this problem to six joints and three dimensions, it is necessary to introduce vector and matrix notation to keep track of positions and rotations. Furthermore, we will add the effects of external forces caused by Shuttle attitude thruster firings to the system.

As before, \bar{w} , will define the state of the end effector in an Orbiter-fixed reference frame. Now, however, in three dimensions it is composed of a displacement vector and a rotation vector

$$\bar{w} = \begin{bmatrix} \bar{q} \\ \bar{\delta} \end{bmatrix} \quad (3.11)$$

where \bar{q} is the vector defining the translational deflection of the end effector due to the applied load. Similarly, $\bar{\delta}$ is the vector defining the angular deflection of the end effector on each axis due to the applied load. Since Position Hold Mode entails small variations about equilibrium, rotations can be described by vectors. Table 3.2 makes similar definitions as before.

Table 3.2. Variable Notation for Six Joint EOM

Variable	Description
\bar{p}	applied force from the payload at the end effector
$\bar{\tau}$	applied moment from the payload at the end effector
$\bar{\tau}_\gamma$	vector of servo torques at each joint
\bar{w}	end effector state vector
\bar{w}_f	end effector deflection due to flexibility of the arm
\bar{w}_j	end effector deflection due to rotations of the joints
A	6 by 6 flexibility matrix
$\bar{\gamma}$	joint angle vector
L	6 by 6 Jacobian matrix

As before, \bar{w} may be decomposed as follows

$$\bar{w} = \bar{w}_j + \bar{w}_f \quad (3.12)$$

where

$$\bar{w}_j = L\bar{\gamma} \quad (3.13)$$

and

$$\bar{w}_f = A \begin{bmatrix} \bar{p} \\ \bar{\tau} \end{bmatrix} \quad (3.14)$$

The six joint analog of Equation 3.4 is

$$\bar{\tau}_\gamma = L'^T \begin{bmatrix} \bar{p} \\ \bar{\tau} \end{bmatrix} \quad (3.15)$$

where $\bar{\tau}_\gamma$ is a vector of the servo torques at each joint. This expression can be inverted as follows

$$L^{-T'} \bar{\tau}_\gamma = \begin{bmatrix} \bar{p} \\ \bar{\tau} \end{bmatrix} \quad (3.16)$$

Combining Equation 3.12 with 3.16, 3.13, and 3.14 gives

$$\bar{w} = L\bar{\gamma} + AL^{-T'} \bar{\tau}_\gamma \quad (3.17)$$

The six joint version of Equation 3.6 with the effects of external forces added is

$$\begin{bmatrix} \bar{p} \\ \bar{\tau} \end{bmatrix} = -s^2 M \bar{w} + \bar{u}_{II} \quad (3.18)$$

where M is the system mass matrix and \bar{u}_{II} is the vector representing the effect of control torques from Shuttle attitude thruster firings. Combining Equations 3.16 and 3.18 obtains

$$\bar{w} = -s^{-2} M^{-1} L^{-T'} \bar{\tau}_\gamma + s^{-2} M^{-1} \bar{u}_{II} \quad (3.19)$$

Placing Equation 3.19 into Equation 3.17 results in

$$\bar{\gamma} = - \left[s^{-2} L^{-1} M^{-1} L^{-T'} + L^{-1} A L^{-T'} \right] \bar{\tau}_\gamma + s^{-2} L^{-1} M^{-1} \bar{u}_{II} \quad (3.20)$$

Equations 3.19 and 3.20 are the six joint analogs of Equations 3.9 and 3.10. These together define the equations of motion for the Orbiter/SRMS/Payload subsystem. Given the torques produced by the control servos, and disturbances caused by Shuttle attitude thruster firings, the state vector defining the end effector position and attitude as well as the joint angle vector are determined by the above system of equations.

3.2 Modelling and Linearization of the Control Servos

The general approach of this Section is to characterize the transfer function between the joint angles, $\bar{\gamma}$, and the joint rate commands, $\dot{\bar{\gamma}}_c$, to the torque output at the joints, $\bar{\tau}_\gamma$. Section 3.2.1 linearizes this nonlinear system, while Section 3.2.2 characterizes the effect of significant nonlinearities.

3.2.1 Control Servo Dynamics

The highest fidelity model of the SRMS servos available at Draper Laboratory is shown in Figure 3.3. This model was designed to be accurate over a large frequency range and a wide envelope of operations. This model is faithful enough to even encompass the accelerations of the motor shaft while it transitions from forward driving to back driving² using simulation time steps of 2 milliseconds [8]. References [8] and [10] show that for the low frequency oscillations that occur with heavy payloads, much of Figure 3.3 can be eliminated.

References [8] and [10] both derive linearized models of the servo, but for slightly different purposes. They do, however, provide useful insight into the nature of the nonlinearities as well as the conditions in which they can be ignored. Figure 3.4 represents the linearized model of the servos. Table 3.3 defines the variables of Figure 3.4. All quantities are either vectors or matrices since there are six servos. The servos are all similar in configuration; differences occur only in the values of the gear ratios, current limiters, moments of inertias, and gearbox stiffness.

Heavy payloads are assumed in modelling the arm dynamics. Draper's experience with the SRMS in Position Hold mode demonstrates these conditions imply low frequency motions with moderate amplitudes. This implies we can neglect high frequency dynamics. In linearization, the effects of gear backlash, stictions, and frictions are ignored since they have negligible effect. Simulations have shown that the integral trimmer has an effect only on motion when friction is important; therefore, the trimmer and its limiter are eliminated from the linear model. The analog tachometer with its high pass filter has negligible effects on low frequency motions, so it is eliminated as well [8]. The digital tachometer's quantization effects are ignored; it is treated as a linear gain. While in Position Hold, the current limiter saturates before the torque limiter so the torque limiter can be eliminated from the model. Indeed, the most significant nonlinearities

²Forward drive occurs when the motor is driving the payload. Back drive occurs when the payload is driving the motor.

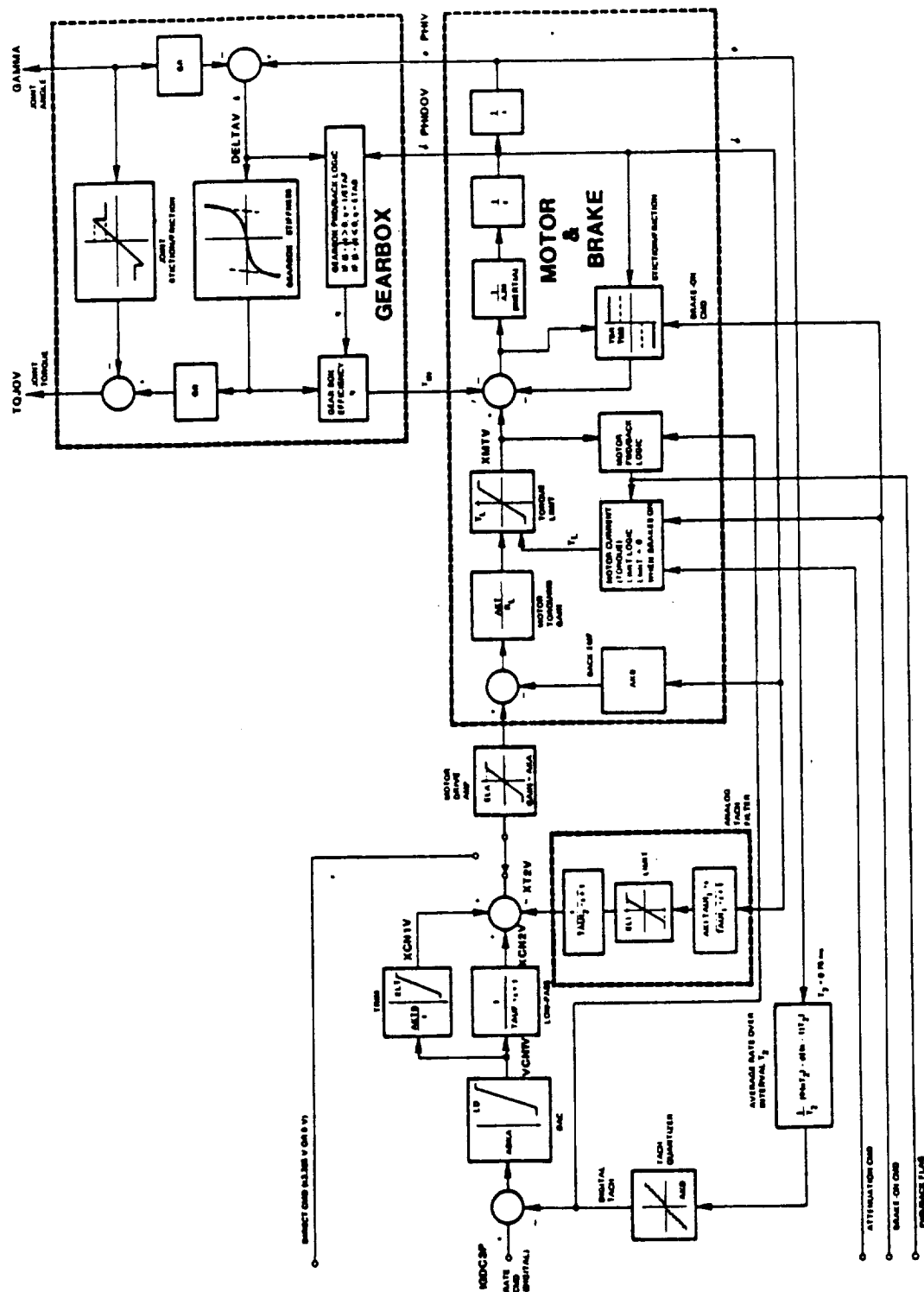


Figure 3.3. Draper Servo Model

Table 3.3. Variable Notation for Servo Parameters

Variable	Description	Units
$\bar{\gamma}$	Joint Angle Vector	radians
$\bar{\tau}_{\gamma}$	Vector of Torque at each Joint	ft-lb
$\dot{\bar{\gamma}}_C$	Joint Rate Commands	rad/sec
$\bar{\phi}$	Motor Shaft Angle Vector	radians
$\dot{\bar{\phi}}$	Motor Shaft Rate Vector	rad/sec
N	Gear Ratio	-
K_1	Motor Speed Command Scaling Gain	count/rad/sec
K_{DA}	Digital-to-Analog Converter Gain	v/cnt
K_A	Motor Drive Amplifier Gain	v/v
K_T/R_L	Motor Torquing Gain	ft-lb/v
K_D	Effective Gain of Digital Tachometer Processing	cnt/rad/sec
K_H	Motor Back EMF Constant	v/rad/sec
K_{MA}	Gain of the Forward Path: $K_{DA}K_AK_T/R_L$	ft-lb/cnt
K_{FH}	Gain of the Feedback Path: $K_D + K_H/K_{DA}K_A$	cnt/rad/sec
J_M	Motor Rotor and Gearbox Input Shaft Moment of Inertia	slug-ft ²
K_G	Gearbox Stiffness	ft-lb/rad

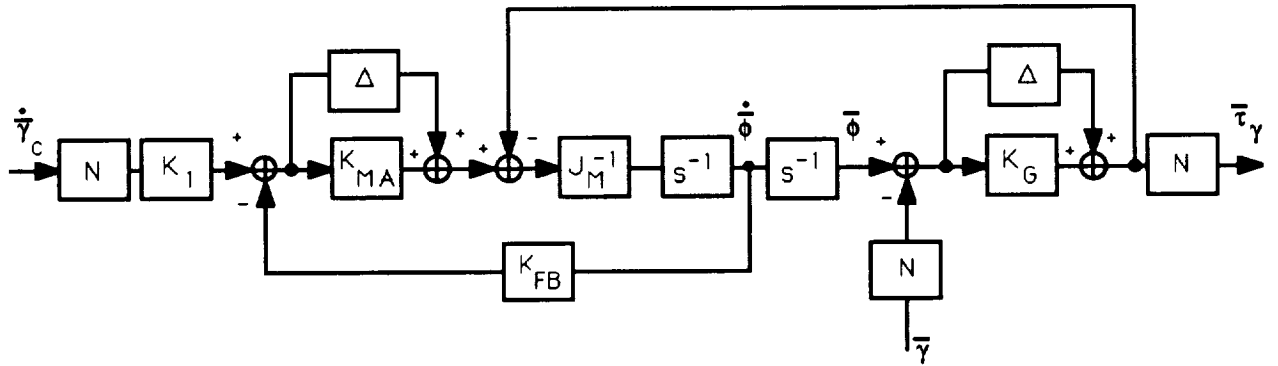


Figure 3.4. Linearized Servo Model

while operating in Position Hold with a heavy payload are the motor current limiter and the gearbox stiffness curve. These cannot be dismissed as easily as the other nonlinearities. Ignoring their effects could lead to controller designs which do not achieve robust performance or stability.

In an attempt to capture the effect of these nonlinearities, uncertainty blocks are used. Combining the gains in the forward path of the servo leads to a single gain, K_{MA} . This gain includes the effect of the current limiter. Since it has the potential to saturate via its limiter, it is represented in Figure 3.4 with an uncertainty block, Δ , around it. Gearbox stiffness, K_G , with its nonlinear behavior has a Δ block around it as well. The mathematical characterization of these Δ blocks is discussed in the next Section.

Figure 3.5 combines the results of the servo dynamics and the arm dynamics in block diagram form. This linearized version of the SRMS has been dubbed SSAD³. If not for the Δ blocks, it would be short work to put this linear plant model into state-space form⁴

$$\begin{aligned}\dot{x}_p &= A_p x_p + B_p u \\ y &= C_p x_p + D_p u\end{aligned}\tag{3.21}$$

where x is the plant state vector, y is the observation vector, and u is the control vector. Equation 3.21 represents the nominal state-space form of SSAD.

For the development of regulators in subsequent Chapters, measurements of the end effector position and attitude for feedback are assumed. This selection of measurements provides the necessary observability of the structural flexibility existing in both the SRMS booms and the

³SSAD stands for Some Singing And Dancing.

⁴From now on, bars are left off vectors since all quantities are vectors or matrices unless specified otherwise.

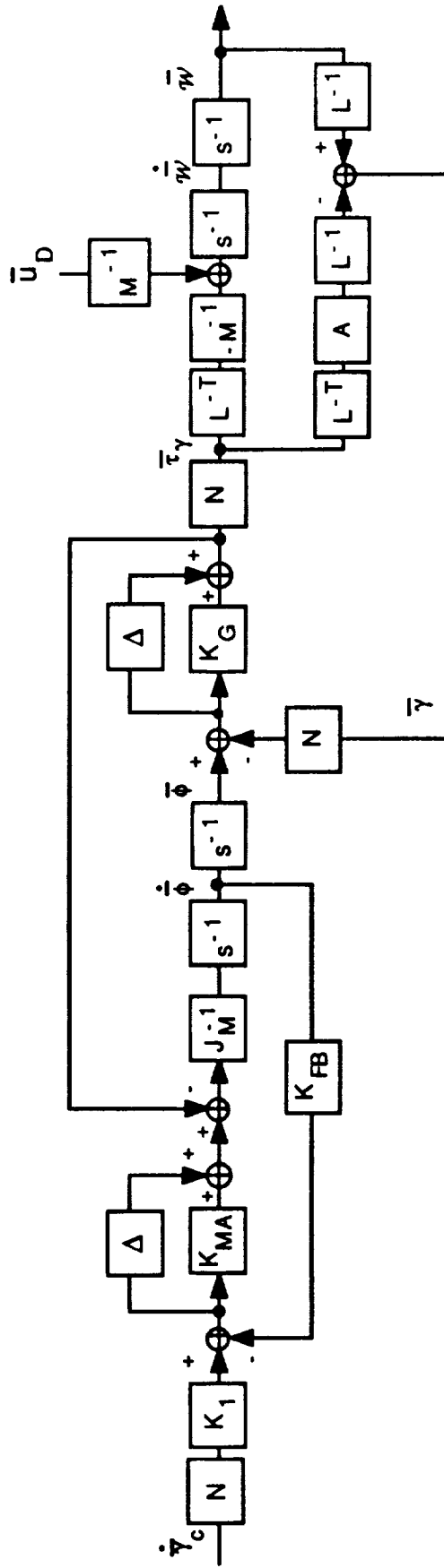


Figure 3.5. Linearized SRMS Model

gearboxes at each joint. There are several types of sensor suites that can recover this type of information, including force-torque sensors, strain gauges, or accelerometers. Eventually, the NASA/Johnson Space Center (JSC) plans to incorporate one of these set-ups into the SRMS system.

3.2.2 Representing the Uncertainties

The method of characterizing parametric uncertainty presented in this Section follows the work of Reference [11]. As shown in Figure 3.5, the state-space model of SSAD is a function of several physical parameters, two of which, K_G and K_{MA} , are uncertain. Using the form of Equation 3.21 it is possible to model these parameter errors as

$$\begin{aligned} \dot{x}_p &= \left(A_p + \sum_{i=1}^k \Delta A_i \delta_i \right) x_p + \left(B_p + \sum_{i=1}^k \Delta B_i \delta_i \right) u \\ y &= \left(C_p + \sum_{i=1}^k \Delta C_i \delta_i \right) x_p + \left(D_p + \sum_{i=1}^k \Delta D_i \delta_i \right) u \end{aligned} \quad (3.22)$$

where each δ_i represents a parameter error that has been normalized as

$$-1 < \delta_i < 1 \quad \forall i$$

As this suggests, the nominal value of both K_G and K_{MA} must be bounded equally from both above and below. Consider K_G first.

The gearbox stiffness curve is shown in Figure 3.6. The gain, K_G , is the slope of the curve at the point $\phi - \gamma$. This slope can achieve values from zero up to a maximum slope that is determined by the servo under consideration. One choice that captures all possible values of K_G is to choose the nominal value as half the maximum attainable slope with bounds above and below of also half the maximum slope. This, however, will introduce problems when performing robust analysis. Allowing a zero value for K_G is essentially allowing for the possibility of the servos to be cut off from the rest of the system. All of the servos' associated dynamics would become both uncontrollable and unobservable to any controller. Such a system will always fail robust stability analysis. This, however, is a mathematical fiction. The system's manifestation in a zero K_G state is transient, not a situation which the controller must deal with for any length of time. A gain of 0.01 is used as the minimum value of K_G in order to pose the bounds

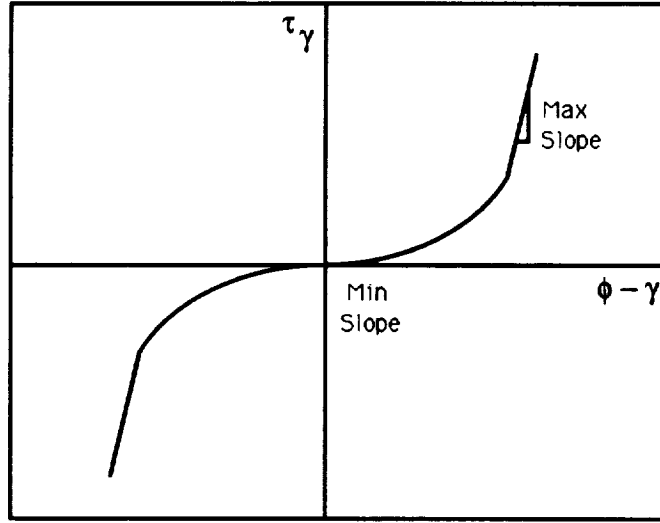


Figure 3.6. Gearbox Stiffness Curve

in a better conditioned manner. For a value of K_{G_i} below 0.01 we are assuming that the system is either in a state of transition or in a relatively unexcited state. $K_{G_{i_{nom}}}$ is selected in the center of this range.

The current limiter, shown in Figure 3.7, is a unit gain until it saturates. After saturation, the limiter's behavior can be characterized as a gain that is inversely proportional to the input current. The minimum gain achievable, K_{min} , is the current limit value divided by the maximum current possible in the system, both known quantities for each servo. Since the current limiter has been absorbed into K_{MA} , K_{MA} will have a range from $K_{min}K_{MA}$ up to K_{MA} . $K_{MA_{nom}}$ is also selected in the center of this range.

There are now twelve parameters, six K_{G_i} and six K_{MA} , nominally centered in ranges, but free to vary independently of each other. To calculate every possible ΔA_i , ΔB_i , ΔC_i and ΔD_i these parameters would generate through their ranges would be computationally intensive. As a first order approximation, ΔA_i , ΔB_i , ΔC_i and ΔD_i are computed by sending each parameter individually to its upper and lower bound to reduce computation. This will generate a set of 24 perturbed matrices.

The system can now be written in the perturbed state-space form of Equation 3.22. The perturbation matrices associated with each uncertain parameter can be combined into a single

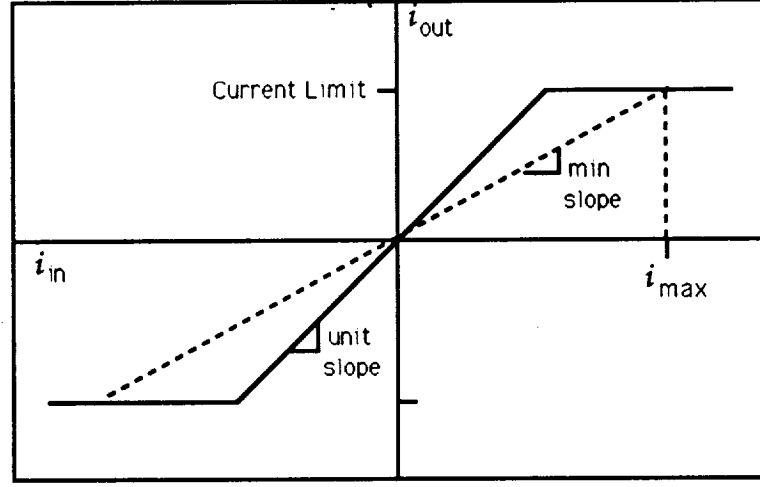


Figure 3.7. Current Limiter

matrix

$$N_i = \begin{bmatrix} \Delta A_i & \Delta B_i \\ \Delta C_i & \Delta D_i \end{bmatrix} \in \mathcal{R}^{(n_x+n_y) \times (n_x+n_u)} \quad (3.23)$$

where $n_x = \dim(x)$, $n_y = \dim(y)$, and $n_u = \dim(u)$. This matrix is not full rank for the SSAD system since any one parameter does not affect all of the states and outputs. N_i can therefore be decomposed as

$$N_i = \begin{bmatrix} Q_i \\ R_i \end{bmatrix} \begin{bmatrix} S_i & T_i \end{bmatrix} \quad (3.24)$$

where for $\text{Rank}(N_i) = n_i$, $Q_i \in \mathcal{R}^{n_x \times n_i}$, $R_i \in \mathcal{R}^{n_y \times n_i}$, $S_i \in \mathcal{R}^{n_i \times n_x}$, $T_i \in \mathcal{R}^{n_i \times n_u}$. The state-space model of the perturbed system can be rewritten as

$$\begin{aligned} \dot{x}_p &= \left[A_p + \sum_{i=1}^k Q_i \delta_i I_{n_i} S_i \right] x_p + \left[B_p + \sum_{i=1}^k Q_i \delta_i I_{n_i} T_i \right] u \\ &= A_p x_p + [Q_1 \dots Q_k] \begin{bmatrix} \eta_1 \\ \vdots \\ \eta_k \end{bmatrix} + B_p u \\ y &= \left[C_p + \sum_{i=1}^k R_i \delta_i I_{n_i} S_i \right] x_p + \left[D_p + \sum_{i=1}^k R_i \delta_i I_{n_i} T_i \right] u \end{aligned} \quad (3.25)$$

$$= C_p x_p + [R_1 \dots R_k] \begin{bmatrix} \eta_1 \\ \vdots \\ \eta_k \end{bmatrix} + D_p u \quad (3.26)$$

$$\begin{bmatrix} \epsilon_1 \\ \vdots \\ \epsilon_k \end{bmatrix} = \begin{bmatrix} S_1 \\ \vdots \\ S_k \end{bmatrix} x_p + \begin{bmatrix} T_1 \\ \vdots \\ T_k \end{bmatrix} u \quad (3.27)$$

The ϵ_i represent the inputs to the uncertainty block, Δ . They are a function of x_p and u . The η_i represent the outputs of the uncertainty block which will influence the state dynamics. This models the effect the parameter uncertainties have on the plant dynamics. Define

$$Q \equiv [Q_1 \dots Q_k]$$

$$R \equiv [R_1 \dots R_k]$$

$$S \equiv [S'_1 \dots S'_k]$$

$$T \equiv [T'_1 \dots T'_k]$$

Augmenting the unperturbed state-space of Equation 3.21 with process noise, w , measurement noise, ν , and the effects of parameter uncertainty as defined above gives

$$\begin{aligned} \dot{x}_p &= A_p x_p + B_p u + B_m w + Q \eta \\ y &= C_p x_p + D_p u + D_\nu \nu + R \eta \\ \epsilon &= S x_p + T u \end{aligned} \quad (3.28)$$

Figure 3.8 represents the general transfer function of a nominal plant, $P(s)$, and compensator, $K(s)$, with parametric uncertainty, Δ . In this representation, d represents all exogenous inputs into the system; in this case

$$d = \begin{bmatrix} w \\ \nu \end{bmatrix} \quad (3.29)$$

and e is an error vector of signals of interest to be defined later. The state-space representation of Figure 3.8 is

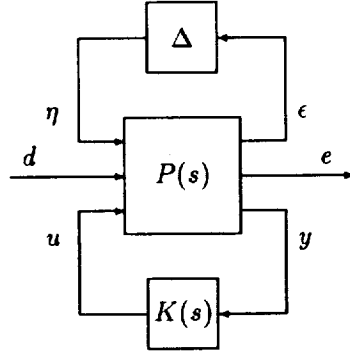


Figure 3.8. Standard Form for a Compensated Plant with Uncertainty

$$\begin{aligned}
 \dot{x} &= Ax + B_1\eta + B_2d + B_3u \\
 \epsilon &= C_1x + D_{11}\eta + D_{12}d + D_{13}u \\
 e &= C_2x + D_{21}\eta + D_{22}d + D_{23}u \\
 y &= C_3x + D_{32}\eta + D_{32}d + D_{33}u
 \end{aligned} \tag{3.30}$$

Placing Equation 3.28 in the form of Equation 3.30 gives

$$\begin{bmatrix} \dot{x}_p \\ \epsilon \\ e \\ y \end{bmatrix} = \begin{bmatrix} A_p & Q & B_2 & B_p \\ S & 0 & 0 & T \\ C_2 & D_{21} & D_{22} & D_{23} \\ C_p & R & D_{32} & D_p \end{bmatrix} \begin{bmatrix} x_p \\ \eta \\ d \\ u \end{bmatrix} \tag{3.31}$$

$$B_2 \equiv [B_w \vdots 0_{(n_x \times n_v)}]$$

$$D_{32} \equiv [0_{(n_y \times n_w)} \vdots D_v]$$

Equation 3.31 represents the state-space equation for the linearized SRMS with the nonlinearities K_{MA} and K_G modeled as parameter uncertainties. One clarification needs to be made about the matrix B_2 . This matrix characterizes how the process noise affects the state. This matrix comes from the u_{ij} term of equation 3.19. u_{ij} represents the effect of Shuttle attitude thruster firings on the end effector. Recall that while in Position Hold mode the Shuttle is

restricted from using its translational thrusters, therefore u_{ij} will effect only the rotational states. However, for computation of a linear optimal estimator such as one employed by model based compensators, every state must be controllable by the noise. To avoid problems before they occur, the effects of fictitious Shuttle translational thruster firings are added to B_2 .

The actual construction of u_{ij} depends upon the Orbiter/Payload configuration. On a given Shuttle mission, pre-flight evaluations select a certain set of jets to fire for a roll, pitch or yaw command for a given Orbiter/Payload configuration. Barring a system failure, those same jets are used every time. Since the force a particular jet will impart to the end effector can be calculated, the disturbance vector, u_{ij} , has six elements corresponding to a roll, pitch, yaw; x translation, y translation, or z translation command. Such a command is normalized to lie between -1 and 1 corresponding to, for example, a -roll command or a +roll command.

3.3 Comparison of the Linear and Nonlinear Plant

There are several simplifications made in developing the linearized SSAD from the nonlinear LSAD. This Section compares the two simulations to expose the deficiencies in the linearization process. Frequency domain information such as singular value decompositions are not available for the LSAD. Instead, comparisons are made in the time domain while running both systems in Position Hold Mode. Figure 3.9 shows a block diagram of SSAD in Position Hold Mode. The Position Hold controller does nothing more than feed back the joint angles, γ , to the servos through a set of gains, K_V .

The Hubble Space Telescope (HST) in its release configuration is selected as the payload on a standard Orbiter. HST weighs 25,000 lbs, so the heavy payload assumption is not violated. HST in its release configuration will be used in subsequent Chapters for all designs since when this research began, ample data was available on this payload in this configuration.

Recall that both K_{MA} and K_G have a range of values. The nominal state-space, $P_{nom}(s)$, places both K_{MA} and K_G at the midpoint of their respective ranges. Since $P_{nom}(s)$ is the plant that will be used in controller design, $P_{nom}(s)$ in Position Hold Mode is compared with LSAD.

Both SSAD and LSAD are run in a Position Hold closed-loop with initial conditions on end effector velocity, \dot{w} . This scenario models the situation occurring when the SRMS drops

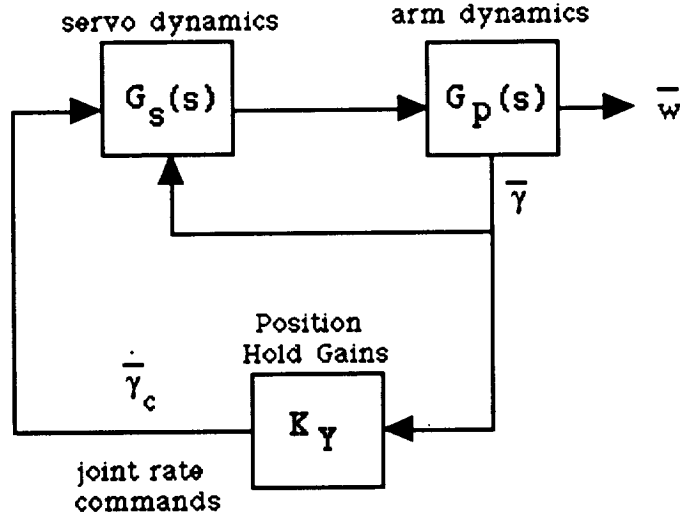


Figure 3.9. SSAD in Position Hold

into Position Hold Mode following a maneuver; the SRMS is instructed to maintain it's current position and attitude though residual velocities remain from the maneuver. Recall that the end effector state vector is constructed as follows

$$\bar{w} = \begin{bmatrix} \bar{q} \\ \bar{\delta} \end{bmatrix} = \begin{bmatrix} X \text{ position} \\ Y \text{ position} \\ Z \text{ position} \\ \text{Roll attitude} \\ \text{Pitch attitude} \\ \text{Yaw attitude} \end{bmatrix} \quad (3.32)$$

Figures 3.10 and 3.11 compare the translational and rotational response of the end effector to an initial velocity for both LSAD and the nominal SSAD. Both amplitudes and frequencies are similar. Considering the linearization process, SSAD compares reasonably well with LSAD.

Recall that Figures 3.10 and 3.11 represent the nominal SSAD plant. In the nominal plant, both K_{MA} and K_G have been placed in the center of their ranges for design and robust analysis purposes. Hopefully, the uncertainty ranges on these gains capture the behavior of the nonlinear plant. Following this logic, there should exist off-nominal values for both K_{MA} and K_G that will make the comparison between LSAD and SSAD more favorable for these initial conditions. Looking at Figures 3.10 and 3.11 it seems that SSAD is damping quicker than

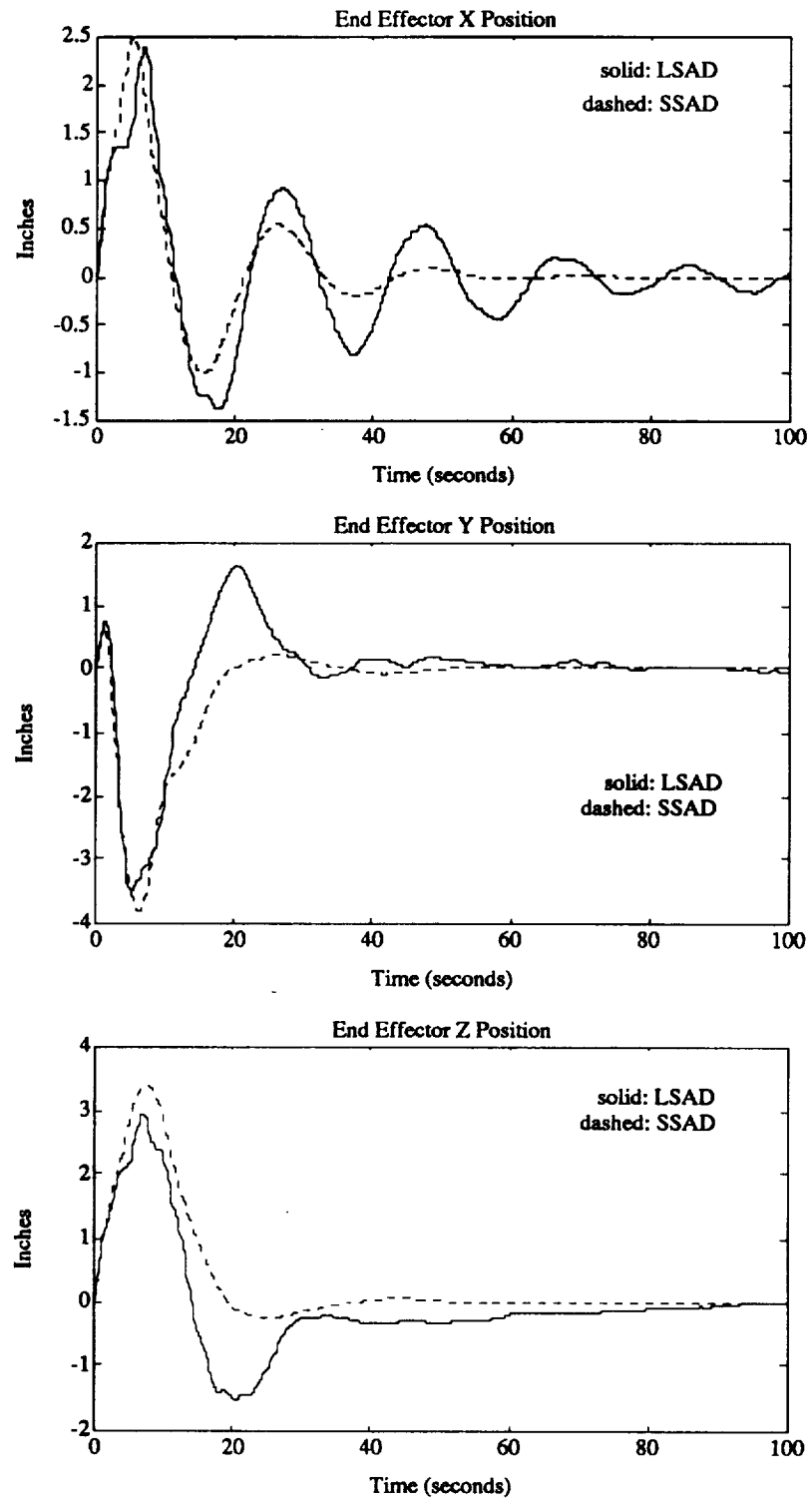


Figure 3.10. Translation Response of LSAD and Nominal SSAD to an Initial Velocity

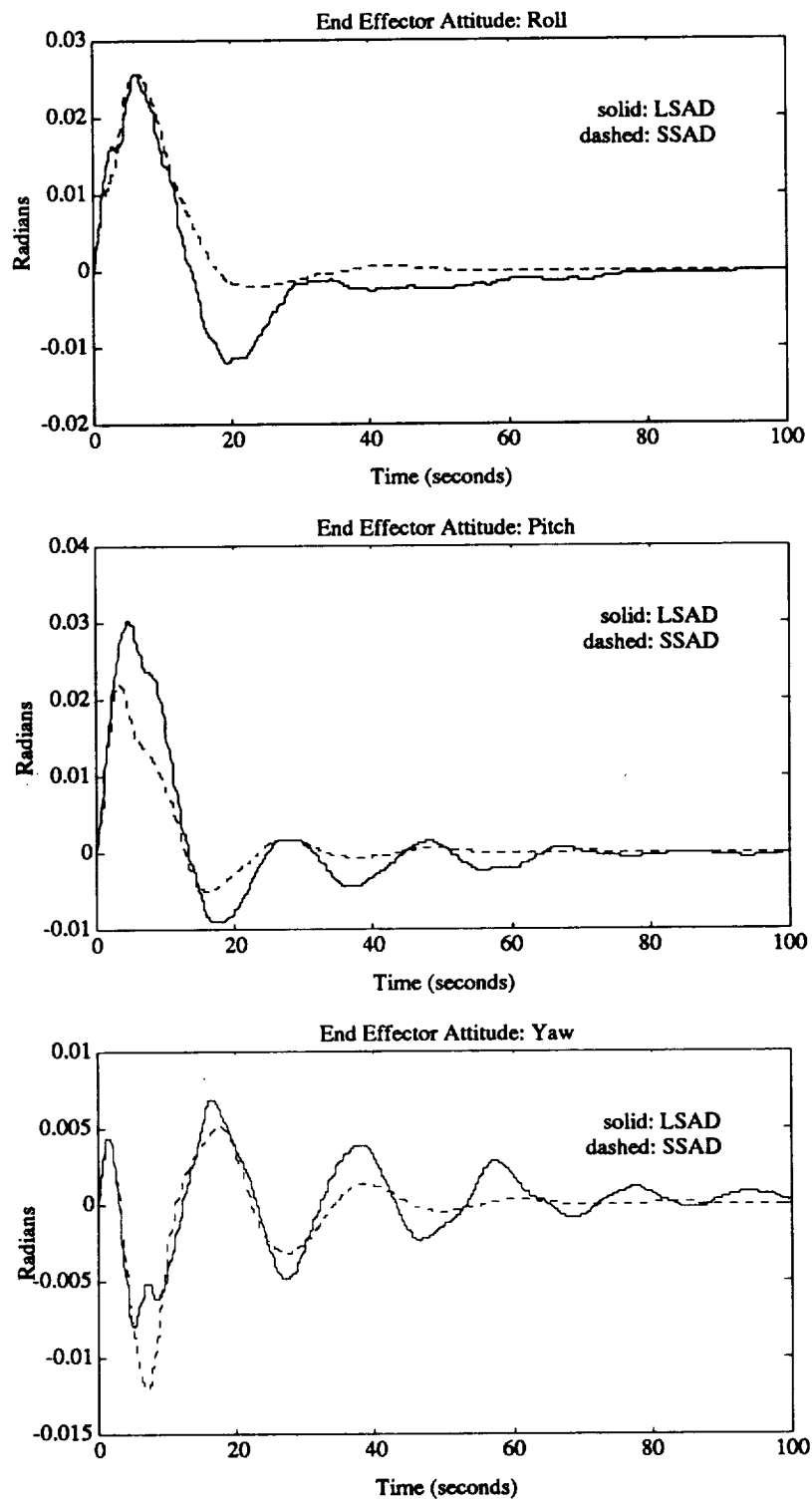


Figure 3.11. Rotational Response of LSAD and Nominal SSAD to an Initial Velocity

LSAD. After moving K_G towards the lower end of its range to compensate this damping, and a little experimentation with increasing K_{MA} as well, Figures 3.12 and 3.13 present an improved match between LSAD and SSAD.

3.4 Conclusions

This Chapter uses several assumptions to bring the SRMS Position Hold plant into a workable linear form. SSAD model accuracy is restricted to payloads greater than 5,000 lbs. This is not a crippling assumption. The 25,000 lbs Hubble Space Telescope is used for design in this thesis. Other assumptions are made in linearizing the nonlinear plant. Several nonlinearities are ignored whose effects are small in the envelope of design. That is, they either have negligible contribution, or dominate at high frequencies. Two significant nonlinearities, K_{MA} and K_G , are represented as parameter uncertainties. These steps are all necessary to obtain a workable plant model such that linear control design techniques can be applied. The drawback, however, is that even if robust stability can be guaranteed on SSAD, this guarantee will not translate to the full nonlinear plant. SSAD can provide a reasonable indication, but not an assurance of robust stability. The standard three block form for design and robust analysis presented in this Chapter will be exploited in subsequent Chapters to provide easy ways to compare controllers designed by different techniques.

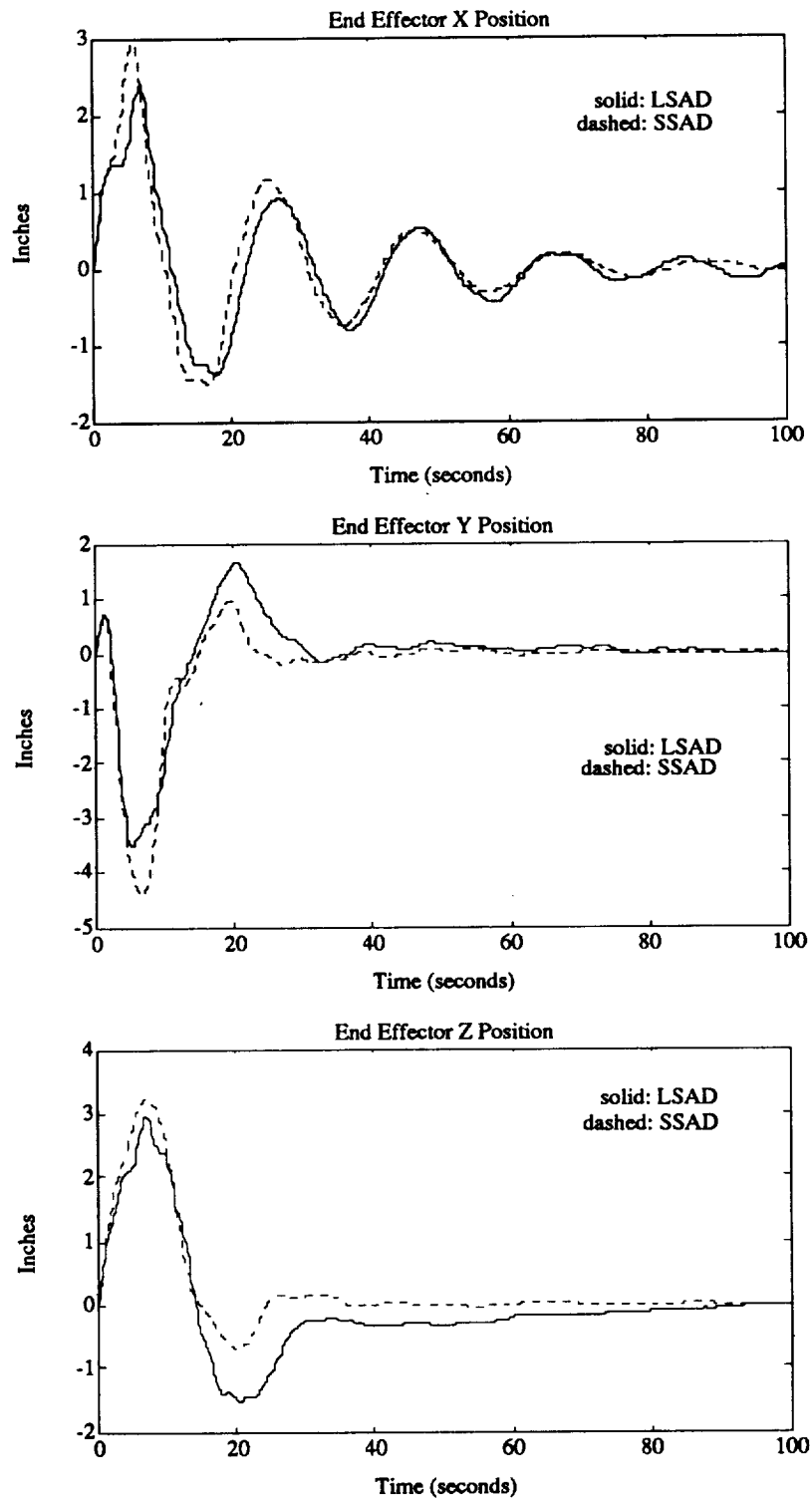


Figure 3.12. Translation Response of LSAD and off-nominal SSAD to an Initial Velocity

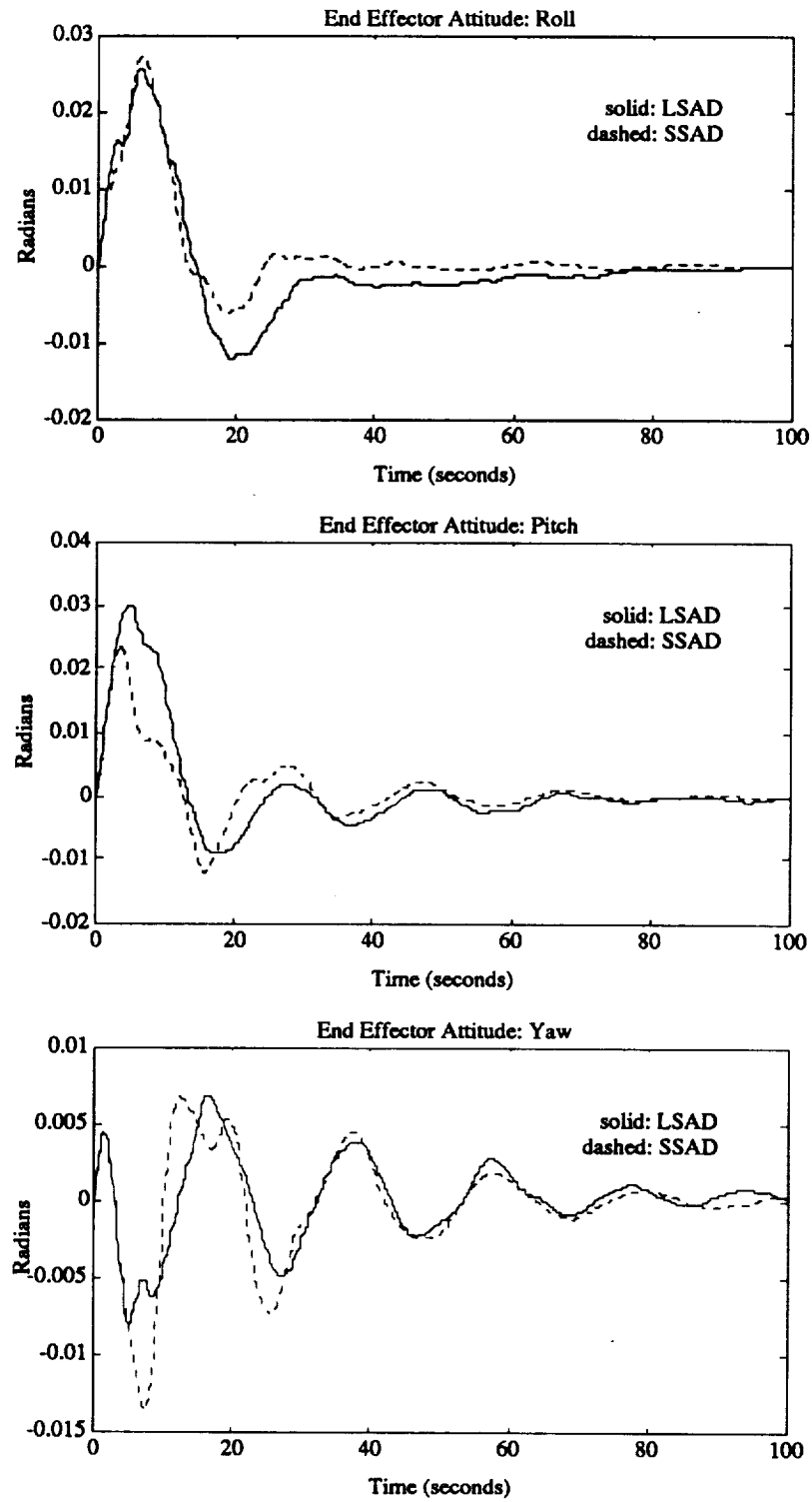


Figure 3.13. Rotational Response of LSAD and off-nominal SSAD to an Initial Velocity

Chapter 4

Design and Analysis Approach

The 24 state linearized model of the SRMS developed in Chapter 3 is used in subsequent Chapters for regulator design using three techniques: LQR, H_2 , and H_∞ optimization. Before any of these techniques are pursued, it is appropriate to consider the characteristics of the open-loop plant and their possible effects on the design process. This Chapter examines several aspects of the plant and anticipates how some can cause problems in both the design and analysis process¹. Stability and performance criteria upon which each regulator design are evaluated is introduced as well.

Section 4.1 examines the open-loop plant and suggests advantages of precompensation loop closure. Model reduction is applied to the open-loop plant to reduce it to 18 states, thereby reducing the order of any resulting compensator. The singular values of the reduced order system are compared to the full order system. The poles and transmission zeros of the reduced order plant are evaluated. Issues such as controllability and observability are also considered.

Section 4.2 concentrates on analysis of the open-loop plant. The criteria considered are the same that are applied to each compensator design in order to provide a common measure for evaluation. The singular values of the transfer functions from disturbance to end effector position and attitude are inspected. The transfer function from disturbance to control effort is scrutinized as well. In face of the parametric uncertainty present in SSAD, robust stability is considered via the small gain theorem. As a less conservative method, the structured singular value, μ , is also used in analysis. Due to the nature of the uncertainty, μ -analysis is still

¹This may seem like foresight in the thesis, though it is actually hindsight in the research.

conservative. The impact this will have on the analysis process is explored as well.

4.1 Obtaining a Design Plant

The first inclination when designing a new compensator for a system is to remove the old compensator and then proceed to the design process with the resulting open-loop plant. Such an open-loop plant was presented in Figure 3.5. The poles of this open-loop plant are plotted in Figure 4.1. With no feedback to the system, as expected, there are six poles residing at the origin. These rigid body modes, though not welcome, would be accepted except that computationally they do not appear exactly at the origin. Machine precision places them at some small ϵ on either side of the $j\omega$ -axis. This ϵ propagates through the design process causing computational problems later.

One method of dispensing with this dilemma is to leave the joint angle feedback loop intact. The current Position Hold controller as shown in Figure 3.9 consists of only a gain matrix. Leaving the current Position Hold loop in place and designing around it can be thought of as precompensation loop closure. Since there are no dynamics associated with the Position Hold gains, designing around them will not increase the order of a resulting compensator. There are several advantages to this precompensation loop closure.

Each joint operating in the current Position Hold Mode behaves as a spring with damping; the joint angle feedback of Position Hold will pull the origin poles decisively into the left half plane. This not only alleviates the computational problems discussed above, but it also produces a non-singular system A matrix. Invertability of the system would allow for the application of loop-shaping techniques in the LQG/LTR methodology such as those presented in References [13] and [12]. Furthermore, when designing an enhancement to a system already in use, it is conceptually more palatable to design the upgrade as stability or performance augmentation such that the improvement will work around the current system rather than replacing it. If necessary, the augmentation to the software can be disabled leaving the original system intact.

For the reasons outlined above, the current Position Hold system is treated for all intents and purposes as the open loop plant. Henceforth, in all discussion of analysis of the open-loop plant, it is the original Position Hold system that is actually being considered. The poles of

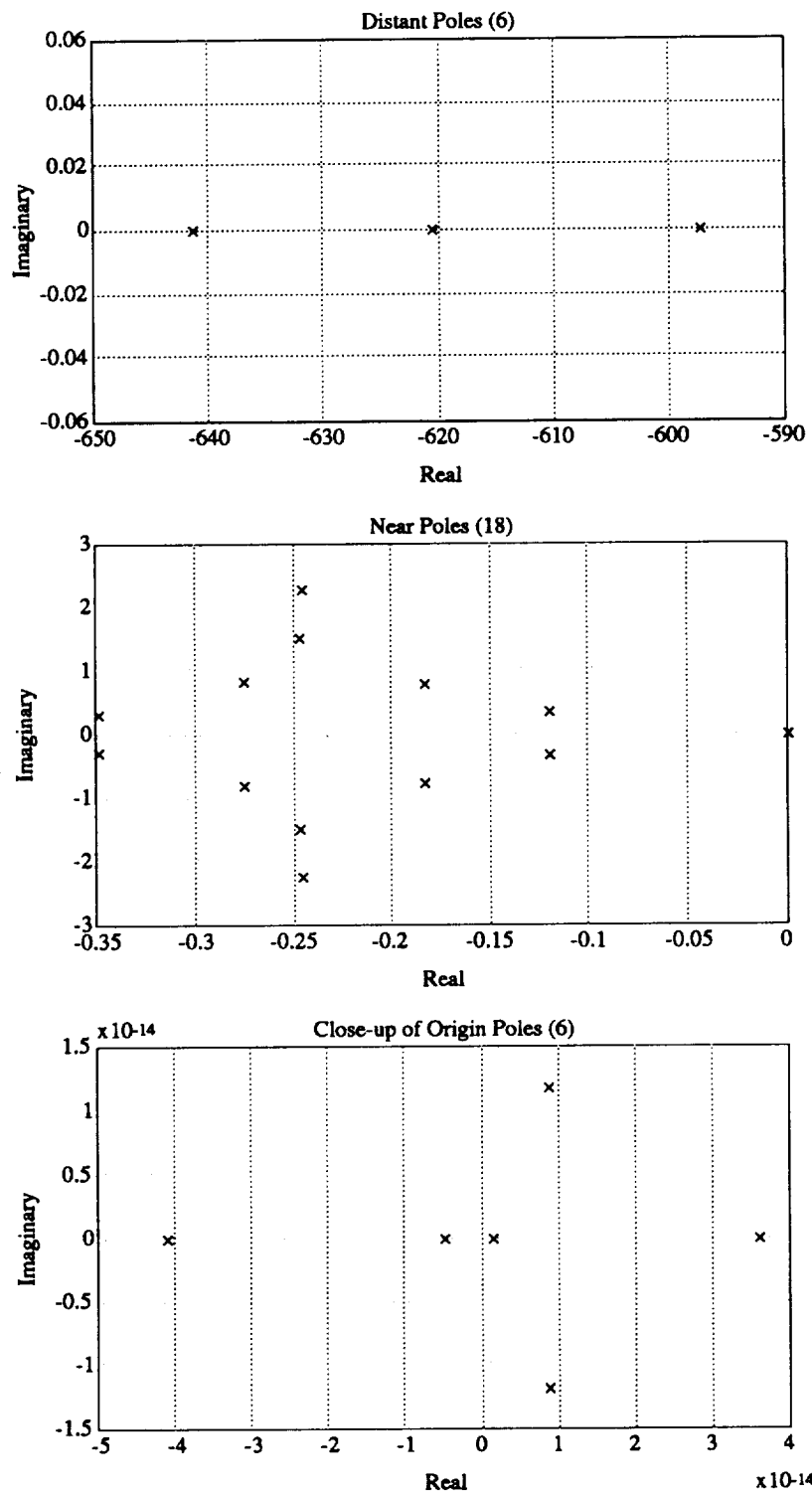


Figure 4.1. Poles of Open-Loop SSAD

this system are shown in Figure 4.2.

The six distant poles, which correspond to the dynamics of the motor rates, are considerably faster than the rest of the system. They are even faster than the fastest possible sample rate of 80 milliseconds in the actual system. Eliminating the fast poles will reduce the model to 18 states and thereby reduce the order of a compensator. As long as the bandwidth of a compensator designed from the reduced order model (ROM) is kept relatively small, there will be no interference. To insure problems do not occur with performance or stability as a result of the model reduction, the ROM is used for controller design purposes only. The full order model (FOM) is always used in analysis. This will isolate stability robustness problems to the parameter uncertainties rather than confusing the issue with neglected dynamics. Section 4.1.1 examines a method for eliminating the fast dynamics of the system, while Section 4.1.2 explores the characteristics of the ROM and compares it to the FOM.

4.1.1 Model Reduction

Denote the transfer function from joint rate commands to end effector position and attitude as

$$G(s) := (A, B, C, D)$$

This can be decomposed as

$$G(s) = [G(s)]_s + [G(s)]_f \quad (4.1)$$

where

$$[G(s)]_s := (\hat{A}_{11}, \hat{B}_1, \hat{C}_1, \hat{D}_1)$$

represents the slow modes of the system, and

$$[G(s)]_f := (\hat{A}_{22}, \hat{B}_2, \hat{C}_2, \hat{D}_2)$$

represents the fast modes to be cut from the system. Finding the matrices which define the decomposed system requires the use of the algorithm presented in Reference [14] in the manner outlined below:

Using an ordered Schur decomposition, find a unitary matrix, V such that

$$A = VAV' = \begin{bmatrix} \hat{A}_{11} & \hat{A}_{12} \\ 0 & \hat{A}_{22} \end{bmatrix} \quad (4.2)$$

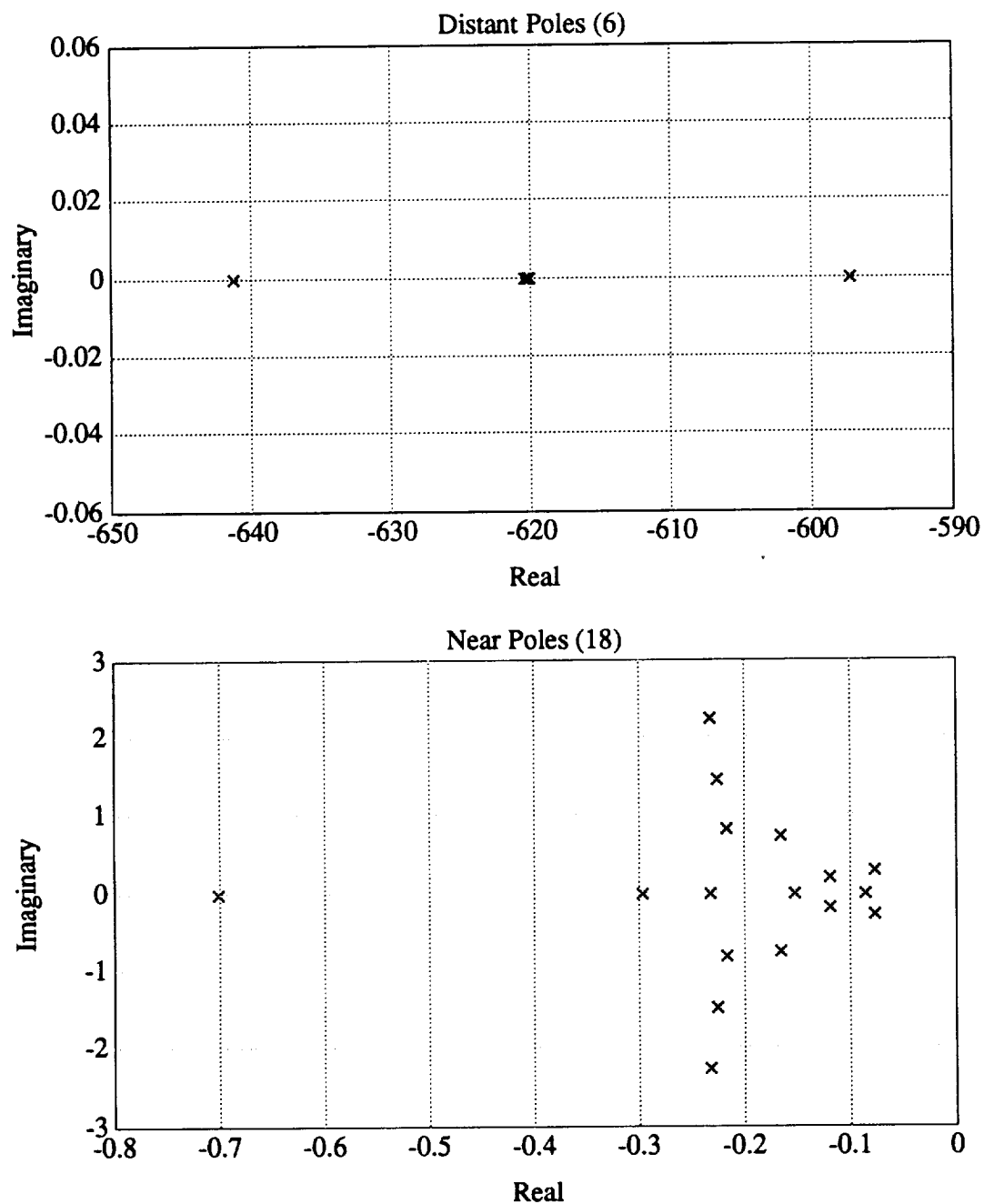


Figure 4.2. Poles of the Position Hold Open-Loop SSAD

Consider λ_i to be the i^{th} eigenvalue of some matrix, A . Using the ordered Schur form, one can find \hat{A}_{11} and \hat{A}_{22} such that

$$|\lambda_i(\hat{A}_{11})| < |\lambda_i(\hat{A}_{22})| \quad (4.3)$$

For SSAD, the system is divided into its 6 fast modes and 18 slow modes. Next, solving the following equation for X

$$\hat{A}_{11}X - X\hat{A}_{22} + \hat{A}_{12} = 0 \quad (4.4)$$

and then computing

$$\begin{bmatrix} \hat{B}_1 \\ \hat{B}_2 \end{bmatrix} = \begin{bmatrix} I & -X \\ 0 & I \end{bmatrix} VB \quad (4.5)$$

and

$$[\hat{C}_1 \ \hat{C}_2] = CV' \begin{bmatrix} I & X \\ 0 & I \end{bmatrix} \quad (4.6)$$

one arrives at the state-space forms

$$[G(s)]_s := \left[\begin{array}{c|c} \hat{A}_{11} & \hat{B}_1 \\ \hline \hat{C}_1 & D \end{array} \right] \quad (4.7)$$

$$[G(s)]_f := \left[\begin{array}{c|c} \hat{A}_{22} & \hat{B}_2 \\ \hline \hat{C}_2 & 0 \end{array} \right] \quad (4.8)$$

Notice that the full DC term of the system, D , is preserved in the slow system. Removing the 6 fast poles in this manner reduces the system to 18 states. The next Section will examine what information is lost in the reduction process and explore what effect this will have on design.

4.1.2 Characteristics of the ROM

Figure 4.3 plots the singular values of the ROM and the FOM. No information is lost until well beyond the bandwidth of the open-loop system. In the lower frequency range where the

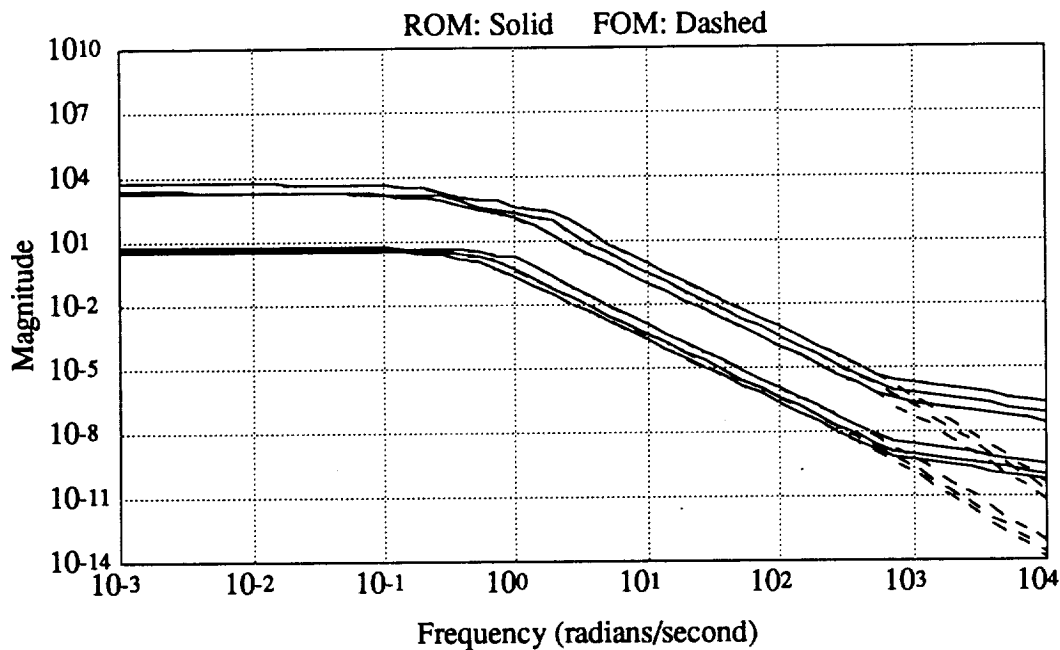


Figure 4.3. Singular Values from Joint Rate Commands to End Effector State for the ROM and FOM

system has significant gain, the two models are identical. Whatever DC effect the fast poles of the FOM had on the system is preserved in the reduction process. Also evident from the singular value plots is the poor scaling of the system. This can be seen from the distance between individual singular values. This ill-scaling is to be expected since the end effector state vector is comprised of translations measured in inches, and rotations measured in radians. Certainly scaling must be applied before design so that a regulator will not consider a one inch error and a one radian error with equal gravity.

Figure 4.4 displays the poles of the ROM. The 18 poles of the ROM reside in the same locations as the near poles of the FOM as shown in Figure 4.2; as desired, the fast dynamics have been eliminated.

Figure 4.5 bears silent witness to the fact that the model is non-minimum phase. Note, however, that all of the transmission zeros are exceedingly fast relative to the rest of the system.

We can study the controllability and observability properties of the system since SSAD in its nominal configuration is a linear time-invariant system. Consider the following gramians:

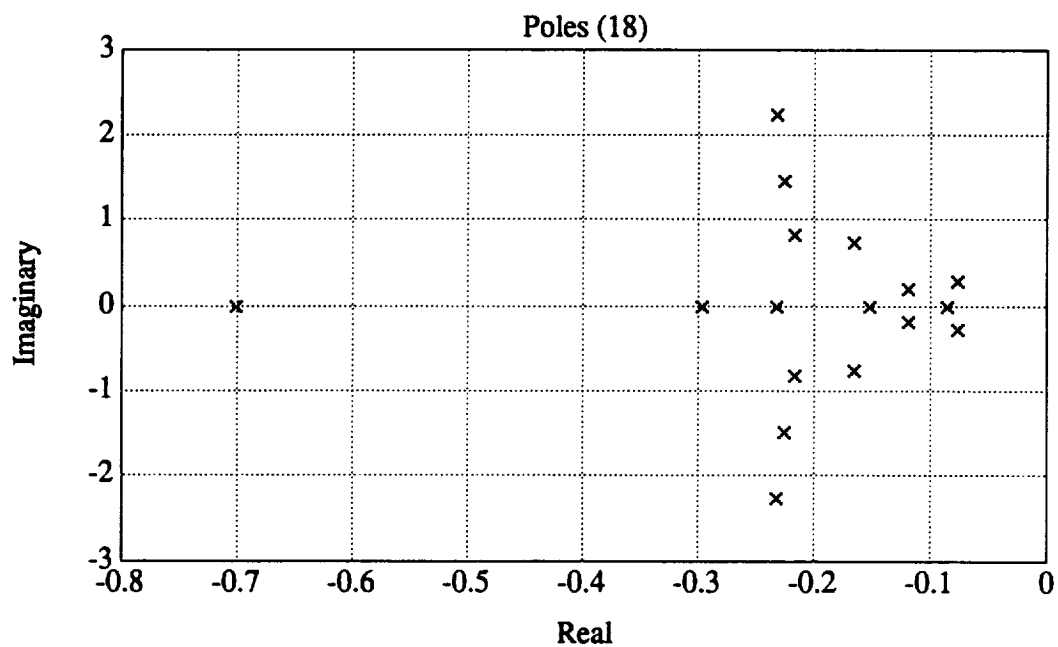


Figure 4.4. Poles of the Reduced Order Model

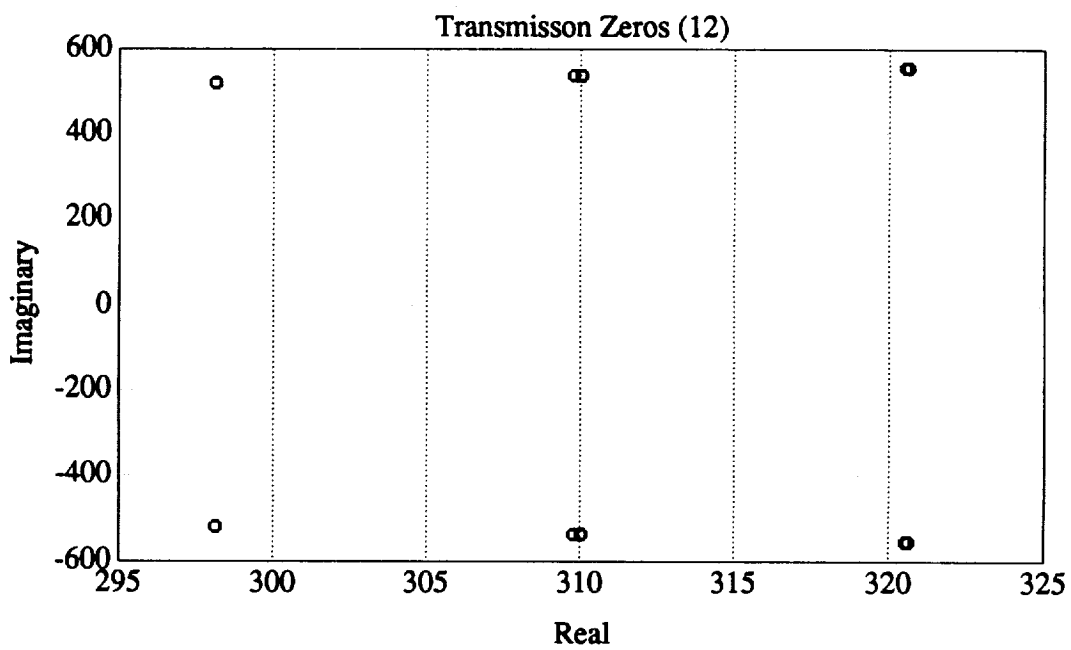


Figure 4.5. Transmission Zeros of the Reduced Order Model

A necessary and sufficient condition for controllability is that the controllability gramian

$$L_c(t) = \int_0^t \{e^{At} B B^T e^{A^T t}\} dt \quad (4.9)$$

must be full rank. Dually, a necessary and sufficient condition for observability is that the observability gramian

$$L_o(t) = \int_0^t \{e^{A^T t} C^T C e^{At}\} dt \quad (4.10)$$

must be full rank. If t is allowed to go to infinity and A is stable, then L_c and L_o can be found via the following Lyapunov equations:

$$A L_c + L_c A^T + B B^T = 0 \quad (4.11)$$

$$A^T L_o + L_o A + C^T C = 0 \quad (4.12)$$

Evaluating these gramians for the ROM ascertains the system to be fully controllable and observable. Recall that the end effector position and attitude are the measurements used for the new regulator designs. The controls are the six joint rate commands. Table 4.1 presents the singular values for the controllability and observability gramians. Though the system is fully controllable and observable to machine precision, this can be slightly misleading. Looking at Table 4.1 some modes are clearly more controllable and/or more observable than others. This implies that certain modes may require exorbitant amounts of control effort if they are to meet certain performance requirements. Fortunately, however, all of the modes are stable.

All of these issues are important to keep in mind during the design process. There will be limits to how far certain poorly controllable poles can be placed because of restrictions on the control effort. Keep in mind that the reduced order model presented in this Section will only be used for design purposes, the full order model will be used for analysis.

4.2 Analysis Techniques and the Open-Loop Plant

Before proceeding to design a new regulator to augment the performance of the current Position Hold controller, let us consider Position Hold performance as it stands now. This Section will analyze the current system following a threefold path. First, Section 4.2.1 considers the transfer function from disturbance to end effector position and attitude respectively to determine system performance. Second, Section 4.2.2 examines the transfer function from

Table 4.1. Gramian Singular Values

Controllability Gramian Singular Values		Observability Gramian Singular Values	
2.0767e+07	2.1420e+05	7.0207e+05	1.4658e-01
2.0295e+07	1.3638e+05	3.6847e+05	7.7801e-02
7.1140e+06	8.5671e+04	1.0944e+04	3.8524e-02
1.8852e+06	6.6693e+04	4.3336e+00	3.4467e-02
1.8332e+06	4.7181e+04	1.7348e+00	1.6510e-02
1.4352e+06	2.6289e+04	1.2482e+00	4.7992e-03
9.2866e+05	2.7779e+00	4.8469e-01	9.0874e-04
3.5116e+05	1.1020e+00	2.6327e-01	2.4196e-04
2.6732e+05	8.8740e-01	1.7180e-01	1.5619e-05

disturbance to control effort in order to establish how much control effort is required. Finally, Section 4.2.3 looks at the stability robustness of the system. This method of system analysis is the same procedure applied to every new controller designed in subsequent Chapters.

4.2.1 Performance

In evaluating the effect of a disturbance on the end effector state, only the rotational Shuttle commands are considered since the effect of fictitious translational jets were added only so that mathematically every state would have process noise. In fact, for Shuttle RMS operations, translational commands are prohibited. As pointed out in Section 3.2.2, the disturbance is normalized to lie between -1 and 1; let us consider the singular values from disturbance to the end effector in two sets. The first set will include the end effector position in inches and the second set will consist of the end effector attitude in radians. In this manner the singular values will retain their units making the evaluation of performance an easier task. Figure 4.6 displays these two sets of singular values for the current Position Hold regulator.

From Figure 4.6 we can see that the end effector excursion from equilibrium can be as great as 5 inches in position and as much as 0.03 radians in attitude for certain Orbiter rotation command directions. The goal in designing a new regulator is to bring these maximum excursions down as far as possible without exceeding the limitations on the control effort described in the next Section. Ideally we aim for less than 1 inch excursion in position and less than 0.01 radians of rotation excursion.

4.2.2 Control Effort

There are already in place certain joint rate command limits, ie., limitations on the control effort. These limits are not based on any hardware constraints, rather they are safety settings to insure a payload at the end effector isn't commanded too rapidly bringing the system into precarious areas of operation. These settings are a function of the payload inertia. The limits are calculated to maintain a prescribed stopping distance when operating the RMS. If new controllers can exhibit improved capability to control the end effector, there may be justification for increasing the joint rate limits.

For design purposes, the joint rate limits will be treated as hard constraints that must

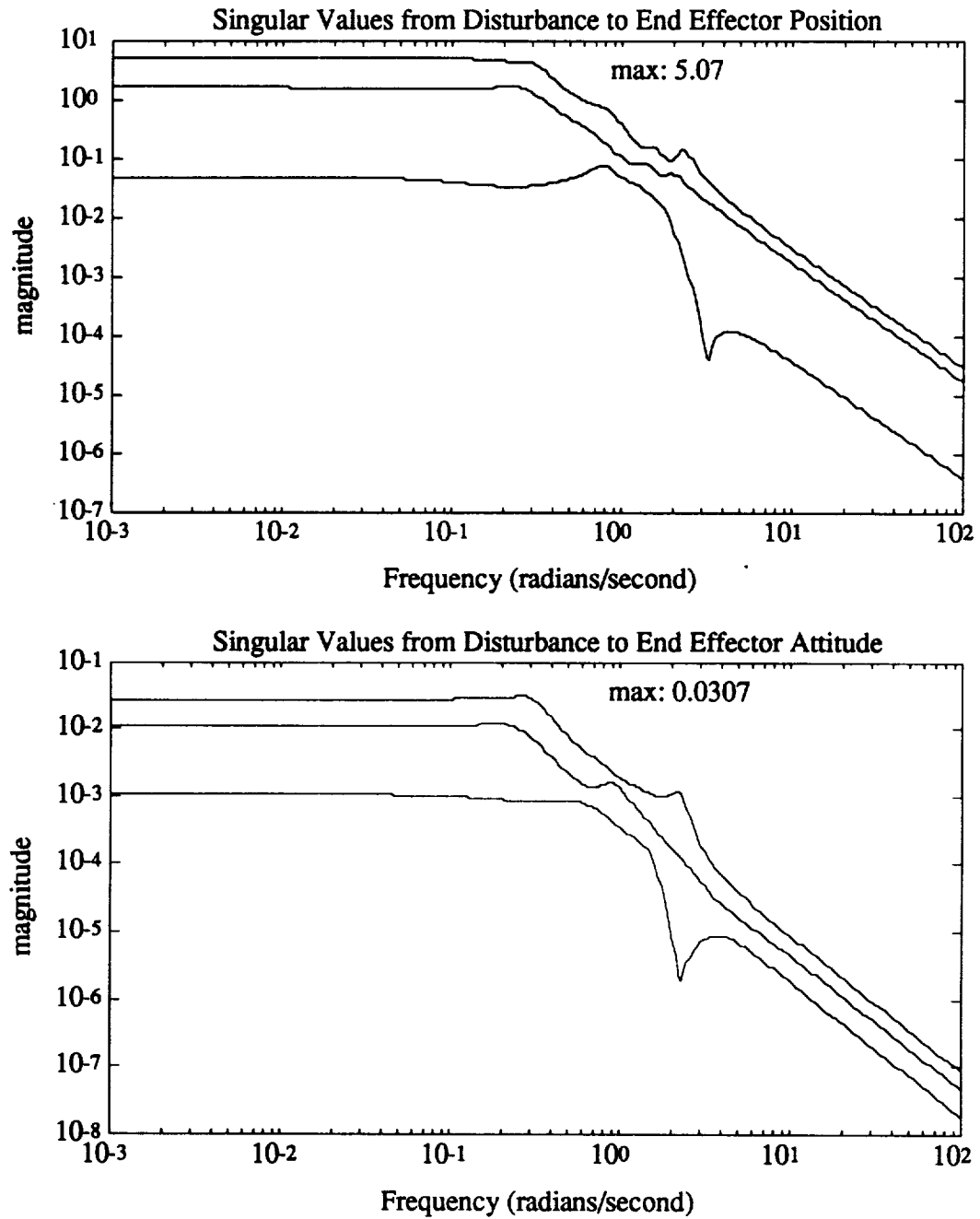


Figure 4.6. Performance Singular Values of the Current Position Hold System

Table 4.2. Joint Rate Limits

Joint	Joint Rate Limit (rad/sec)
Shoulder Yaw	0.0052
Shoulder Pitch	0.0052
Elbow Pitch	0.0072
Wrist Pitch	0.0107
Wrist Yaw	0.0107
Wrist Roll	0.0107

be met. In this manner, the lower bound on performance will be established. Increasing the joint rate limits will allow a new controller to use more control and thus allow performance to improve. Table 4.2 presents the current joint rate limits.

To determine the control effort used by the system for a disturbance caused by Shuttle attitude thruster firings, consider the singular values of the transfer function from the attitude firings to each individual joint rate command. There are six joints and six different joint rate limits. Let us scale each joint rate command by its corresponding joint rate limit. In this fashion, as long as the singular values of these six transfer functions remain below unity, the joint rate limits have not been exceeded. As Figure 4.7 shows, the current system is safely below the joint rate limits.

Keep in mind that all performance and control effort analysis performed so far has been on the nominal plant. Recall there are two parameters, K_{MA} and K_G , that include additive uncertainty. The next issue to consider is robust stability in face of this uncertainty.

4.2.3 Stability Robustness

Recall the standard form for a compensated plant with uncertainty shown in Figure 3.8. The closed-loop version of this is shown in Figure 4.8. $G(s)$ is the closed-loop transfer function which combines the dynamics of the plant and the compensator and Δ is the modeling uncertainty.

The closed-loop transfer function, $G(s)$, can be divided into a set of four transfer functions as follows,

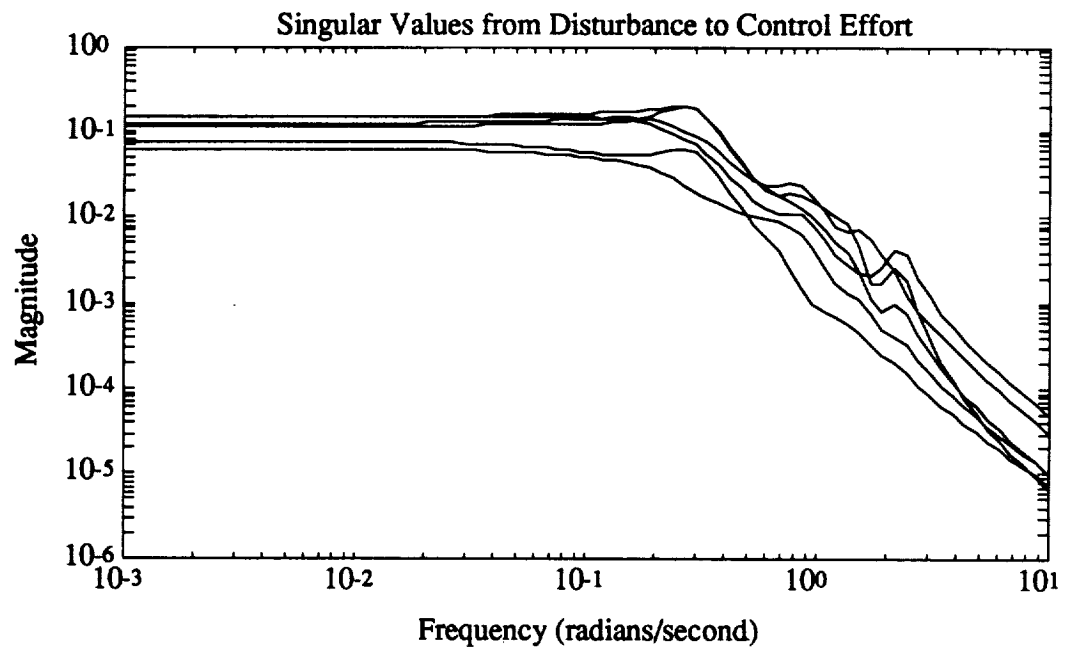


Figure 4.7. Control Effort Singular Values of the Current Position Hold System

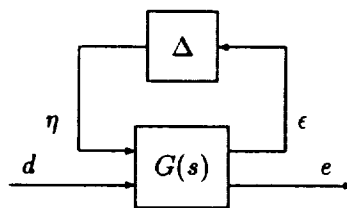


Figure 4.8. Closed-Loop Transfer Function

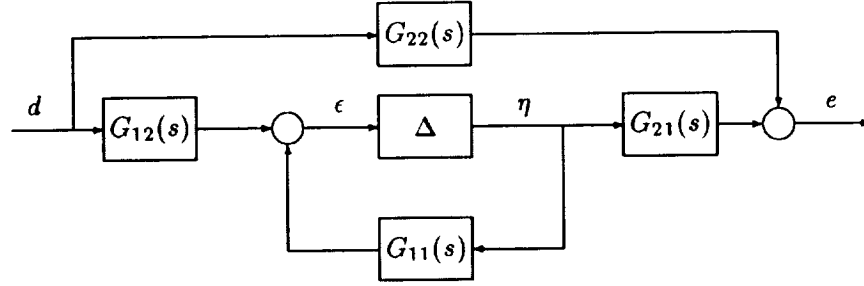


Figure 4.9. Closed-Loop System for Robust Stability Analysis

$$\begin{bmatrix} \epsilon \\ e \end{bmatrix} = \begin{bmatrix} G_{11}(s) & G_{12}(s) \\ G_{21}(s) & G_{22}(s) \end{bmatrix} \begin{bmatrix} \eta \\ d \end{bmatrix} \quad (4.13)$$

In this representation, the nominal closed-loop system is given by $G_{22}(s)$. Let us redraw Figure 4.8 as shown in Figure 4.9. In this representation, looking at the Δ and $G_{11}(s)$ transfer functions, the small gain theorem can be invoked.

By invoking the small gain theorem, a sufficient condition for closed-loop stability is

$$\|G_{11}(s)\Delta\|_{\infty} < 1 \quad (4.14)$$

The H_{∞} norm is defined in the frequency domain for a stable transfer function matrix as

$$\begin{aligned} \|G(s)\|_{\infty} &\equiv \sup_{\omega} \bar{\sigma}[G(j\omega)] \\ &= \sup_{\|u\|_2 \neq 0} \frac{\|y\|_2}{\|u\|_2} \end{aligned} \quad (4.15)$$

Therefore, the H_{∞} norm is the induced 2-norm.

In Section 3.2.2, Δ was defined to be normalized to less than one. Therefore, Equation 4.14 can be reduced to

$$\|G_{11}(s)\|_{\infty} < 1 \quad (4.16)$$

This small gain test is valid for any complex Δ with norm less than one. However, for indepen-

dent modeling uncertainties, Δ is known to have a block diagonal structure

$$\Delta = \begin{bmatrix} \Delta_1 & 0 & \dots & 0 \\ 0 & \Delta_2 & & \vdots \\ \vdots & & \ddots & 0 \\ 0 & \dots & 0 & \Delta_m \end{bmatrix}$$

For the SSAD plant, there are two block diagonal elements for K_{MA} and K_G . Since the small gain test must hold for all normalized Δ , not just the more restricted set of normalized block diagonal Δ matrices, Δ_D , it is a conservative test. Because it is known the perturbations of SSAD are real parameter variations, testing for complex perturbations makes the small gain test even more conservative.

In an effort to supply a less conservative robust stability test, Doyle [15] developed the structured singular value, μ . μ is defined as

$$\mu[G(j\omega)] \equiv \begin{cases} 0 & \text{if } \det[I - G(j\omega)\Delta(j\omega)] \neq 0 \text{ for all } \Delta \in \Delta_D \\ \{\min_{\Delta \in \Delta_D} \bar{\sigma}[\Delta(j\omega)]\}^{-1} & \det[I - G(j\omega)\Delta(j\omega)] = 0 \text{ otherwise} \end{cases} \quad (4.17)$$

Consider $\mu[G_{11}(j\omega)]$. From the definition of μ , if $\mu[G_{11}(j\omega)] > 1$ at some frequency ω then there exists a block diagonal $\Delta(j\omega)$ such that

$$\bar{\sigma}[\Delta_i(j\omega)] < 1 \text{ and } \det[I - G_{11}(j\omega)\Delta(j\omega)] = 0$$

Conversely, if $\mu[G_{11}(j\omega)] < 1$ for all ω , then the smallest block diagonal Δ matrix that makes the system singular has the gain

$$\bar{\sigma}[\Delta_i(j\omega)] > 1$$

which violates the norm of the modeling error. Therefore, a necessary and sufficient condition for robust stability when $\Delta \in \Delta_D$ is

$$\mu[G_{11}(j\omega)] < 1 \quad \forall \omega \quad (4.18)$$

Unfortunately, in the actual application of μ -analysis we are reduced to conditions which are sufficient but not necessary for two reasons. First of all, μ is not a norm and it cannot be computed easily. Software is available that can calculate upper bounds for μ . However, using

an upper bound adds some conservatism to the analysis. The second source of conservatism again comes from the fact that SSAD has real parametric uncertainty. The set Δ_1 still allows for complex perturbations as in the small gain test. This is a particularly bothersome problem for the SSAD plant which contains lightly damped poles with large error. With lightly damped poles, even small complex perturbations can cause the condition for robust stability to be violated, ie., $\mu[G_{11}(j\omega)] > 1$. Consider the following simple example.

Example 4.1: Spring-Mass-Damper System with Uncertain Spring Constant

A spring-mass-damper system with a unit mass can be represented by the differential equation

$$\ddot{x} + c\dot{x} + kx = f \quad (4.19)$$

where c is the viscous damping coefficient given as 0.1, k is the spring constant, and f is a disturbance force. The spring constant is uncertain, but modeled to fall in the range

$$0.5 < k < 2.5$$

If k is selected in the center of its range for the nominal system, a state-space representation is given by

$$\begin{aligned} \begin{bmatrix} \dot{x}_1 \\ \dot{x}_2 \end{bmatrix} &= \begin{bmatrix} 0 & 1 \\ -1.5 & -0.1 \end{bmatrix} \begin{bmatrix} x_1 \\ x_2 \end{bmatrix} + \begin{bmatrix} 0 \\ 1 \end{bmatrix} [f] \\ \dot{x} &= Ax + Bf \end{aligned} \quad (4.20)$$

The nominal system has stable roots at $\lambda = -0.05 \pm 1.224i$. In fact, throughout the range of k the system remains stable with roots at $\lambda = -0.05 \pm 0.705i$ for the high end of the range and roots at $\lambda = -0.05 \pm 1.5803i$ for the low end of the range. The system is robustly stable in face of the parametric uncertainty. Nevertheless, since μ -analysis will consider complex perturbations, this system will fail the μ test for stability.

Consider, as an example, the perturbation matrix

$$\Delta A = \begin{bmatrix} 0 & 0 \\ i & 0 \end{bmatrix}$$

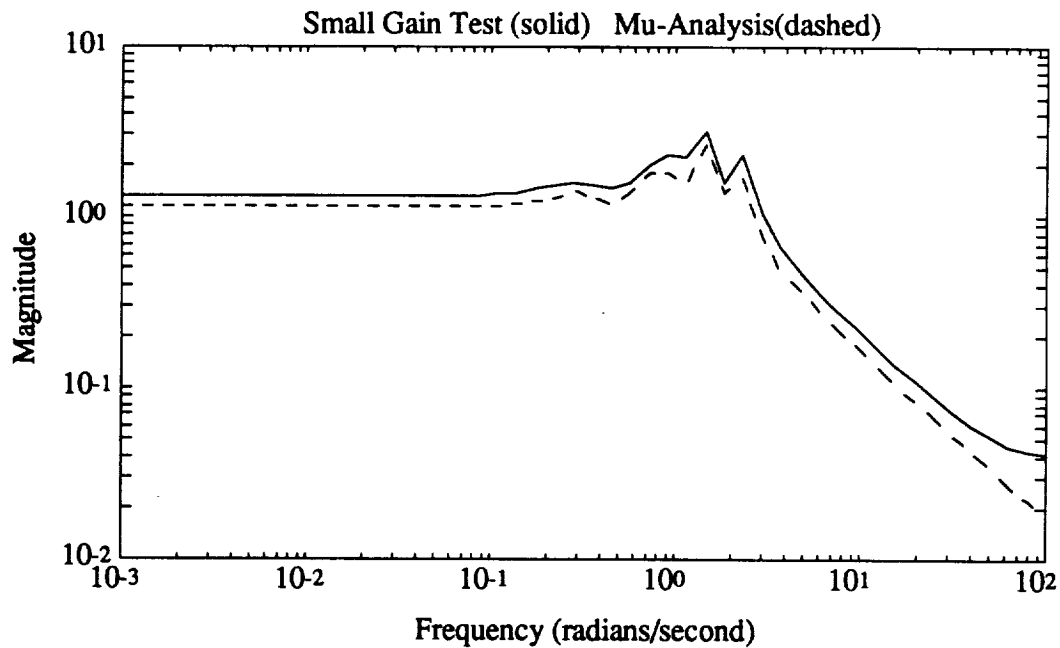


Figure 4.10. Robust Stability Analysis of the Current Position Hold System

whose norm is one. Though this perturbation cannot occur in the real system, μ -analysis will test for such a Δ . This perturbation places the roots at $\lambda_1 = 0.3394 + 1.284i$ and $\lambda_2 = -0.4394 - 1.284i$ failing robust stability.

Though μ -analysis does not supply a necessary condition for robust stability, it does reduce conservatism over the small gain test. To illustrate this, Figure 4.10 displays the results of the small gain test and μ -analysis performed on the current Position Hold controller. Though μ -analysis is less conservative than the small gain test, the plant still fails robust stability.

To determine if the instability displayed in Figure 4.10 is the result of a fictitious complex perturbation, or a configuration the system can actually realize, it is possible to evaluate the pole locations of the system for different parameter values. To analyze every possible combination of the twelve parameters would not be feasible; however, it is reasonable to check the endpoints.

Consider when the end effector is very close to its equilibrium position and attitude. At these very small amplitudes, the current limiter has not saturated, hence all six of the K_{MA} are at their maximum values. Furthermore, at very small amplitudes the joint angles and motor shaft angles are almost aligned, thus the six K_{Gi} are at their minimum values. Figure 4.11 displays the pole locations of the system with the parameters K_{MA} and K_{Gi} at these endpoints

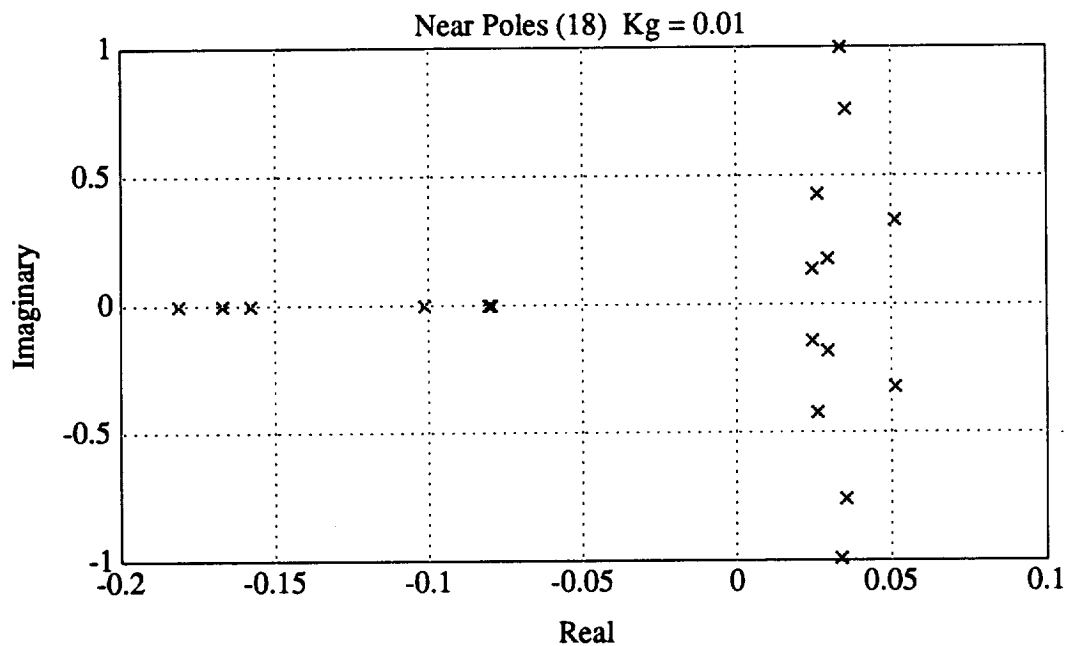


Figure 4.11. Open-Loop System Near Pole Locations With $K_G = 0.01$ and $K_{MA} = K_{MA_{max}}$

of their ranges.

As Figure 4.11 shows, the instability indicated by μ -analysis is not fictitious. The system is not robustly stable for the full range of values the parameters can inhabit. If all six K_{G_i} are increased in unison at 0.01 increments, the lowest values that achieve stability are 0.05. This value brings the system poles just to the left of the $j\omega$ -axis. This configuration is shown in Figure 4.12. Interpreting these observations indicates the SSAD plant is a system that is stable at moderate to high torque values when K_{G_i} is higher than 0.05 and unstable at very low torque values when K_{G_i} is below 0.05. Such a system would stably damp and then limit-cycle close to the equilibrium position; such behavior is observed in the actual system.

To totally eliminate this limit cycle behavior with a regulator may require a large sacrifice of performance. In any case, it would be misleading to think that eliminating such behavior with a regulator on our model would do so for the actual system. Recall that in Chapter 3 frictional effects were neglected in SSAD. Such effects would certainly contribute to the limit cycle behavior. This is something to keep in mind when designing new compensators. Instabilities caused by very low K_{G_i} may not be a problem since they indicate slow limit-cycling of small

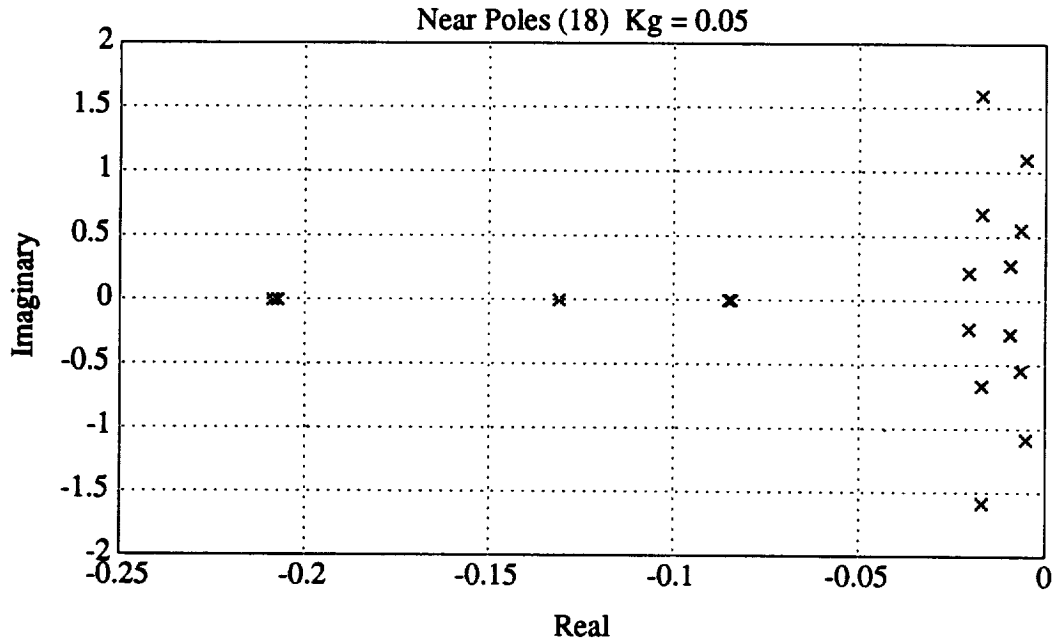


Figure 4.12. Open-Loop System Near Pole Locations With $K_G = 0.05$ and $K_{MA} = K_{MA_{max}}$ amplitude near the equilibrium values which is unavoidable.

4.3 Summary

In this Chapter, the 24 state SSAD model has been reduced to 18 states for design purposes only. The 24 state model will be used for analysis purposes. Three criteria that will be considered for each design are the performance singular values, the control effort singular values, and robust stability of the plant. The analysis process was carried out on the current Position Hold controller as both an example of the process and the baseline for comparison. In analyzing performance, two sets of singular values were examined: disturbance to end effector position as well as end effector attitude. Control effort was determined by looking at the singular values of the transfer function from disturbance to control effort. Finally, robust stability was determined via the small gain test, and the less conservative structured singular value, μ . μ -analysis may still be too conservative a test since the SSAD plant is restricted to real parametric variations. To determine this, we resorted to eigenvalue evaluation at certain parameter values.

Chapter 5

LQR Design

Linear Quadratic Regulator (LQR) design is very limited in its applications. This technique not only requires knowledge of every state, but also, this knowledge must be uncorrupted by any sensor noise. Since measurements of every state are not available, a linear quadratic regulator cannot be implemented on the actual SRMS without first designing an estimator to approximate the states. Nevertheless, it is useful to design a LQR because it gives an idea of the best we can hope to achieve in terms of minimizing the ‘2-norm’ of the error, $\|e\|_2$. It is a simple first step that helps to motivate the model-based compensator (MBC) designs. In MBC design techniques, the states of the system are estimated from the measurements. These estimates are then used by a compensator. MBC design techniques are the topics of subsequent Chapters.

The LQR technique is derived from optimal control theory. Kwakernaak and Sivan [16] provide the full details of this theory. Section 5.1 provides the main results of the LQR technique as it applies to the SRMS problem.

Section 5.2 analyzes the LQR for the SRMS using the techniques presented in Chapter 4. The performance and control effort singular values are examined and compared to the open-loop system. A time domain simulation of a typical jet firing pattern is also presented. Finally, stability robustness is examined in face of the parametric uncertainty.

5.1 LQR Theory

LQR theory provides no direct method to design for stability robustness or robust performance, thus for design purposes Figure 5.1 eliminates the Δ block of Figure 3.8. The effects of

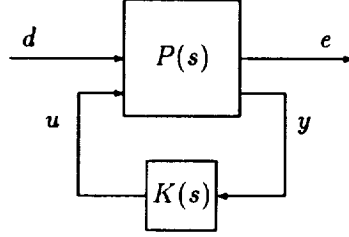


Figure 5.1. Plant With Compensator

the Δ block are considered after the design process is completed.

The general state-space representation of Figure 5.1 is

$$\begin{bmatrix} \dot{x}_p \\ e \\ y \end{bmatrix} = \begin{bmatrix} A_p & B_1 & B_2 \\ C_1 & D_{11} & D_{12} \\ C_2 & D_{21} & D_{22} \end{bmatrix} \begin{bmatrix} x_p \\ d \\ u \end{bmatrix} \quad (5.1)$$

In the LQR design methodology, uncorrupted full state feedback is called for. Thus the disturbance vector, d , does not include sensor noise, only the process noise. Furthermore, C_2 is the identity matrix. We will design the LQR compensator from the reduced order model presented in the last Chapter. For analysis, we will apply the reduced order compensator design on the full order plant. The result of an LQR design is well known to be a constant gain matrix, thus an LQR does not increase the order of the closed-loop system.

The error vector, e , includes the states and the controls.

$$e = \begin{bmatrix} x_p \\ u \end{bmatrix}$$

The states are weighted by a symmetric and positive semidefinite matrix, Q , while the controls are weighted by a symmetric and positive definite matrix, R . Additionally, the modelling performed in Chapter 3 produced no direct feedthrough term, thus $D_{22} = 0$. Hence for the LQR formulation of the SRMS, Equation 5.1 can be recast as

$$\begin{bmatrix} \dot{x}_p \\ e \\ y \end{bmatrix} = \left[\begin{array}{c|cc} A_p & B_1 & B_p \\ \hline Q & 0 & 0 \\ \hline 0 & I & 0 \end{array} \right] \begin{bmatrix} x_p \\ d \\ u \end{bmatrix} \quad (5.2)$$

The LQR problem is to devise a feedback control law which minimizes the quadratic cost functional

$$J = \int_0^\infty [x_p' Q x_p + u' R u] dt \quad (5.3)$$

The optimal feedback control law is

$$\begin{aligned} u &= -G x_p \\ G &= R^{-1} B_p' K \end{aligned} \quad (5.4)$$

where K is the symmetric, positive semidefinite solution of the algebraic Riccati equation

$$A_p' K + K A_p - K B_p R^{-1} B_p' K + Q = 0 \quad (5.5)$$

In general, there are many solutions to Equation 5.5, but only one of them is positive semidefinite. The gain matrix K will exist and be positive definite provided that the system $(A_p, B_p, Q^{\frac{1}{2}})$ is stabilizable and detectable. In other words, any uncontrollable or unobservable modes are asymptotically stable.

The closed-loop system dynamics become

$$\begin{aligned} \dot{x}_p &= A_p x_p + B_p u + B_1 d \\ u &= -G x_p \\ \dot{x}_p &= [A_p - B_p G] x_p + B_1 d \end{aligned} \quad (5.6)$$

Furthermore, the closed-loop system is guaranteed to be stable, ie.,

$$\text{Re} \lambda_i [A_p - B_p G] < 0 \quad \forall i \quad (5.7)$$

The exact pole locations will depend not only upon the open-loop system (through A_p and B_p), but also upon how the weighting matrices Q and R are selected. Thus Q and R are the design parameters that are tuned until a LQR design meets desired disturbance rejection and control effort requirements.

5.2 LQR Results

For the SRMS problem, the only states of concern are the ones corresponding to the end effector position and attitude. To express this desire, Q is selected as a matrix of zeros except for the values along the diagonal elements corresponding to the end effector position and attitude states.

Recall that the end effector position is measured in inches and the attitude is measured in radians. To scale the outputs, consider the singular values of the open-loop system as shown in Figure 4.6. The attitude maximum singular value is more than an order of magnitude below the position maximum singular value. The weights in Q are chosen to reflect this difference. The elements of Q corresponding to attitude are placed more than an order of magnitude above the position weights. In this manner a one inch error is not considered as serious as a one radian error. The actual values of the weights do not matter, only the ratio between them. Such a selection of Q also insures that the system $(A_p, B_p, Q^{\frac{1}{2}})$ is stabilizable and detectable.

In selecting R , certainly every control must be weighted to insure the joint rate limits are not violated. As shown in Table 4.2, we already know the limit of control demand considered acceptable. As a starting point, choose the inverse of the joint rate limits as the initial weight and then iterate over the design process, tuning R each time until the singular values from disturbance to control effort fall just below the joint rate limits for each control channel. This procedure will result in the best performance possible with the LQR design technique given the limits on the control effort.

Section 5.2.1 examines the control effort and performance singular values in the same manner as outlined last Chapter. A time domain simulation is included as well to help interpret the singular values. Section 5.2.2 examines the stability robustness of the LQR design.

5.2.1 LQR Control Effort and Performance

Figure 5.2 shows the singular values from disturbance to control effort after the iteration process. Each control weight is fine tuned until the scaled singular value falls just below one. Below 0.1 radians/second, the control effort has not changed much from the open-loop system. For disturbances occurring at 1 radian/second, the LQR system uses almost two orders of magnitude more control than the open-loop system. Nevertheless, the LQR system does not

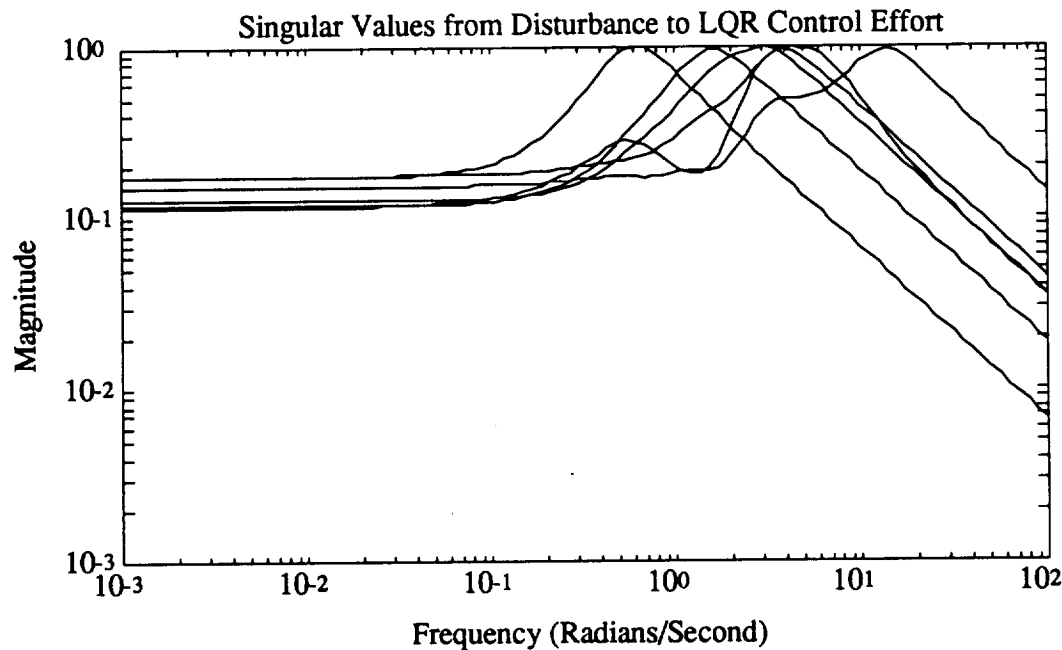


Figure 5.2. Control Effort Singular Values of the LQR System

exceed the joint rate limits.

Figure 5.3 presents the singular values from disturbance to end effector position and attitude. Included on the same plots is the corresponding information for the open-loop system. For the LQR design we were able to meet the performance goal of less than 1 inch excursion in position. This is expressed by the maximum singular value falling below one for all frequencies. Thus for any input disturbance, its effect on the end effector position will be multiplied by a gain at least less than one. Since the input disturbance is already normalized to fall between -1 and 1, the maximum excursion of the end effector position is less than one inch. Similarly, since the maximum singular value for the disturbance to attitude transfer function falls below 10^{-2} we have guaranteed less than 0.01 radians of rotation excursion. Both goals are met without exceeding the joint rate limits.

To better visualize what is occurring on the singular value plots, a time domain simulation is presented in Figures 5.4 and 5.5. These figures include both the response of the open-loop system and the LQR system. In this simulation a roll command is given for a full 10 seconds immediately followed by a 10 second pitch command and finally a 10 second yaw command.

From Figure 5.4 we can see that the X direction has considerably poorer disturbance re-

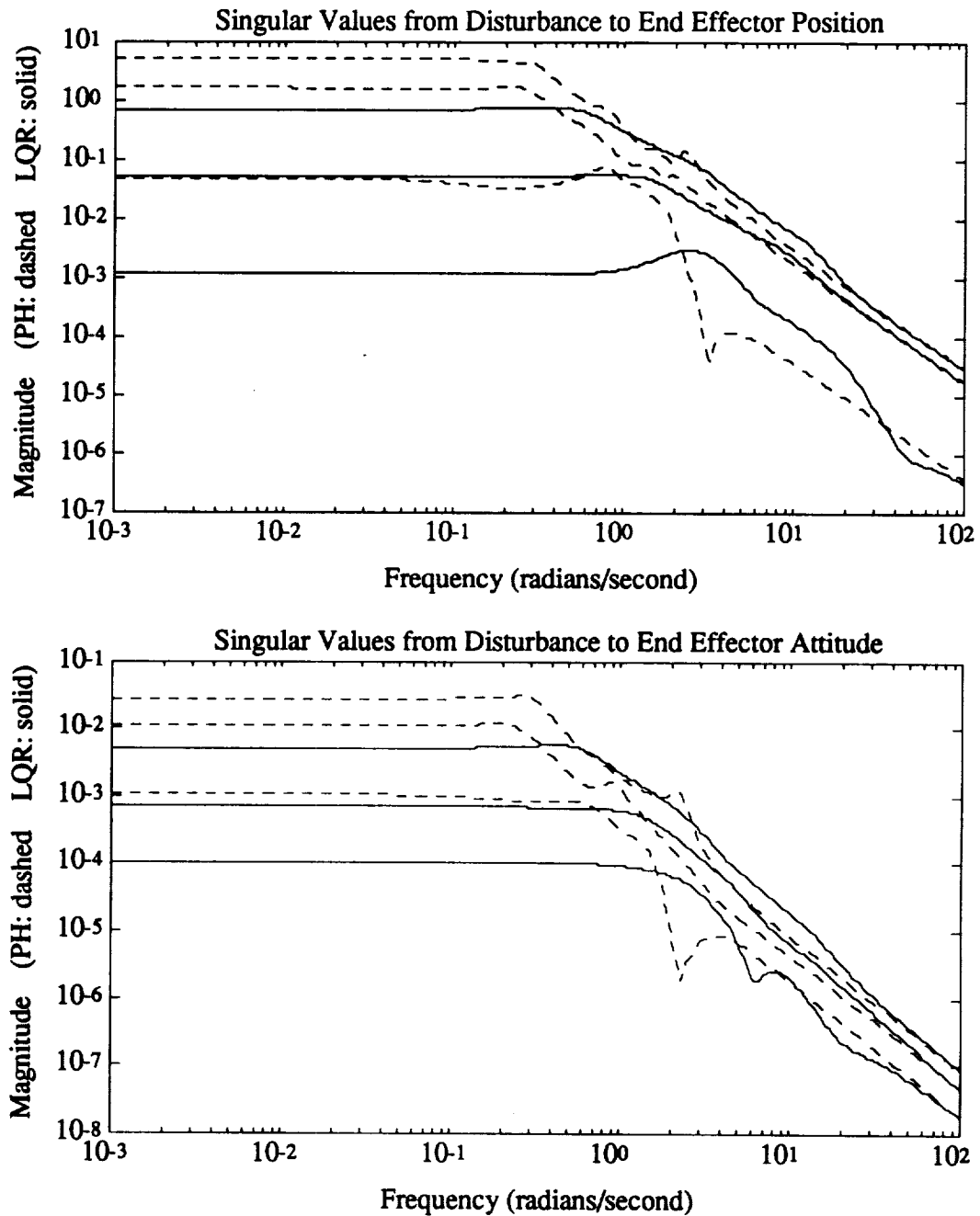


Figure 5.3. Performance Singular Values of the LQR System

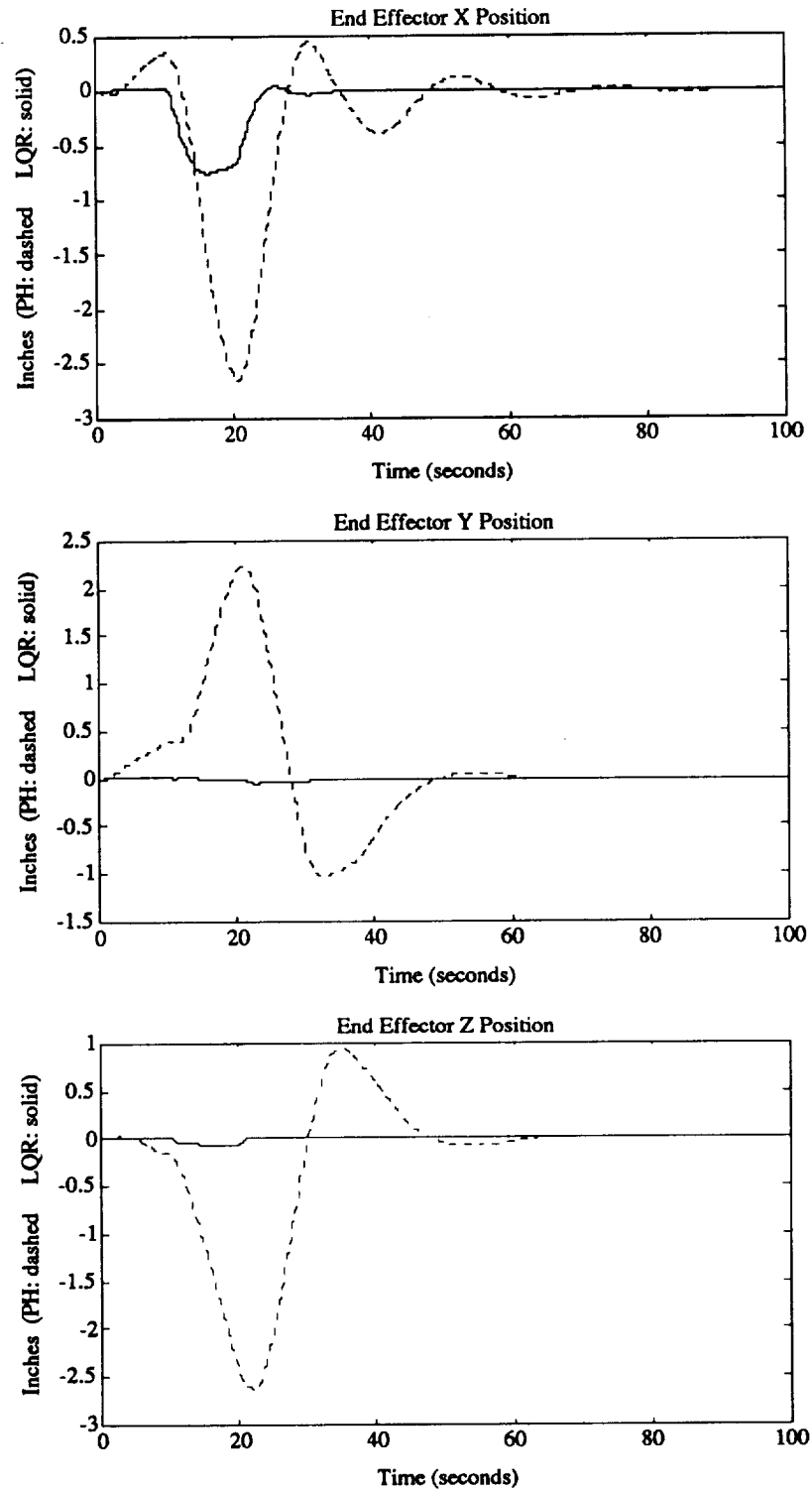


Figure 5.4. Translational Response of PH System and LQR System to Attitude Thruster Commands

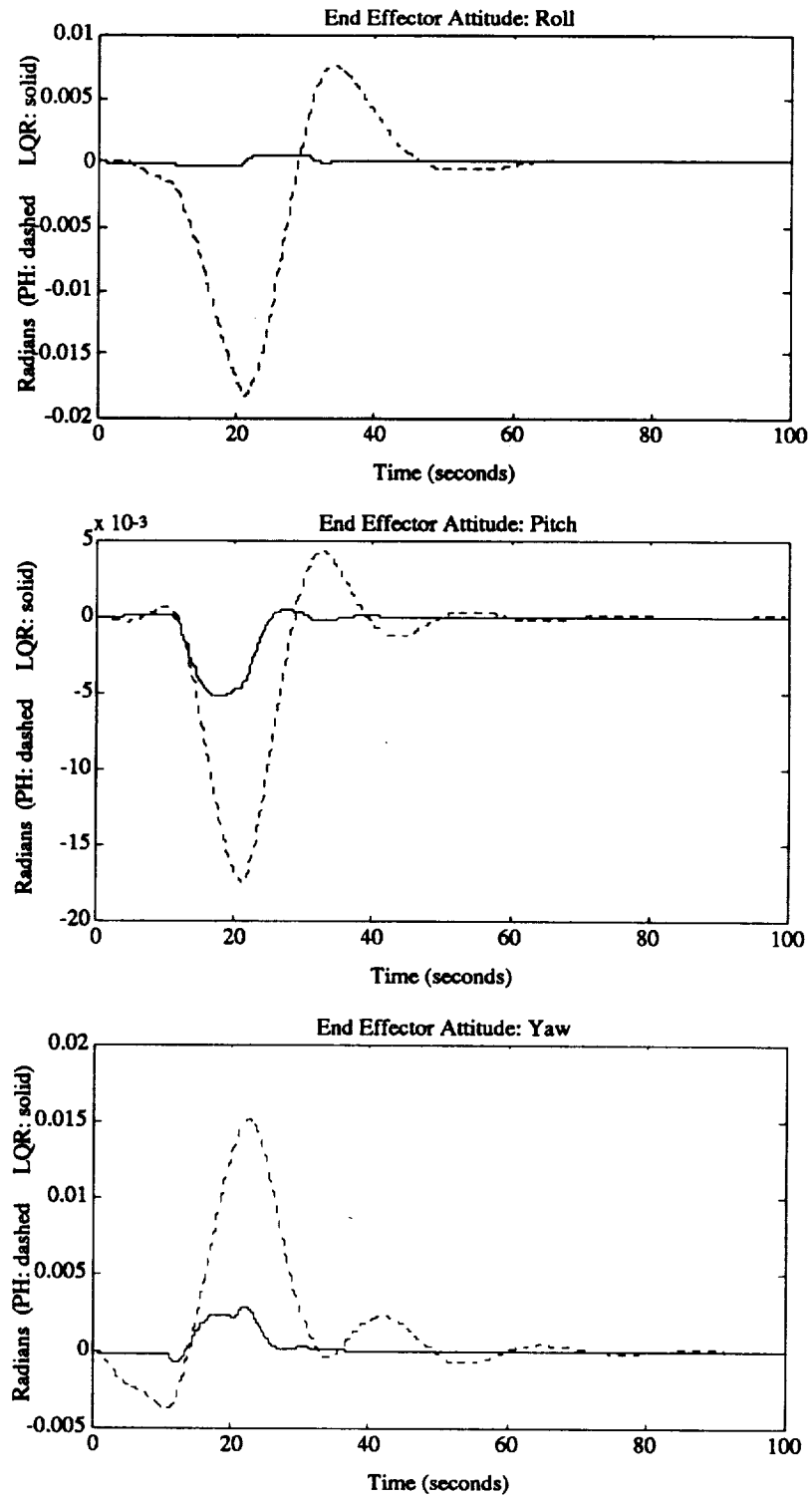


Figure 5.5. Rotational Response of PH System and LQR System to Attitude Thruster Commands

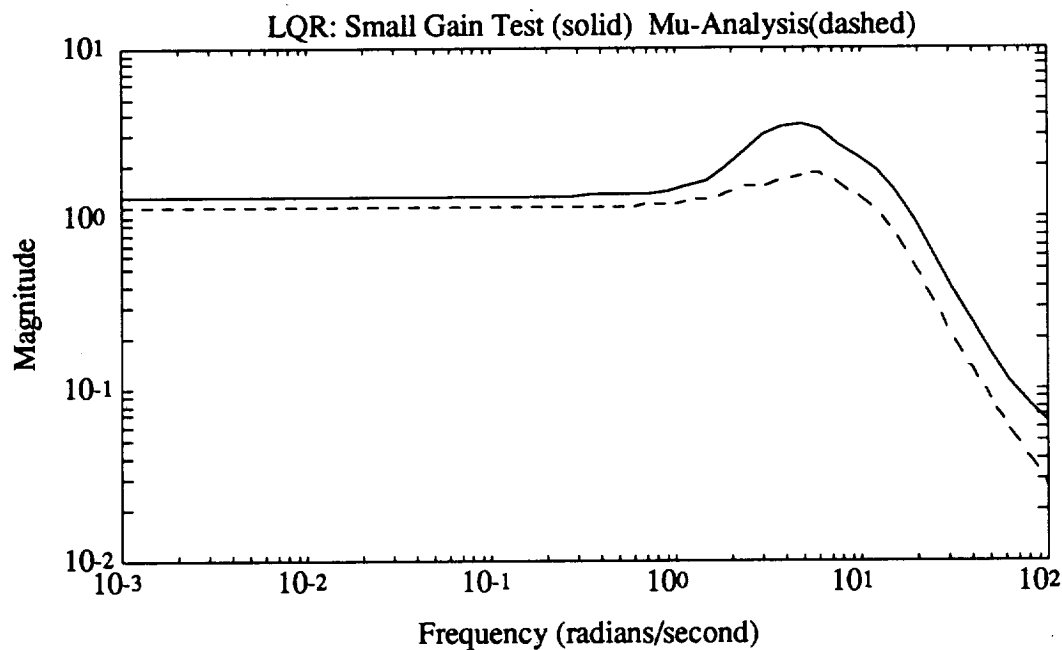


Figure 5.6. Robust Stability Analysis of the LQR System

jection than the Y and Z directions. Nevertheless, significant improvement over the uncompensated system is also apparent. Similarly, roll disturbance rejection is considerably better than the other axes as shown in Figure 5.5. These plots indicate that while in HST release configuration, the SRMS can reject disturbances much easier in some directions over others.

5.2.2 LQR Stability Robustness

Applying both the small gain test and μ -analysis to the closed-loop LQR system results in Figure 5.6. Unfortunately the system fails both tests. Recall as outlined last Chapter that both tests are conservative for SSAD since the uncertainties are real parameter variations. Therefore it is possible that the system is in fact robustly stable in face of the uncertainty though it cannot be shown.

Last Chapter, to confirm the results of μ -analysis, we evaluated the eigenvalues of the open-loop system for different parameter values. This technique conclusively showed that the open-loop system was in fact not robustly stable. As before, we can evaluate the eigenvalues of some combinations of the parameters to further our information on robust stability.

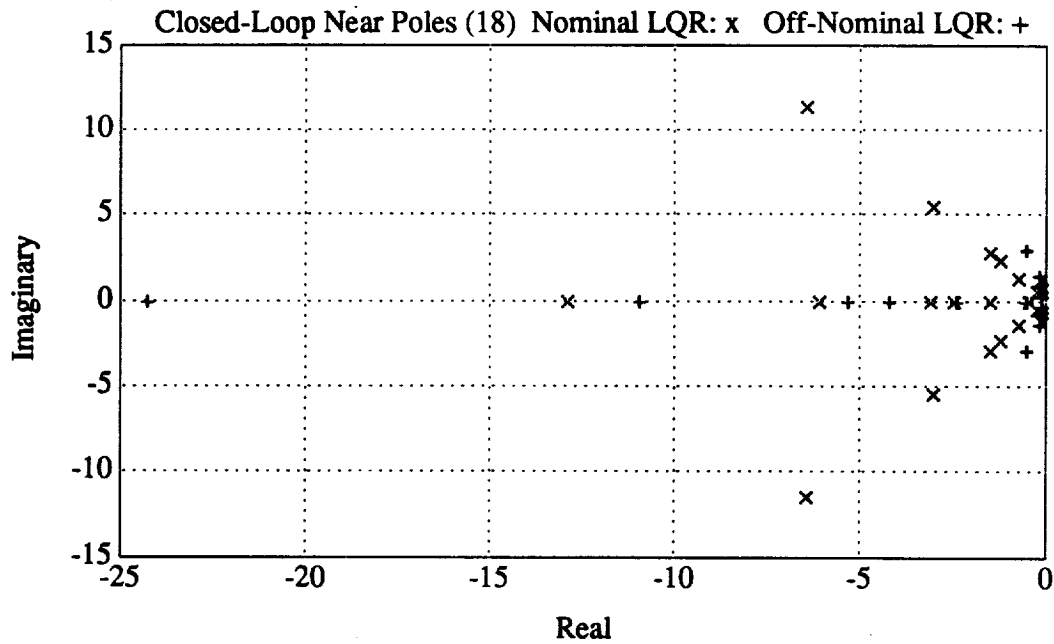


Figure 5.7. LQR Closed-Loop System Near Pole Locations for the Nominal and Off-Nominal System

Consider the twelve parameters in two sets, the K_{MA} and the K_G . After checking the four combinations of these two sets at the endpoints of their ranges, as we discovered with the open-loop plant, the worst possible combination is found to be the K_{MA} at the top of their range and the K_G at the bottom of their range. The worst combination is defined to be the system in which the closed-loop poles reside closest to the $j\omega$ -axis, or furthest into the right half plane. Figure 5.7 presents the LQR closed-loop near poles of the nominal plant and the worst off-nominal plant.

For these combinations, the system remains stable. Let us qualify this immediately; this does not prove robust stability. Though experimentation seems to indicate that the combination of the K_{MA} at the top of their range and the K_G at the bottom of their range is the system's worst, we cannot prove this conclusively. This is a multi-variable system with twelve varying parameters. There can be some other combination of parameters not considered that will result in an unstable closed-loop system.

To further dampen our spirits, keep in mind that several nonlinearities have been totally eliminated in the development of SSAD. Thus even if robust stability is guaranteed on the

model, it is not guaranteed on the actual system. We will not bypass the extensive pre-flight simulation requirement of a Shuttle mission.

5.3 Summary

Using the LQR technique, we have designed a compensator that is capable of meeting the performance objectives within the allowable control effort. The resulting regulator fails robust stability analysis via both the small gain test and μ -analysis. However, actual eigenvalue evaluation with four combinations of the parameters at their endpoints seems to indicate that the system may be robustly stable. Unfortunately, this cannot be proven unequivocally.

There are several drawbacks to the LQR technique. This technique not only requires knowledge of every state, but also, this knowledge must be uncorrupted by sensor noise. These requirements render an LQR design impractical for implementation of the actual SRMS. An estimator would be required to determine the states for the LQR. This would add noise to the state feedback vector which the LQR does not account for. If an estimator must be designed, it is better to use an optimal design method such as the LQG technique.

Chapter 6

H_2 Design

Last Chapter we saw that with full state feedback, performance goals were met without exceeding the control effort limitations. However, in the actual system we are limited to an observation vector, y , which is some linear combination of the states corrupted by noise. The solution to this more involved problem is given by the Linear Quadratic Gaussian (LQG) theory studied extensively in the 1960's and 1970's. The LQG solution is realized via the separation principle. The problem is reduced to two sub-problems, the solutions to which are well known.

The first sub-problem is to obtain an estimate, \hat{x} , of the state, x . This estimate is to be optimal in the sense that $E\{(x - \hat{x})'(x - \hat{x})\}$ is minimized. The solution to this problem is given by Kalman filter theory. Kalman filters have the structure of a state observer. They receive as inputs the plant input, u , and plant output, y , and produce as an output the state estimate vector, \hat{x} .

The second sub-problem involves using the state estimate from the Kalman filter as if it were an exact measurement of the states. As in last chapter, we solve the resulting deterministic linear quadratic control problem. The state estimates are fed through the resulting state feedback matrix, thus producing the control for the complete system. The structure of the total LQG compensator is a Kalman filter in series with a state feedback matrix [12].

A consistent, but more suave term for the LQG problem is the H_2 problem. This nomenclature arises because solving the LQG problem is analogous to the minimization of the H_2 norm of the transfer function from exogenous inputs to the error vector. Section 6.1 develops the H_2 theory in this fashion, following the work of Reference [17]. This approach is used over the traditional presentation of the LQG problem because it utilizes the two block format

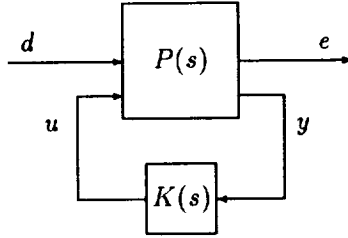


Figure 6.1. Plant With Compensator

we used in previous Chapters. Aside from visualizing the problem in a simpler manner, this approach helps motivate the H_∞ problem in the culminating Chapter. The H_∞ ¹ problem can be developed parallel to this approach.

Section 6.2 analyses the results of the H_2 design using the same criteria as before. The singular values from disturbance to control effort and disturbance to the end effector states are examined and compared to the open-loop system. A time domain simulation of the same jet firing pattern used before is also presented. Finally, stability robustness of the closed-loop H_2 system is examined including the parametric uncertainty.

6.1 H_2 Theory

Recall the general block diagram of the plant, but with the Δ block removed, as shown in Figure 6.1. This is the plant with compensator where u and y are the control inputs and observation vector respectively. d represents all exogenous inputs to the system. d includes process and sensor noise for the H_2 problem. e is the vector of signals whose mean squared value we wish to minimize. As before we chose it to contain the control effort and end effector states.

$$e = \begin{bmatrix} y \\ u \end{bmatrix}$$

¹ H_2 and H_∞ are both Hardy spaces

$P(s)$ is derived from the nominal plant model. Suppose that $P(s)$ is partitioned as follows:

$$\begin{bmatrix} e \\ y \end{bmatrix} = \begin{bmatrix} P_{11}(s)_{p_1 \times m_1} & P_{12}(s)_{p_1 \times m_2} \\ P_{21}(s)_{p_2 \times m_1} & P_{22}(s)_{p_2 \times m_2} \end{bmatrix} \begin{bmatrix} d \\ u \end{bmatrix} \quad (6.1)$$

We can eliminate u and y using $u = Ky$, to obtain

$$e = [P_{11} + P_{12}K(I - P_{22}K)^{-1}P_{21}] d \quad (6.2)$$

It is convenient to adopt the shorthand for the linear fractional transformation of P and K

$$\mathcal{F}_l(P, K) = P_{11} + P_{12}K(I - P_{22}K)^{-1}P_{21} \quad (6.3)$$

so that we can write

$$e = \mathcal{F}_l(P, K) d \quad (6.4)$$

A simple way to state the H_2 problem is to minimize $\|\mathcal{F}_l(P, K)\|_2$ for stabilizing K over all $\mathcal{F}_l(P, K) \in H_2$. The H_2 norm is defined in the frequency domain for a stable transfer function matrix, $G(s)$ as

$$\|G\|_2 \equiv \left(\frac{1}{2\pi} \int_{-\infty}^{\infty} \text{trace} [G(-j\omega)'G(j\omega)] d\omega \right)^{\frac{1}{2}} \quad (6.5)$$

Recall that the general state-space representation of Figure 6.1 is

$$\begin{bmatrix} \dot{x}_p \\ e \\ y \end{bmatrix} = \begin{bmatrix} A_p & B_1 & B_2 \\ C_1 & D_{11} & D_{12} \\ C_2 & D_{21} & D_{22} \end{bmatrix} \begin{bmatrix} x_p \\ d \\ u \end{bmatrix} \quad (6.6)$$

In order to insure stabilizing controllers exist, the uncompensated plant, (A_p, B_2, C_2) , as well as (A_p, B_1, C_1) must be stabilizable and detectable. The SSAD plant meets this condition and we must choose the error vector and its weights so that it too meets this condition. In order to ensure the realizability of resulting controllers we must also choose the weights on the error vector so that $\text{rank}(D_{12}) = m_2$ and $\text{rank}(D_{21}) = p_2$ where m_2 and p_2 are given in Equation 6.1.

Define the following transformation variables

$$\begin{aligned} z_1 &= (D_{12}'D_{12})^{-\frac{1}{2}} \\ z_2 &= (D_{21}D_{21}')^{-\frac{1}{2}} \end{aligned} \quad (6.7)$$

and apply them to the plant as follows

$$\begin{aligned}\tilde{B}_2 &= B_2 z_1 \\ \tilde{C}_2 &= z_2 C_2 \\ \tilde{D}_{12} &= D_{12} z_1 \\ \tilde{D}_{21} &= z_2 D_{21}\end{aligned}\tag{6.8}$$

Let us assume these transformations have already been applied, thus D_{12} and D_{21} have been normalized so that

$$D_{12} = [0 \ I]'' \quad \text{and} \quad D_{21} = [0 \ I]\tag{6.9}$$

The point of these transformations is that we can reduce the complexity of the controller formulas as long as we can write

$$D_{12}'' [C_1 \ D_{12}] = [0 \ I]\tag{6.10}$$

and

$$\begin{bmatrix} B_1 \\ D_{21} \end{bmatrix} D_{21}'' = \begin{bmatrix} 0 \\ I \end{bmatrix}\tag{6.11}$$

Equation 6.10 means that the penalty on $e = C_1 x_p + D_{12} u$ includes a normalized, nonsingular penalty on u . In other words, the error vector includes the control inputs with an identity weighting matrix and there is no cross weighting between the states and the control.

Equation 6.11 is dual to Equation 6.10. This equation flows from assuming that the disturbance vector, d , includes both the process noise on the states and the sensor noise on the measurements. These noises are separate and the sensor noise weighting matrix is normalized and nonsingular.

The transformations in Equation 6.7 allow us to choose non-normalized weights for D_{12} and D_{21} and then scale the plant so that Equations 6.10 and 6.11 still hold.

Two additional assumptions made on the plant are that $D_{11} = 0$ and $D_{22} = 0$. We require the former for the H_2 cost to be finite; the latter simplifies the formulas. For SSAD $D_{22} = 0$ and we chose the error vector to not include the disturbance hence $D_{11} = 0$.

Thus the form of the system becomes

$$\begin{bmatrix} \dot{x}_p \\ e \\ y \end{bmatrix} = \begin{bmatrix} A_p & B_1 & B_2 \\ C_1 & 0 & D_{12} \\ C_2 & D_{21} & 0 \end{bmatrix} \begin{bmatrix} x_p \\ d \\ u \end{bmatrix} \quad (6.12)$$

with

$$D_{12} = [0 \ I]'' \quad \text{and} \quad D_{21} = [0 \ I]$$

Before proceeding, let us define some notation. Let A , Q , and R be real $n \times n$ matrices. Q and R are both symmetric. Define the Hamiltonian matrix, H , as

$$H := \begin{bmatrix} A & R \\ Q & -A'' \end{bmatrix} \quad (6.13)$$

The definitions of the symbols $\text{dom}(\text{Ric})$ and $\text{Ric}(H)$ are that if $H \in \text{dom}(\text{Ric})$ and $X = \text{Ric}(H)$ then

- (i) X is symmetric.
- (ii) X satisfies the algebraic Riccati equation

$$A''X + XA + XRX - Q = 0$$

- (iii) $A + RX$ is stable.

In order to find an admissible controller K which minimizes $\|\mathcal{F}_\ell(P, K)\|_2$, we must solve the following two Riccati equations given by their Hamiltonian matrices

$$X_2 = \text{Ric} \begin{bmatrix} A_p & -B_2 B_2'' \\ -C_1'' C_1 & -A_p'' \end{bmatrix} \quad (6.14)$$

$$Y_2 = \text{Ric} \begin{bmatrix} A_p'' & -C_2'' C_2 \\ -B_1 B_1'' & -A_p \end{bmatrix} \quad (6.15)$$

The two solutions, X_2 and Y_2 , are positive semidefinite. Using these solutions, define

$$F_2 = -B_2' X_2 \quad (6.16)$$

$$L_2 = -Y_2 C_2' \quad (6.17)$$

Notice that if the control weighting matrix is normalized to identity as we have done, F_2 is the optimal state feedback gain as solved for last in the Chapter with full state feedback. L_2 represents the solution to the Kalman filter gain matrix. Now we may write the unique optimal controller as

$$K(s) := \left[\begin{array}{c|c} \frac{A_p + B_2 F_2 + L_2 C_2}{F_2} & \frac{-L_2}{0} \end{array} \right] \quad (6.18)$$

Considering that our plant is square, (six inputs and six outputs), we have an invertible system A matrix, and that the non-minimum phase transmission zeros are fast relative to the rest of the system, it is tempting to apply a loop-shaping technique. The Linear Quadratic Gaussian/Loop Transfer Recovery (LQG/LTR) method presented in References [12] and [13] is a loop-shaping technique that allows us to shape the singular values at the input or output of the plant.

Unfortunately, in the LQG/LTR methodology, the ways in which the process noise and sensor noise enter the plant are treated as tuning parameters rather than as representations of the real plant behavior. In terms of Equation 6.6, B_1 and D_{21} become design parameters which are adjusted along with the weights on the states and the controls to shape the singular values. For SSAD the process noise, Shuttle jet firings, does enter the system in a prescribed manner. LQG/LTR can still be applied on SSAD, only it is not possible to directly shape the singular values of interest. After initial attempts at applying LQG/LTR it became apparent that conventional H_2 allows a more direct approach the problem since B_1 and D_{21} are physical parameters.

6.2 H_2 Results

In the H_2 problem, the design parameters are the choice of weights on the contents of the error vector, y and u . In SSAD, since y corresponds to the end effector states, we can choose the C_1 weights as we selected Q when designing a LQR. We multiply each channel corresponding to an attitude by an order of magnitude to account for the difference between position and attitude singular values in the open-loop system. In this manner a one inch error is not treated as serious as a one radian error by the H_2 controller. This choice is only an initial guess and can be modified to bring the closed-loop system within performance objectives.

The weights on the control effort, D_{12} , are initially placed at the inverse of the joint rate limits as in the LQR design. Again, this design parameter is tuned until a satisfactory design is achieved. One thing to note, the final weights of the H_2 design do not have to correspond to the final weights of the LQR design. Recall the differences between the two design plants; LQR assumes full state feedback uncorrupted by noise while the H_2 compensator has only the observation vector which is also corrupted by sensor noise.

Section 6.2.1 examines the control effort and performance singular values of the H_2 design. A time domain simulation driven by the same jet firing pattern as used on the LQR is included as well to help interpret the singular values. Section 6.2.2 examines the stability robustness of the H_2 design.

6.2.1 H_2 Control Effort and Performance

Figure 6.2 shows the singular values from disturbance to each individual control effort channel after tuning the weights on the error vector. As before, each control weight is fine tuned until the scaled singular value falls just below one. Notice that two of the control effort singular values actually lie below one. These are the singular values corresponding to elbow pitch and wrist pitch joints.

During the design process, if a particular control effort singular value fell below one, the corresponding weight was reduced allowing the compensator to use more control in that channel. Conversely, if a control effort singular value fell above one, the corresponding penalty was increased. For the elbow pitch and wrist pitch joint rates, the penalties were successively reduced up until the weighting matrix, D_{12} started to numerically fail the rank tests. Nevertheless, the

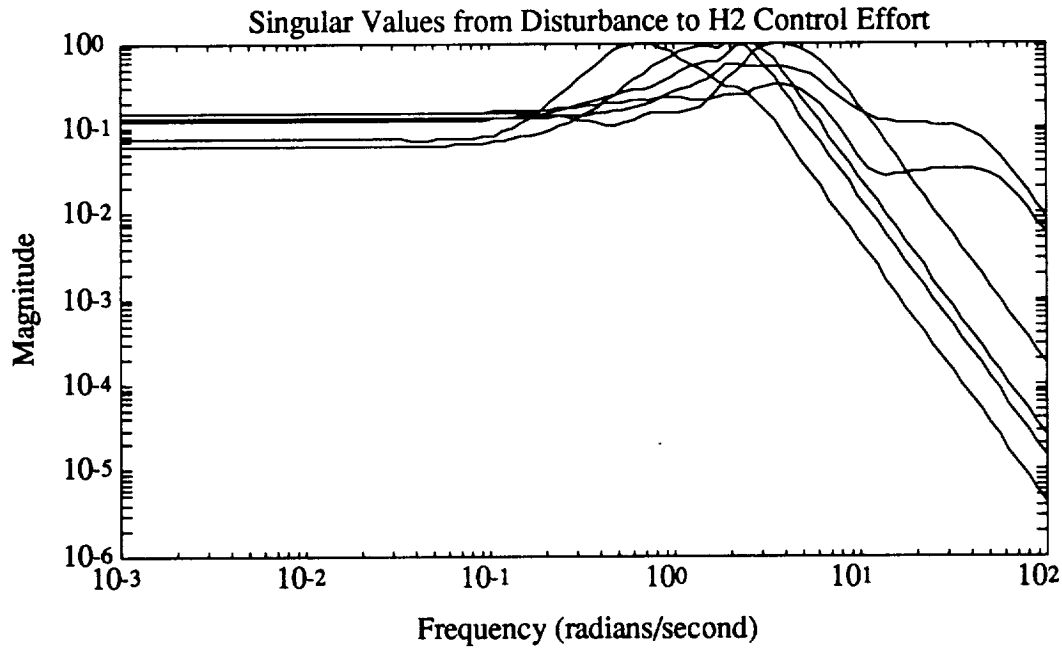


Figure 6.2. Control Effort Singular Values of the H_2 System

compensator chose not to use more control in these channels.

There are two explanations for this result. First, the elbow pitch and wrist pitch joint rates may have limited ability to affect the performance objectives. Consider the simple example of a body with horizontal and vertical velocity as its controls. If we choose as performance objectives vertical position only, a controller would have no reason to use the horizontal control channel. This seems unlikely for SSAD since clearly from Figure 6.2 it is using some control in these channels. If the penalty is made less on these channels, it should use more control even if the benefit is slight. A more likely explanation is that use of the elbow pitch and wrist pitch joint rates is penalized through some coupling in the system. Use of elbow pitch may, for instance, reduce the error in the X direction but cause large excursions in Y which would require use of shoulder pitch to compensate. Thus the weight on shoulder pitch indirectly penalizes elbow pitch as well.

Figure 6.3 presents the singular values from disturbance to end effector position and attitude. Included on the same plots is the corresponding information for the open-loop system. For the H_2 design we are barely able to meet the performance goal of less than 1 inch excursion in position. We are able to meet the attitude goal of less than 0.01 radians of rotation excursion

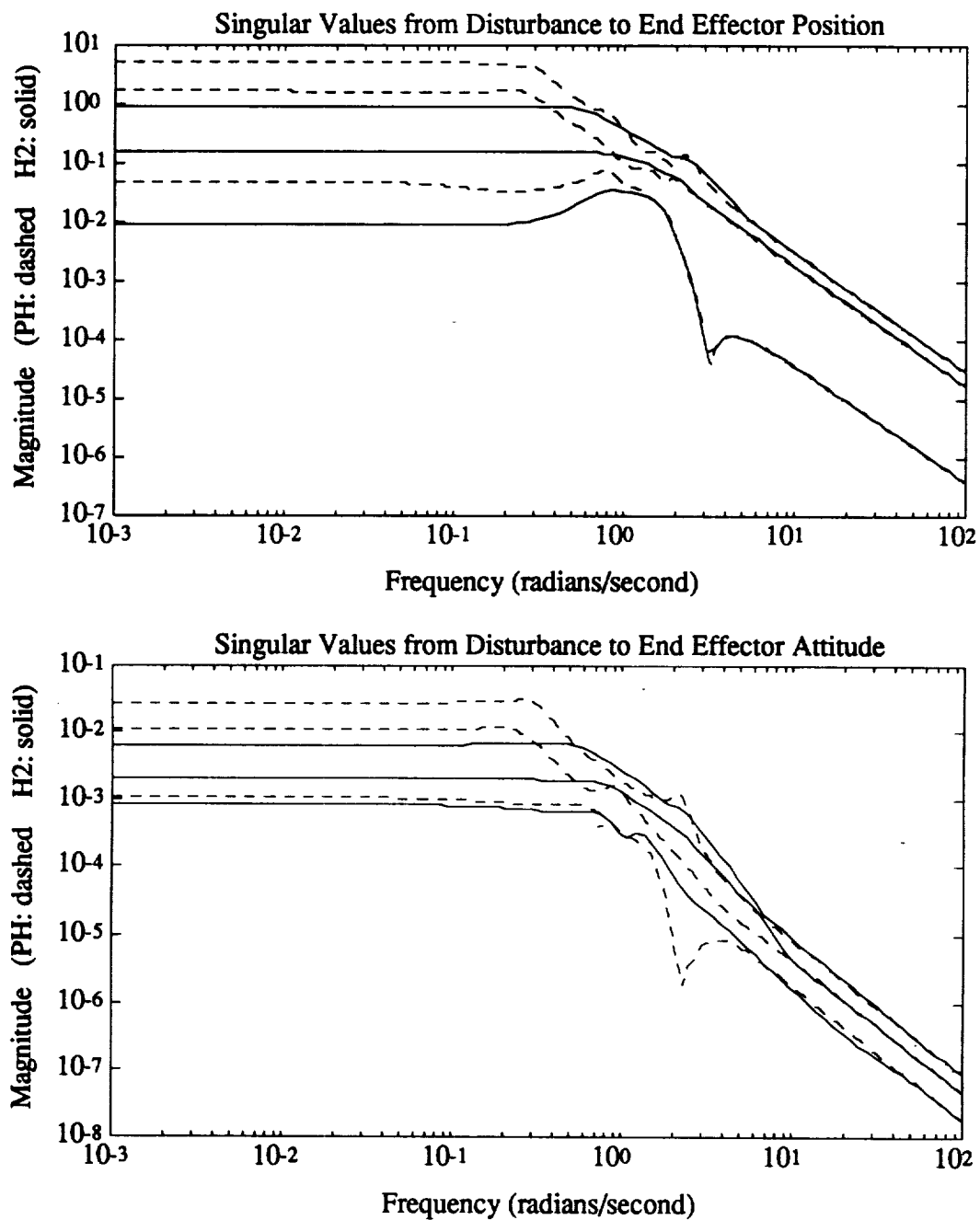


Figure 6.3. Performance Singular Values of the H_2 System

without problem. Both goals are met without exceeding the joint rate limits.

As with the LQR design, to help visualize what is occurring on the singular value plots, a time domain simulation is presented in Figures 6.4 and 6.5. These Figures include both the response of the open-loop system and the H_2 system. As before, a roll command is given for a full 10 seconds immediately followed by a 10 second pitch command and finally a 10 second yaw command.

From Figure 6.4 we can see that as in the LQR design, the X direction has considerably poorer disturbance rejection than the Y and Z directions for the H_2 compensator. Similar improvement over the uncompensated system as in the LQR design is also apparent. For the attitude directions, roll disturbance rejection is considerably better than the other axes as shown in Figure 6.5. Overall, the resulting H_2 design performance is only slightly below the full state feedback LQR design.

6.2.2 H_2 Stability Robustness

Applying both the small gain test and μ -analysis to the closed-loop H_2 system results in Figure 6.6. As before, the system fails both stability robustness tests. With the LQR plant, we evaluated the eigenvalues of the closed-loop system for four sets of the parameters and showed that the system was stable for these endpoints. Though this is not conclusive proof, it suggests that it is possible that the LQR closed-loop system is indeed robustly stable.

Evaluating those same sets of parameters for the closed-loop H_2 design does show conclusively that the system is robustly unstable. Figure 6.7 shows the near pole locations for the nominal closed-loop H_2 system. The following four Figures show the closed-loop poles for the four sets of perturbed parameters. Figure 6.8 places both the K_{MA} and the K_G at their minimum values. Figure 6.9 places both sets of parameters at their maximum values. Figure 6.10 places the K_{MA} at their minimum values and the K_G at their maximum values. Finally, Figure 6.11 considers the last permutation of the K_{MA} at their maximum values and the K_G at their minimum values.

Aside from the nominal plant, the closed-loop system is only stable for Figure 6.9. In Chapter 4 when considering the open-loop plant, we were able to isolate the stability problem to when the system is operating at very low amplitudes. In this region, K_{MA} is at its maximum and K_G is near its minimum. For the H_2 system we cannot draw the same conclusions. Stability

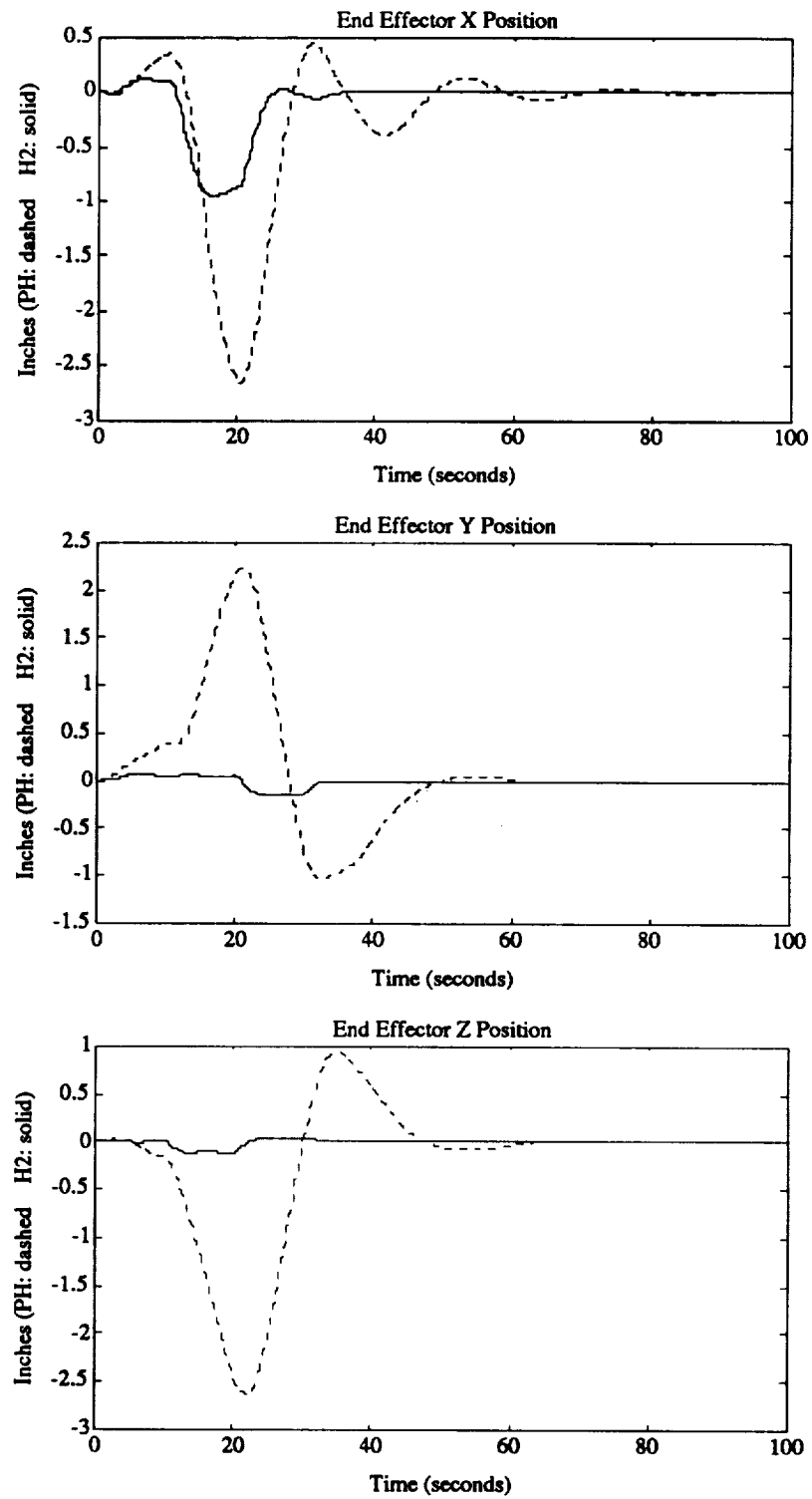


Figure 6.4. Translational Response of PH System and H_2 System to Attitude Thruster Commands

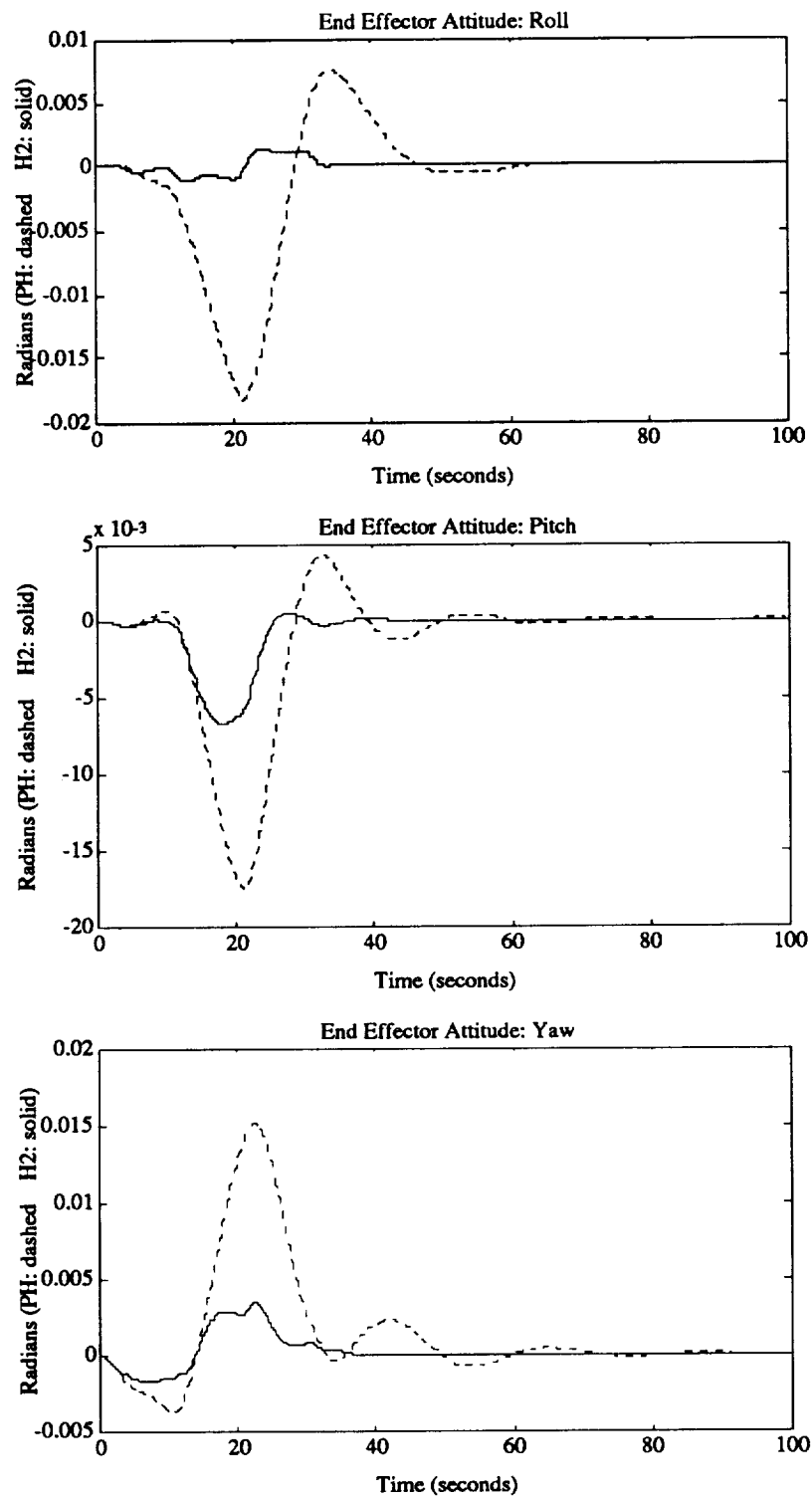


Figure 6.5. Rotational Response of PH System and H_2 System to Attitude Thruster Commands

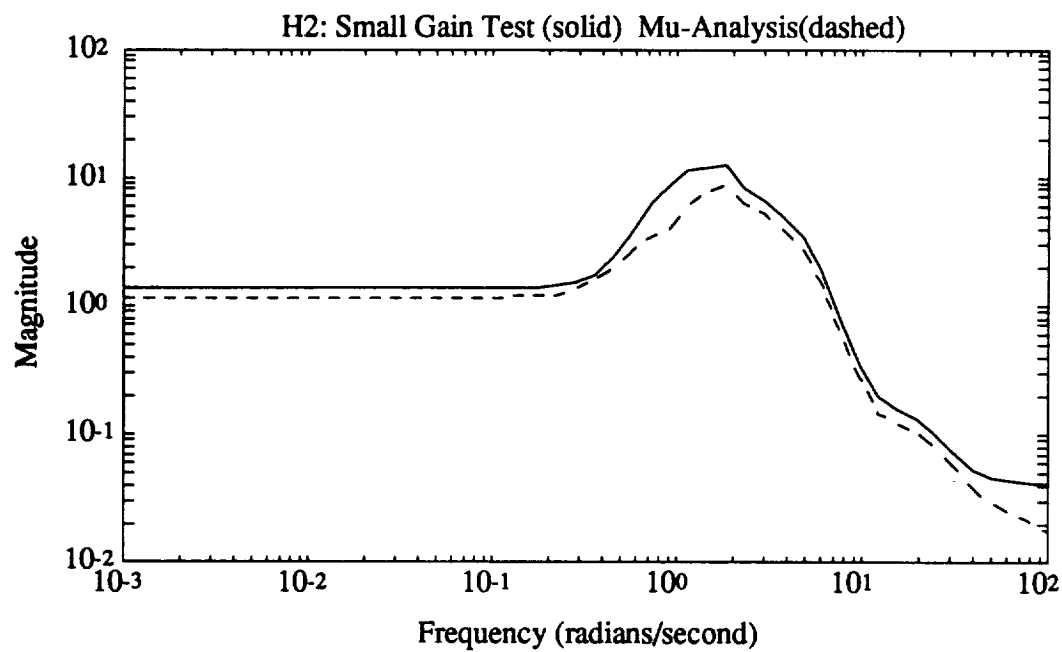


Figure 6.6. Robust Stability Analysis of the H_2 System

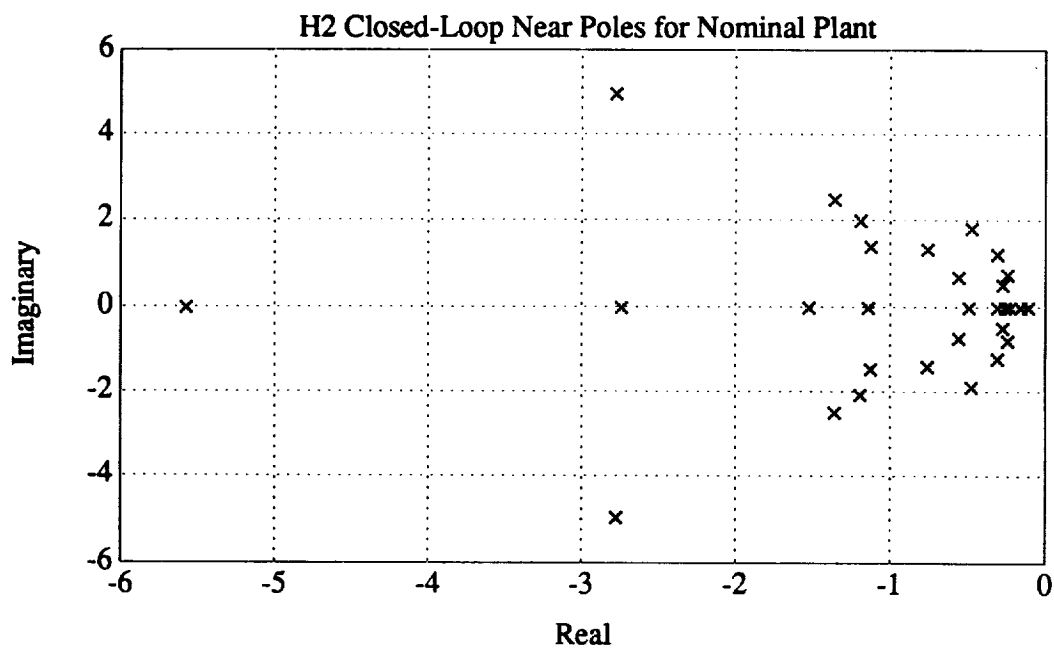


Figure 6.7. Closed-Loop Poles of the Nominal H_2 System

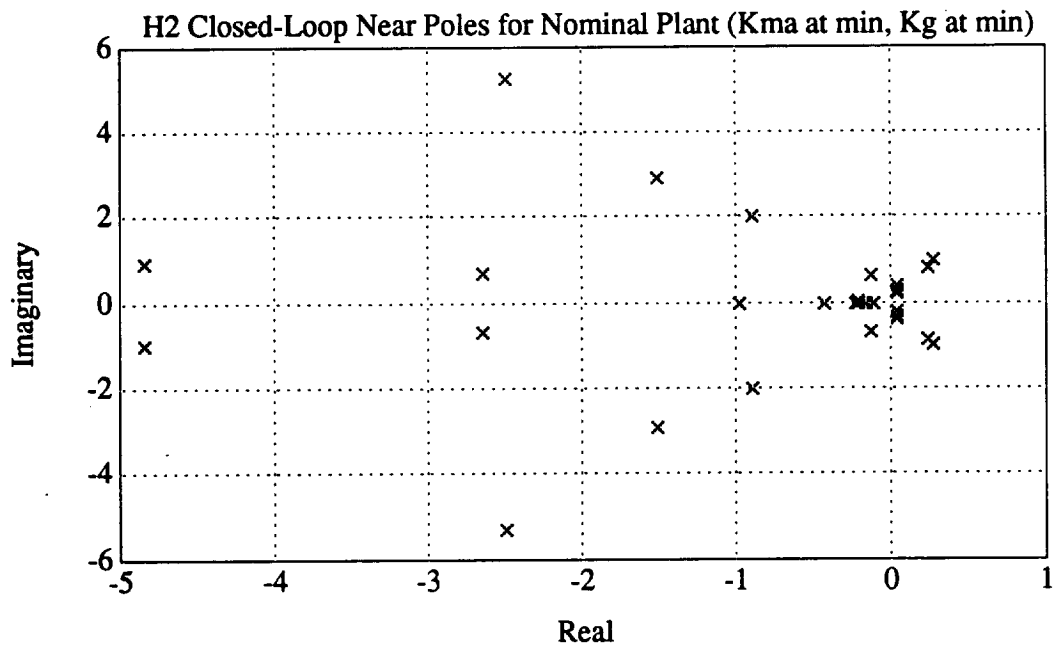


Figure 6.8. Closed-Loop Poles of the Off-Nominal H_2 System: 1

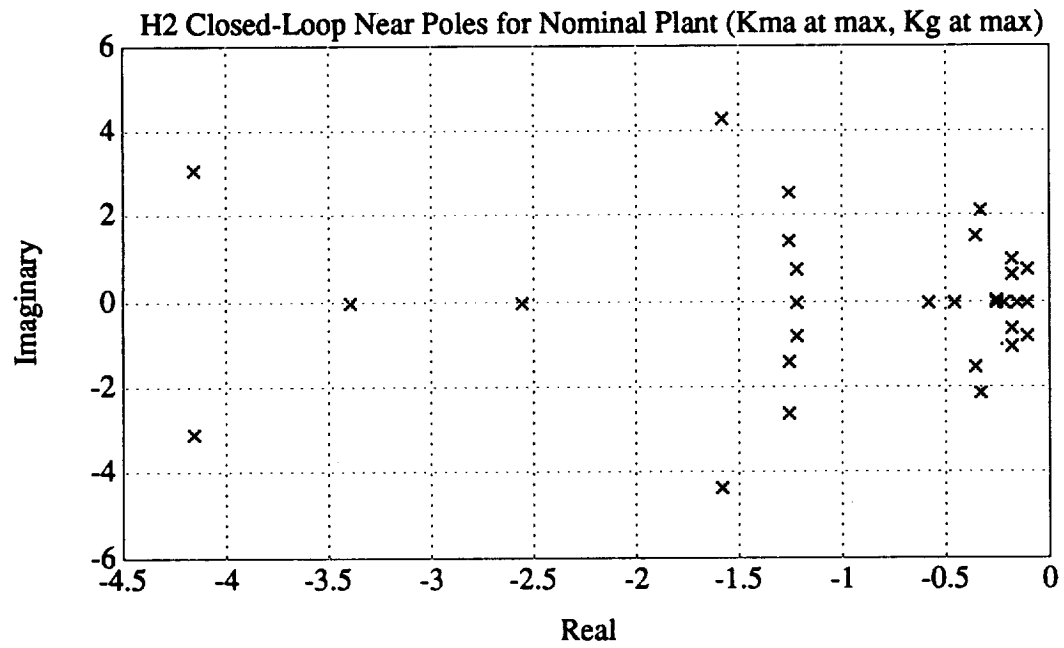


Figure 6.9. Closed-Loop Poles of the Off-Nominal H_2 System: 2

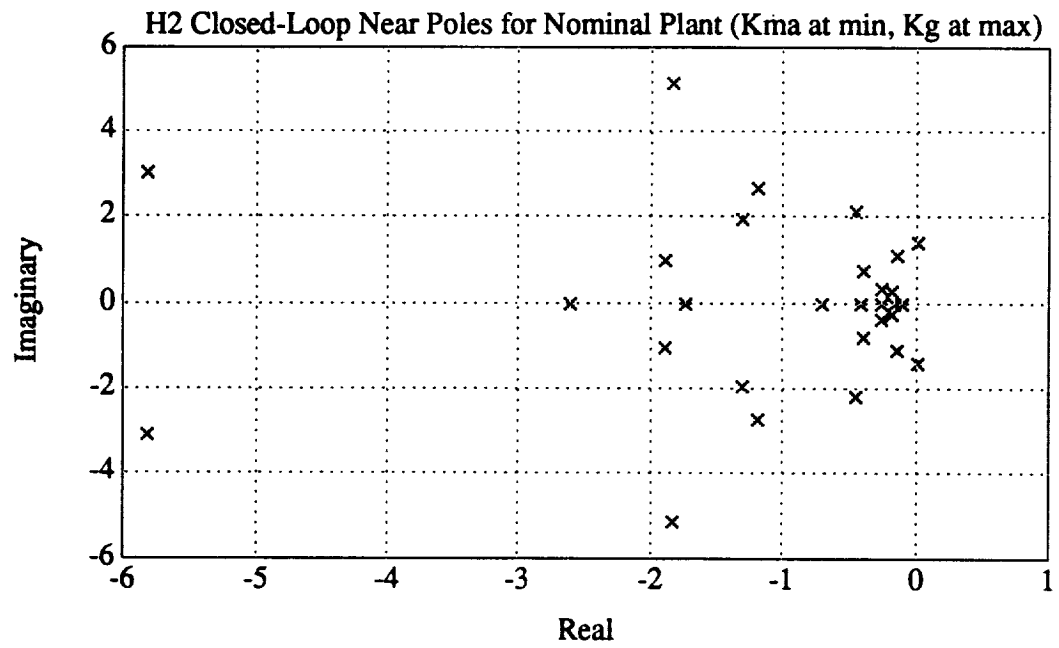


Figure 6.10. Closed-Loop Poles of the Off-Nominal H_2 System: 3

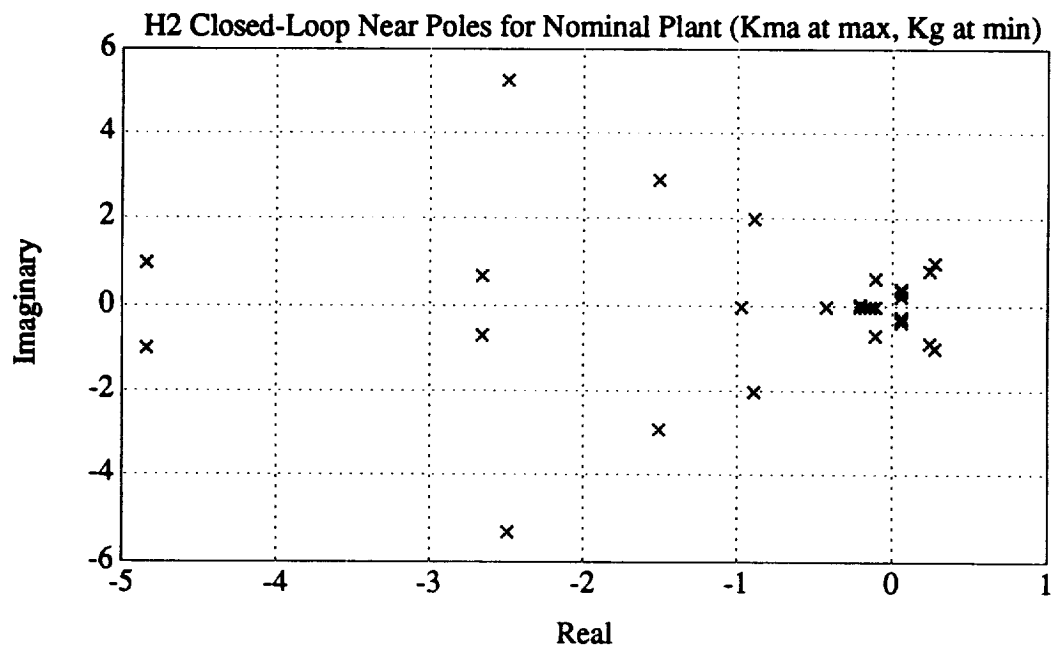


Figure 6.11. Closed-Loop Poles of the Off-Nominal H_2 System: 4

is a problem for the closed-loop system in several configurations. If the stability problem was caused by neglected dynamics, a solution to robust stability would be to reduce the bandwidth of the system. This could be accomplished by either further penalizing the control effort or reducing the weights on the end effector states, ie., demand less performance. Unfortunately, with parametric uncertainty the low frequency system poles simply aren't where the controller is expecting them. Reducing the bandwidth will not solve our problem. We will explore this issue in further detail when considering the H_∞ design.

6.3 Summary

This Chapter removes the requirement for full state feedback uncorrupted by noise and presents the H_2 (or LQG) approach. This approach involves designing a Kalman filter to estimate all of the system states from the observation and control vector and then using these estimates as perfect state information fed into a LQR.

On the nominal plant, the H_2 approach is able to recover performance comparable to the LQR design. Both performance objectives are met without exceeding the limits on the control effort. Unfortunately, the closed-loop H_2 system is not robustly stable in face of the parametric uncertainty present in the plant as indicated by both μ -analysis and the small gain test. Though these tests are both conservative for real parametric uncertainty, eigenvalue analysis shows conclusively that the system is not robustly stable.

Chapter 7

H_∞ Design

In the last Chapter we designed a compensator that meets performance specifications within allowable control effort specifications by minimizing the H_2 norm of the transfer function from exogenous inputs to the error vector. This Chapter solves a similar problem, only this time performance is measured with an H_∞ norm. The H_∞ norm is defined in the frequency domain for a stable transfer function matrix as

$$\begin{aligned}\|G(s)\|_\infty &\equiv \sup_{\omega} \bar{\sigma}[G(j\omega)] \\ &= \sup_{\|u\|_2 \neq 0} \frac{\|y\|_2}{\|u\|_2}\end{aligned}\tag{7.1}$$

Using this norm, an H_∞ optimization design technique will result in the compensator that minimizes the supremum over all frequencies of the maximum singular value of the transfer function of interest.

Recall that the disturbances acting on the SRMS are caused by Shuttle attitude thruster firings. The Shuttle may fire its thrusters in pulses every 80 milliseconds, or for steps lasting as long as 200 seconds. Such a firing profile has the ability to excite the system at any frequency up through its bandwidth. This makes the H_∞ norm a natural selection for optimization. We would like to reduce the worst case gain for disturbances of the SRMS at all frequencies.

There are many parallels between the H_2 and H_∞ approaches. Development of the H_∞ theory in Section 7.1 flows naturally from the work of last Chapter. As in the H_2 case, we arrive at two algebraic Riccati equations. The H_∞ Riccati equations can be thought of as those that arise from a linear quadratic differential game between two opposing players. One player chooses the disturbance to maximize the norm of the output while the opposing player

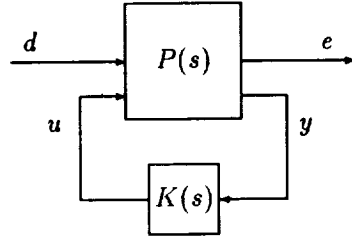


Figure 7.1. Plant With Compensator

chooses the control input to minimize it. The work in this Section follows that of Reference [17]. Though not presented, the H_∞ design technique can also be derived by recasting the system as a model-matching problem via the parametrization of all stabilizing controllers. An exposition of this technique is presented in Reference [18].

Section 7.2 analyzes the results of the H_∞ design using the same criteria as in previous Chapters. The singular values from disturbance to control effort and disturbance to the end effector states are examined and compared to the open-loop system. To highlight the differences in optimizing the H_2 norm versus the H_∞ norm, a comparison of these two designs is presented as well. As before, a time domain simulation of the same jet firing pattern is presented. Finally, stability robustness of the closed-loop H_∞ system is examined in face of the parametric uncertainty. By choosing a different transfer function to optimize, namely the output of the plant uncertainties to the input of the plant uncertainties, we can determine if any H_∞ controller would be able to robustly stabilize the plant.

7.1 H_∞ Theory

For the H_∞ design we will use the same general two-block diagram as shown in Figure 7.1. Define the error vector the same as for the H_2 design, namely

$$e = \begin{bmatrix} y \\ u \end{bmatrix}$$

Using the same notation as in the last Chapter, write the transfer function from the exogenous inputs to the error vector as

$$e = \mathcal{F}_\ell(P, K) d \quad (7.2)$$

The H_∞ optimal compensator is the compensator that minimizes the supremum over all frequencies of the maximum singular value of $\mathcal{F}_\ell(P, K)$ for stabilizing K . This can be written as

$$\min_{\text{stabilizing } K} \|\mathcal{F}_\ell(P, K)\|_\infty = \min_{\text{stabilizing } K} \sup_{\omega} \bar{\sigma}(\mathcal{F}_\ell(P, K)(j\omega)) \quad (7.3)$$

In practice however, contrary to the H_2 problem, H_∞ optimal controllers are more difficult to characterize than suboptimal ones. We settle for an admissible K such that $\|\mathcal{F}_\ell(P, K)\|_\infty < \gamma$.

Before characterizing the H_∞ suboptimal controllers, consider the transfer function matrix of Figure 7.1 to be in the same form as the H_2 problem. That is

$$\begin{bmatrix} \dot{x}_p \\ e \\ y \end{bmatrix} = \begin{bmatrix} A_p & B_1 & B_2 \\ C_1 & 0 & D_{12} \\ C_2 & D_{21} & 0 \end{bmatrix} \begin{bmatrix} x_p \\ d \\ u \end{bmatrix} \quad (7.4)$$

with

$$D_{12} = [0 \ I]'' \quad \text{and} \quad D_{21} = [0 \ I]$$

H_∞ theory requires that the following must hold true for the system:

(a) (A, B_1, C_1) is stabilizable and detectable.

(b) (A, B_2, C_2) is stabilizable and detectable.

(c) $D_{12}'' [C_1 \ D_{12}] = [0 \ I]$.

(d) $\begin{bmatrix} B_1 \\ D_{21} \end{bmatrix} D_{21}'' = \begin{bmatrix} 0 \\ I \end{bmatrix}$.

The weights on the states in the error vector, e , must be chosen to insure (a) is met. As shown in Chapter 4, (b) is known to be true for SSAD. To meet conditions (c) and (d) it will be necessary to apply the same transformations on the system used in the H_2 problem as shown in Section 6.1. Implicit in the given state-space realization for Figure 7.1 is that $D_{11} = 0$ and $D_{22} = 0$. In a general H_∞ problem these conditions can be relaxed, though it would

complicate the formulas presented here considerably. A treatment of the more general problem can be found in Reference [19].

The H_∞ suboptimal problem is to find an admissible K such that $\|\mathcal{F}_t(P, K)\|_\infty < \gamma$. Its solution involves two Hamiltonian matrices as in the H_2 problem

$$F_\infty = \begin{bmatrix} A_p & \gamma^{-2} B_1 B_1' - B_2 B_2' \\ -C_1' C_1 & -A_p' \end{bmatrix} \quad (7.5)$$

$$J_\infty = \begin{bmatrix} A_p' & \gamma^{-2} C_1' C_1 - C_2' C_2 \\ -B_1 B_1' & -A_p \end{bmatrix} \quad (7.6)$$

These Hamiltonians are remarkably similar to the H_2 formulation. The main difference is that the additional terms in the upper-right entry of both F_∞ and J_∞ make the two Hamiltonians no longer sign definite. Therefore we cannot guarantee that either F_∞ or J_∞ has a Riccati solution or that the solution is positive definite. In fact, this limitation is related to the existence of a H_∞ suboptimal controller.

In Reference [17], Doyle et al prove that there exists an admissible controller, K , such that $\|\mathcal{F}_t(P, K)\|_\infty < \gamma$ iff the following conditions hold true

- (i) $F_\infty \in \text{dom}(\text{Ric})$ and $X_\infty := \text{Ric}(F_\infty) \geq 0$.
- (ii) $J_\infty \in \text{dom}(\text{Ric})$ and $Y_\infty := \text{Ric}(J_\infty) \geq 0$.
- (iii) $\rho(X_\infty Y_\infty) < \gamma^2$ where $\rho(M)$ is the spectral radius of M .

When all three of these conditions hold, one such suboptimal controller is

$$K_{sub}(s) := \left[\begin{array}{c|c} A_\infty & B_\infty \\ \hline C_\infty & 0 \end{array} \right] \quad (7.7)$$

where

$$\begin{aligned} A_\infty &= A_p + \gamma^{-2} B_1 B_1' X_\infty + B_2 C_\infty - B_\infty C_2 \\ B_\infty &= (I - \gamma^{-2} Y_\infty X_\infty)^{-1} Y_\infty C_2' \\ C_\infty &= -B_2' X_\infty \end{aligned} \quad (7.8)$$

Conditions (i) through (iii) suggest the following method, known as γ iteration, to calculate an H_∞ ‘optimal’ controller: select a positive number γ ; test conditions (i) through (iii); increase γ if failed or decrease γ if passed; repeat until within a desired tolerance.

To illustrate the relationship between the H_∞ and H_2 solutions, notice that as $\gamma \rightarrow \infty$, $X_\infty \rightarrow X_2$, etc., and $K_\infty \rightarrow K_2$. This can be seen directly from the two sets of Hamiltonians in the H_∞ and H_2 problem formulations; as $\gamma \rightarrow \infty$ the H_∞ Hamiltonians become the H_2 Hamiltonians.

7.2 H_∞ Results

As in the H_2 problem, the design parameters of the H_∞ problem are the choice of weights on the contents of the error vector, namely y and u . In design, select the C_1 weights for the H_∞ problem as before when designing both the H_2 and LQR controllers. That is, multiply each channel corresponding to an attitude by an order of magnitude to account for the difference between position and attitude singular values of the open-loop system. This is to ameliorate the difference between a one inch error and a one radian error.

The weights on the control effort, D_{12} , are treated as the main tuning parameter. The weight on each control channel is increased or decreased appropriately until every control effort singular value does not exceed the corresponding joint rate limit. The final weights of the H_∞ design need not correspond to the weights of the H_2 design since a different norm is being optimized.

Section 7.2.1 examines the control effort and performance singular values of the H_∞ design. The performance singular values are compared not only to the open-loop plant but also to the H_2 design in order to highlight the differences in the two design techniques. A time domain simulation driven by the same jet firing pattern used on the other designs is included as well to help interpret the singular values. Section 7.2.2 examines the stability robustness of the H_∞ design. By choosing a different transfer function’s H_∞ norm to minimize, we can determine if it is possible to design a robustly stable compensator.

7.2.1 H_∞ Control Effort and Performance

Figure 7.2 shows the singular values from disturbance to control effort after tuning the

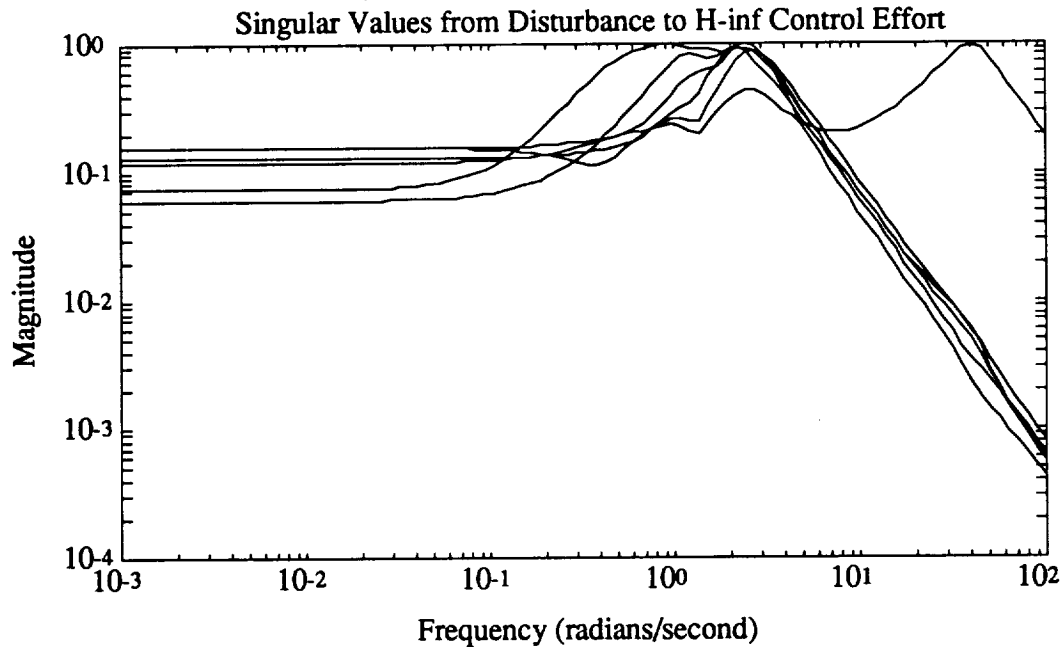


Figure 7.2. Control Effort Singular Values of the H_∞ System

weights on the error vector. As before, each control channel weight residing in D_{12} is fine tuned until the scaled singular value falls just below one.

In the H_2 solution, the controller did not make full use of every control channel, specifically elbow pitch and wrist pitch. For the H_∞ design a different norm is designed for, the H_∞ norm, that is the supremum over all frequencies of the maximum singular value, not the area under the singular value curves as in the H_2 case. The H_∞ controller is able to make use of each control to its full potential since it is penalizing the control channels in a different way.

Figure 7.3 presents the singular values from disturbance to end effector position and attitude. Included on the same plots is the corresponding information for the open-loop system. The H_∞ design is able to meet the performance goals of less than 1 inch excursion in position and less than 0.01 radians of rotation excursion without exceeding the joint rate limits.

Figure 7.4 compares the singular values from disturbance to end effector position and attitude for both the H_∞ and H_2 systems. Because the H_∞ design is trying to minimize the H_∞ norm, it has sacrificed some performance at 2 rps so that the maximum singular value can be brought down. The difference between the two designs is not as dramatic as can be seen in other systems since the H_2 design does not contain any large resonances, or 'hills,' in its

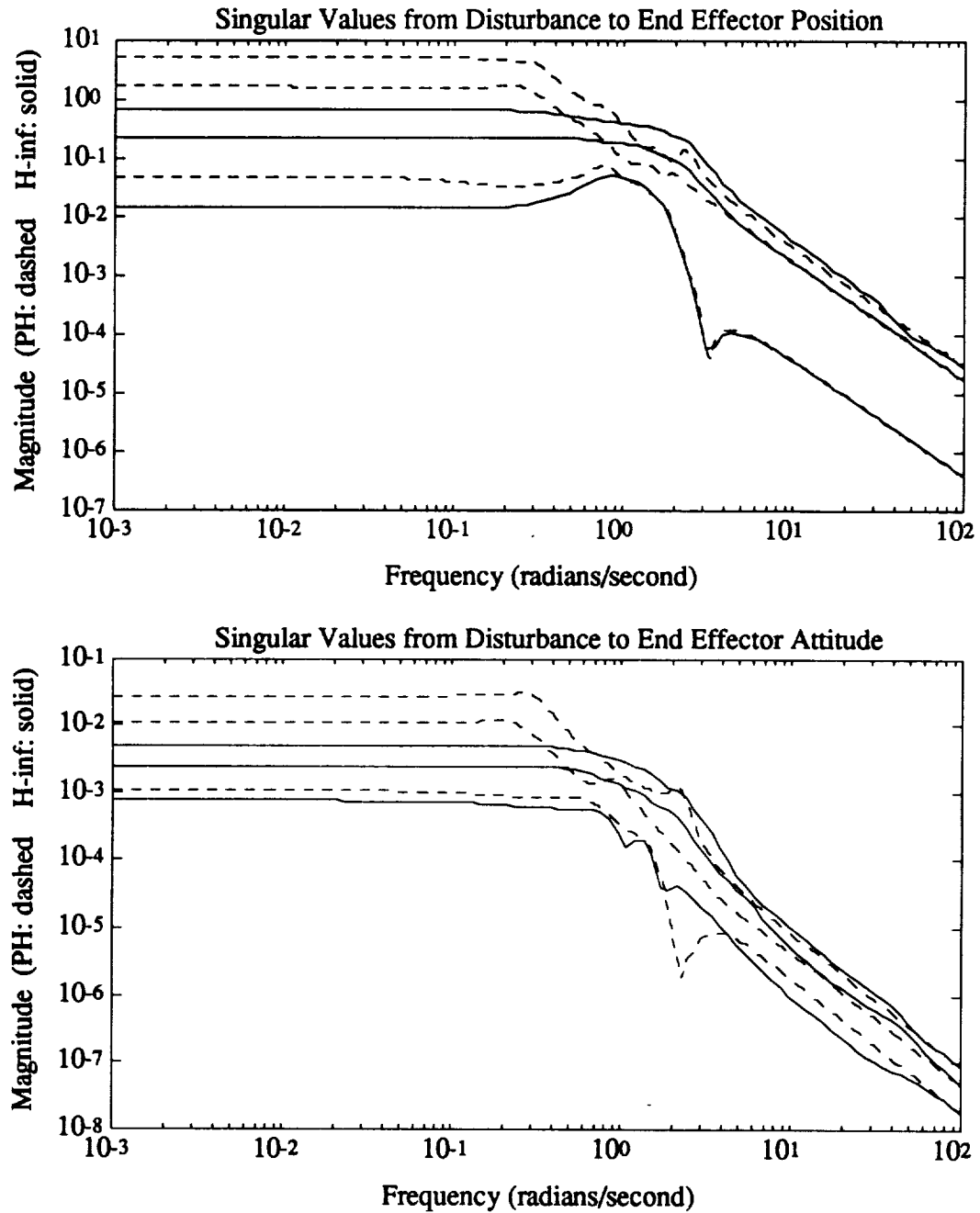


Figure 7.3. Performance Singular Values of the H_∞ and Position Hold Systems

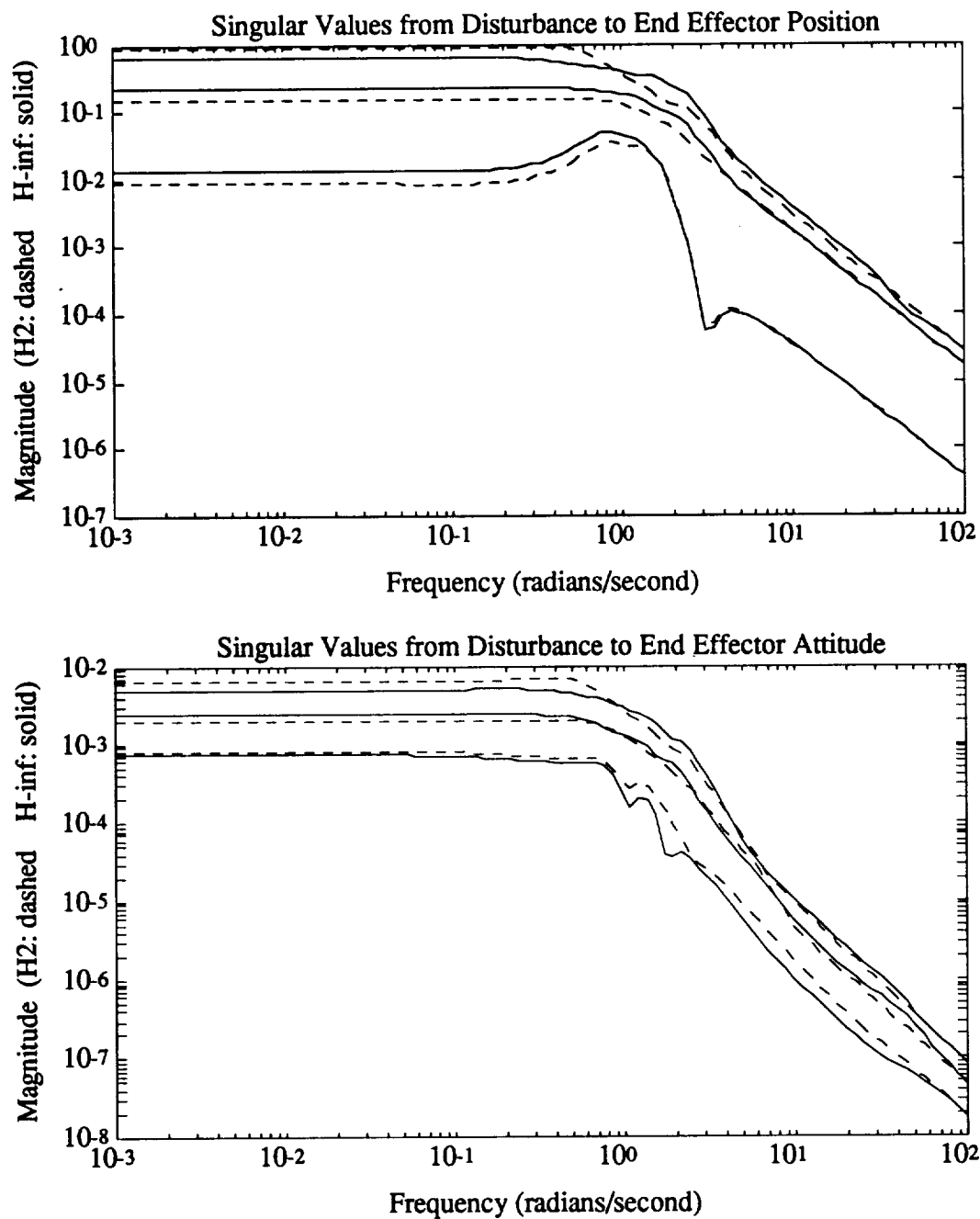


Figure 7.4. Performance Singular Values of the H_∞ and H_2 Systems

maximum singular value to begin with, it is already flat. The H_∞ design lowers the maximum singular value for both position and attitude at the expense of some of the other directions.

The presence of the control effort in the error vector acts like an H_2 constraint on the H_∞ design limiting the bandwidth of the closed-loop system. The H_∞ design sans control effort in the error vector would have a theoretically infinite bandwidth; theoretical because even if we accept exceeding the joint rate limits to increase the bandwidth, the actual system will run into physical constraints on the control effort.

As with the previous designs, Figures 7.5 and 7.6 present a time domain simulation. As before, a roll command is given for a full 10 seconds immediately followed by a 10 second pitch command and finally a 10 second yaw command. These Figures include the responses of the H_∞ system as well as both the open-loop and the H_2 system.

From Figure 7.5 it is apparent that as in the previous designs, the H_∞ compensator's X direction has poorer disturbance rejection than the Y and Z directions. For the attitude directions, roll disturbance rejection is better than the other axes as shown in Figure 7.6. Compared to the H_2 system, the H_∞ system is better in some directions and slightly worse in others. As expected, the worst case direction is better for the H_∞ design, namely X for the position directions and pitch for the attitude directions. These results confirm the singular value plots that show the H_∞ design offers a better worst case direction at the expense of some of the other directions. Nevertheless, both controllers are adequate to achieve our desired performance objectives.

7.2.2 H_∞ Stability Robustness

Figure 7.7 shows the results of applying both the small gain test and μ -analysis to the closed-loop H_∞ system. As with every other design, the H_∞ system fails both stability robustness tests. Experience with the other designs in previous Chapters show that these tests may be poor indicators of the system's true robust stability.

Eigenvalue analysis of both the open-loop system and the H_2 design show conclusively that these two systems are not robustly stable in face of the parametric uncertainty present in the model. However, for the LQR design the closed-loop system is stable for four sets of the parameters at their endpoints. Though this is not undisputable proof, it suggests that it is possible the LQR closed-loop system is indeed robustly stable. This is a crude method for

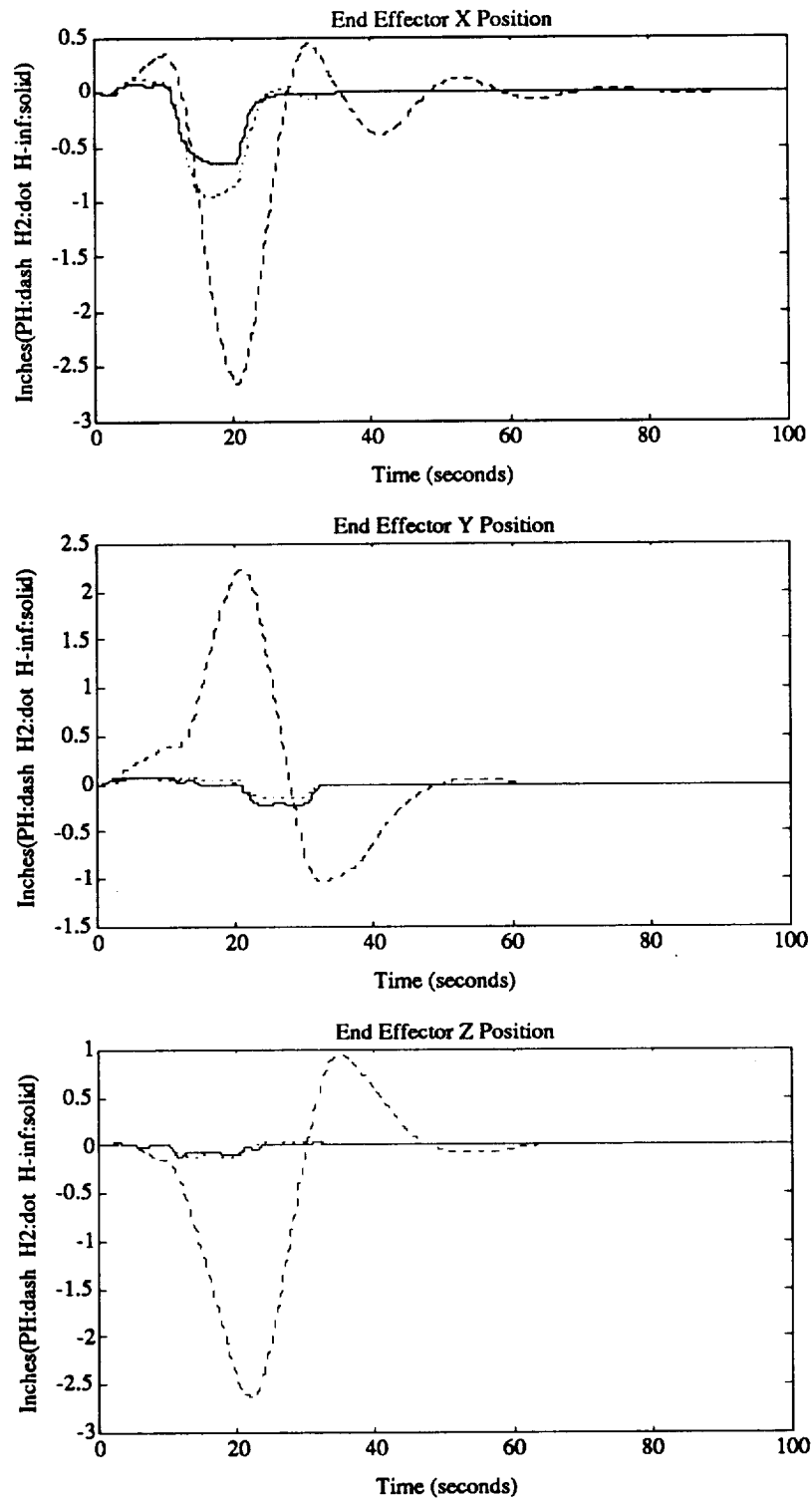


Figure 7.5. Translational Response of PH, H_2 , and H_∞ Systems to Attitude Thruster Commands

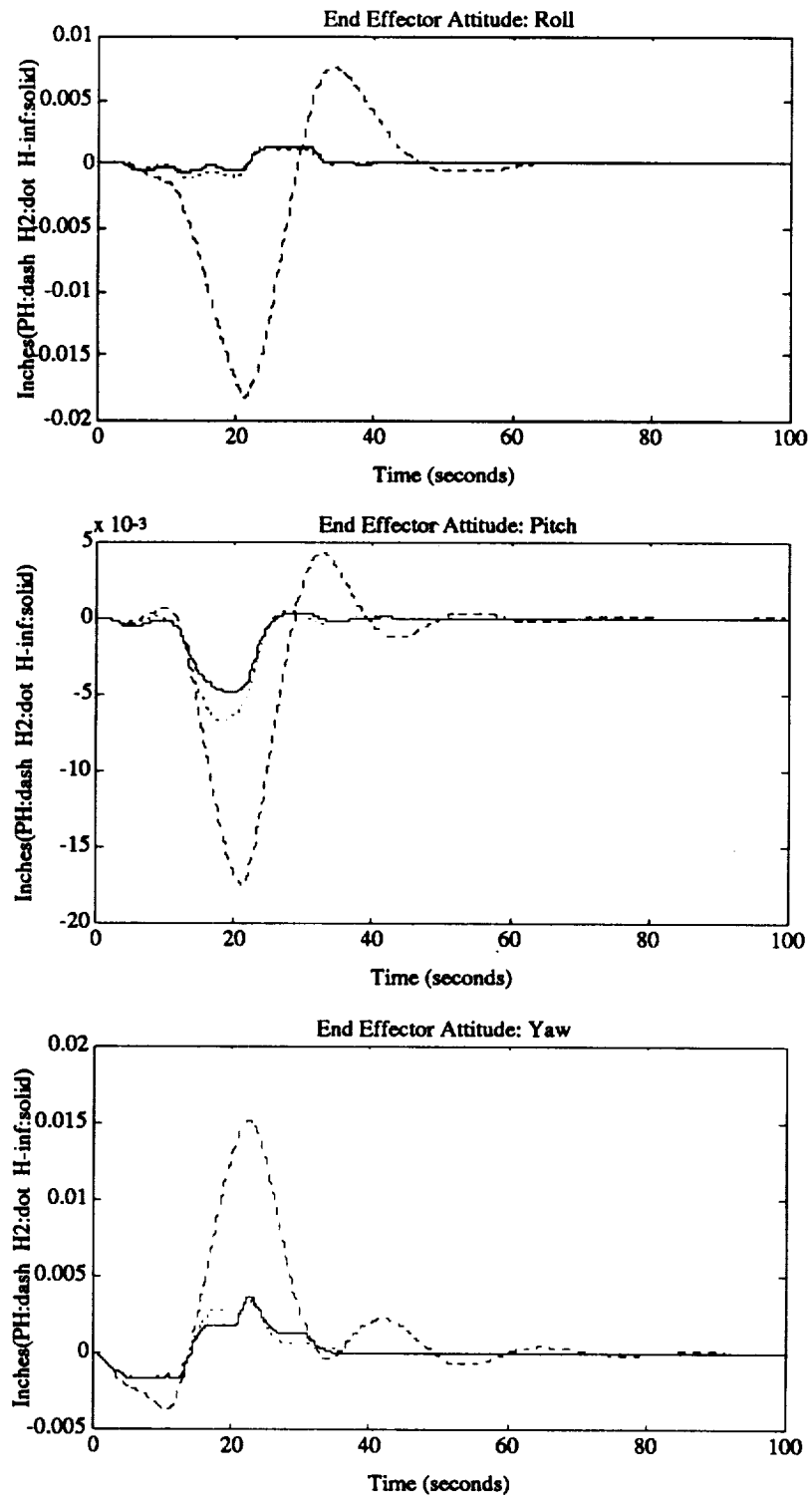


Figure 7.6. Rotational Response of PH, H_2 , and H_∞ Systems to Attitude Thruster Commands

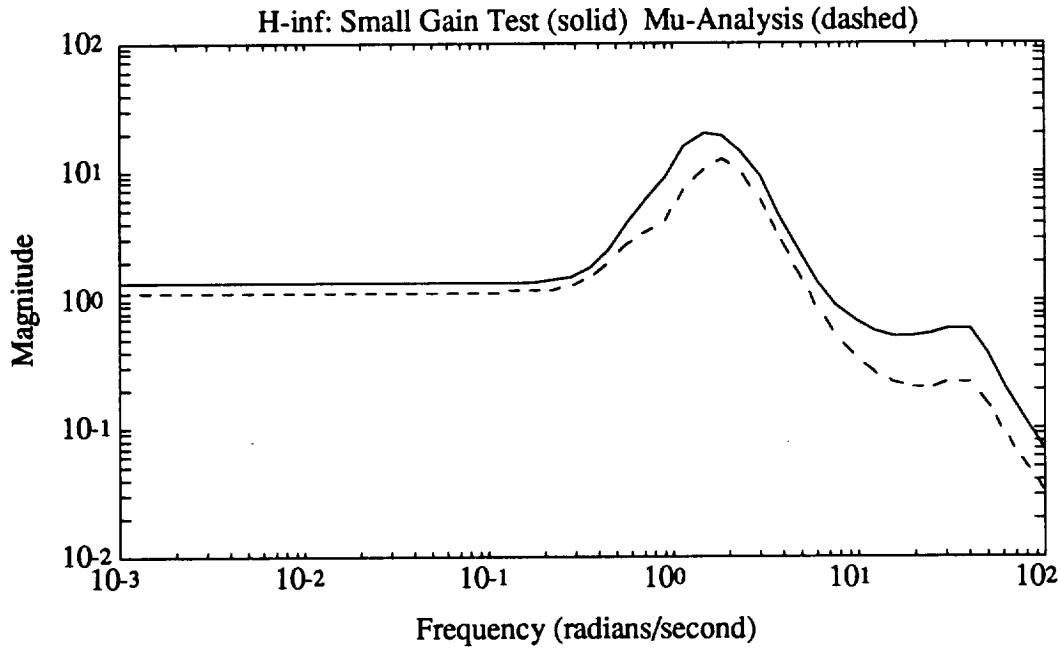


Figure 7.7. Robust Stability Analysis of the H_∞ System

examining robust stability; however the nature of our system leaves few options. Though the H_∞ system fails both stability robustness tests, let us examine the eigenvalues of the closed-loop system at certain endpoints of the parameters as before.

Figure 7.8 presents the near pole locations for the nominal closed-loop H_∞ system. The following four Figures show the closed-loop poles for the four sets of perturbed parameters. Figure 7.9 places both the K_{MA} and the K_G at their minimum values. Figure 7.10 places both sets of parameters at their maximum values. Figure 7.11 places the K_{MA} at their minimum values and the K_G at their maximum values. Finally, Figure 7.12 considers the last permutation of the K_{MA} at their maximum values and the K_G at their minimum values. Evaluating these sets of parameters for the closed-loop H_∞ design, as performed for the LQR and H_2 systems, shows conclusively that the system is indeed not robustly stable.

Aside from the nominal plant, the closed-loop system is only stable for system 2 shown in Figure 7.10. This is also the case for the H_2 system considered in Chapter 6. Similar to the H_2 plant, it is not possible to draw any conclusions for the H_∞ system about certain regions of operation that are causing instability since stability is a problem for several configurations.

If the stability problem was caused by neglected dynamics, a solution to robust stability

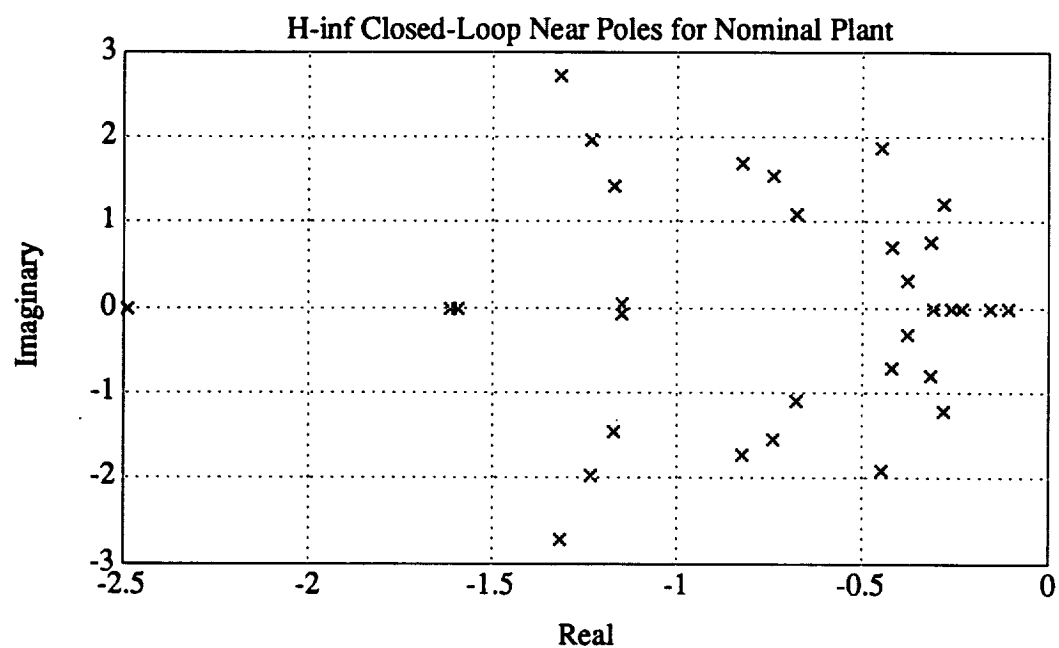


Figure 7.8. Closed-Loop Poles of the Nominal H_∞ System

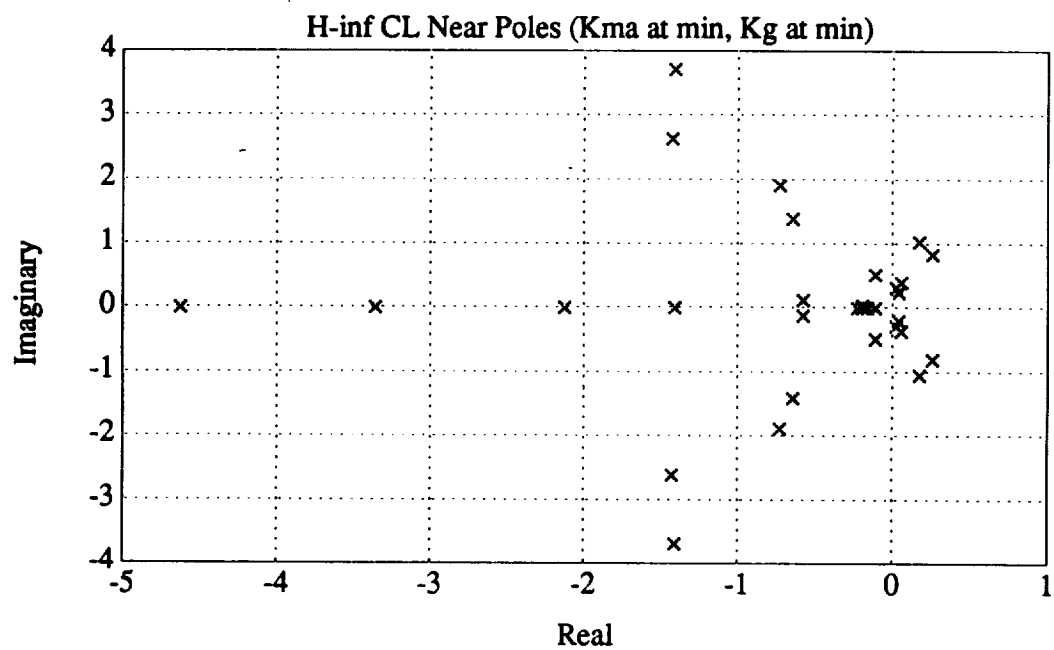


Figure 7.9. Closed-Loop Poles of the Off-Nominal H_∞ System: 1

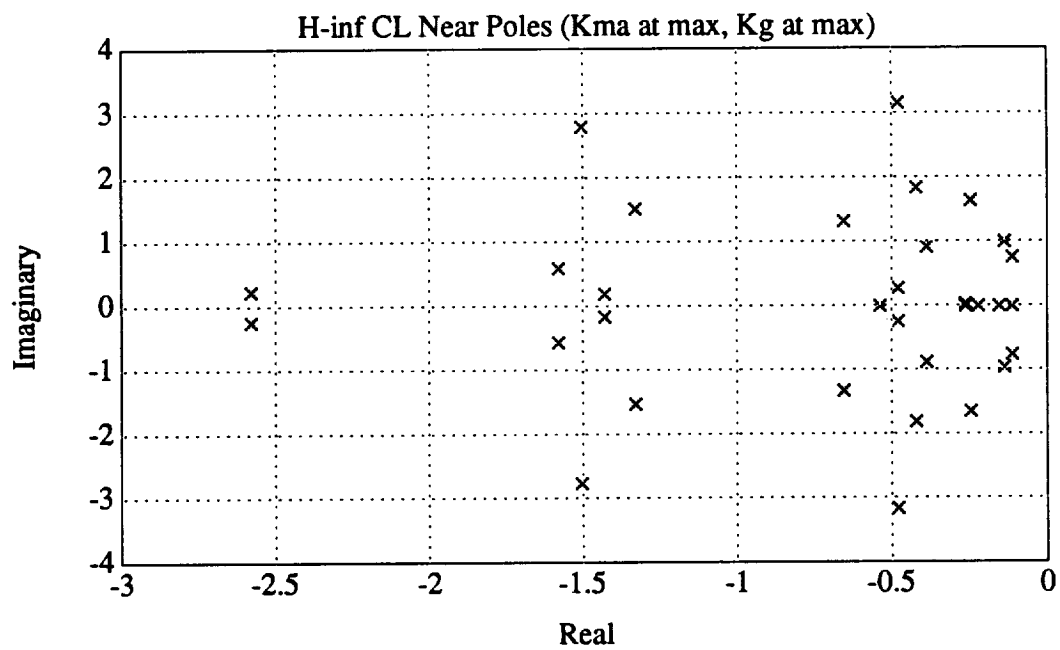


Figure 7.10. Closed-Loop Poles of the Off-Nominal H_∞ System: 2

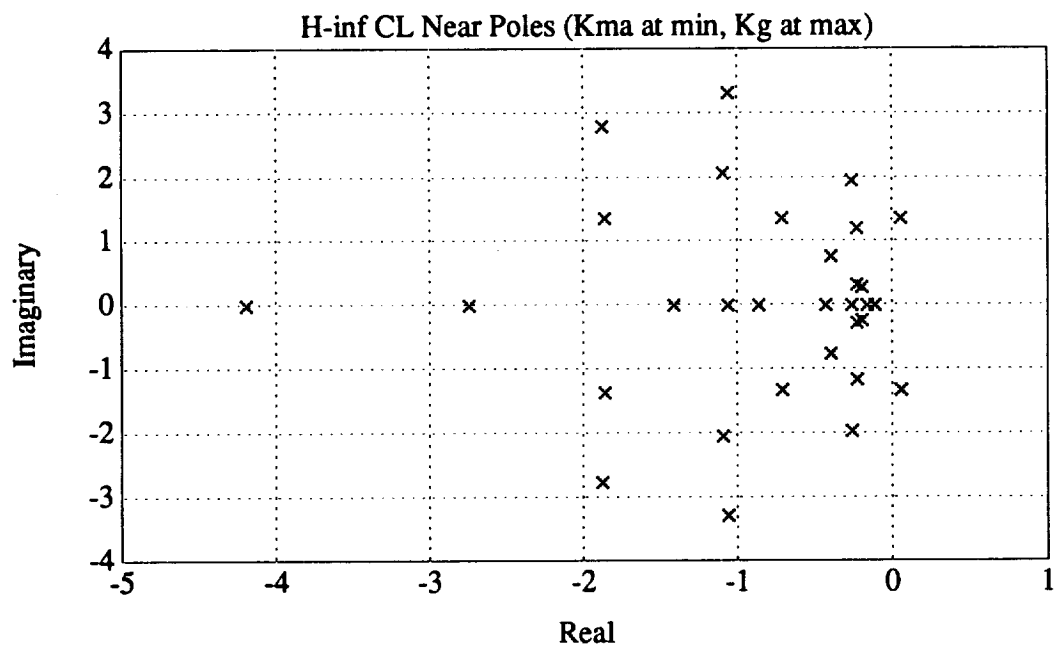


Figure 7.11. Closed-Loop Poles of the Off-Nominal H_∞ System: 3

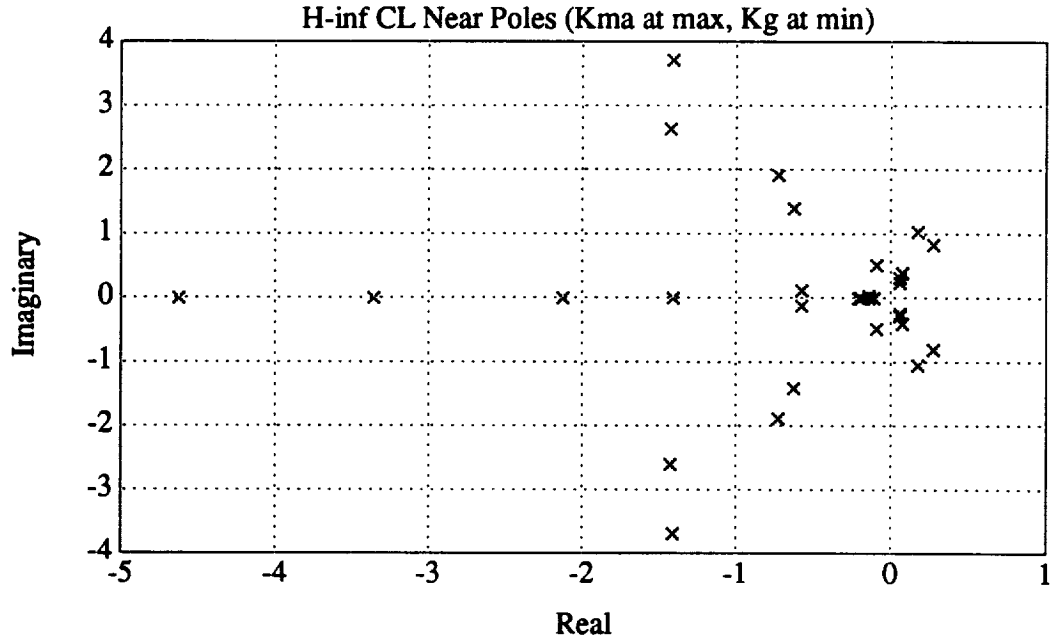


Figure 7.12. Closed-Loop Poles of the Off-Nominal H_∞ System: 4

would be to reduce the bandwidth of the system. Unfortunately, with parametric uncertainty the system poles simply aren't where the controller is expecting them. Reducing the bandwidth will not solve the problem. Chapter 4 shows that the open-loop system itself is not robustly stable in face of the parametric uncertainty present. Therefore even a zero as the transfer function for the controller will not stabilize the plant. However, using the H_∞ design process it is possible to design for robust stability directly to see if it is achievable for the SSAD plant.

Recall the general three block formulation shown in Figure 7.13 and its closed-loop representation shown in Figure 7.14. $G(s)$ is the closed-loop transfer function which combines the dynamics of the plant and the compensator. Recall that the closed-loop transfer function, $G(s)$, can be divided into a set of four transfer functions as follows,

$$\begin{bmatrix} \epsilon \\ e \end{bmatrix} = \begin{bmatrix} G_{11}(s) & G_{12}(s) \\ G_{21}(s) & G_{22}(s) \end{bmatrix} \begin{bmatrix} \eta \\ d \end{bmatrix} \quad (7.9)$$

Chapter 4 shows that if $\|G_{11}(s)\|_\infty < 1$, robust stability is achieved via the small gain test. Therefore, the H_∞ design process will design for robust stability directly with no consideration for performance if the input and error vectors are chosen such that the transfer function from d

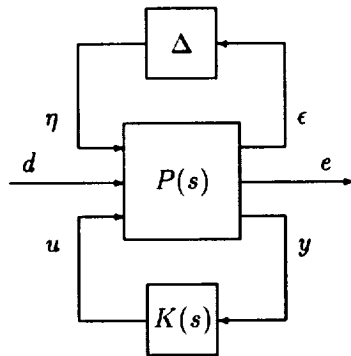


Figure 7.13. Standard Form for a Compensated Plant with Uncertainty

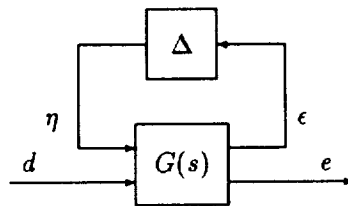


Figure 7.14. Closed-Loop Transfer Function

to e is $G_{11}(s)$. The H_∞ design methodology will try to minimize the H_∞ norm of this transfer function. If it can bring the maximum singular value below one, by the small gain test robust stability is guaranteed.

Before proceeding on this robust stability design, there is a subtlety to consider. In order to insure that the rank conditions outlined in Section 7.1 are not violated, the exogenous input vector, d , must include not only the output of the uncertainty block η , which replaces the process noise, but must also include the sensor noise. Similarly, the error vector e must include u as well as ϵ . These are conditions (c) and (d) from Section 7.1. Hence,

$$d = \begin{bmatrix} \eta \\ v \end{bmatrix} \quad e = \begin{bmatrix} \epsilon \\ u \end{bmatrix}$$

The subtlety is that if u is penalized by being included in the error vector, the ability to achieve robust stability is also penalized since it may require large amounts of control. Remember that for now, performance is not considered at all, the only concern is to see if any controller can robustly stabilize the system¹. Therefore, the design process to achieve a robustly stable compensator is to decrease the penalty on u until the maximum singular value of the closed-loop system falls below unity.

After decreasing the weight on the control channels to 10^{-10} , the plant starts to numerically fail the rank tests. Unfortunately, at this point the plant still fails to achieve robust stability. Figure 7.15 presents the results of both the small gain test and μ -analysis on this ' G_{11} ' H_∞ design. Though robust stability is not achieved, the curves are at their lowest levels out of every design, including the open-loop system. However, do not think of this system as less robustly unstable since robust stability is a binary test that this design fails. Even this attempt at robust stability has come at enormous cost.

Recall that this design gives basically no regard for performance whatsoever. Figure 7.16 shows the scaled singular values from disturbance to control effort. The joint rate limits have been exceeded by almost five orders of magnitude. Figure 7.17 presents the singular values from disturbance to end effector position and attitude. Clearly, the price is quite high in the effort to achieve robust stability. Unfortunately the goal is not even achieved.

¹The LQR system is robustly stable, but it requires full-state feedback

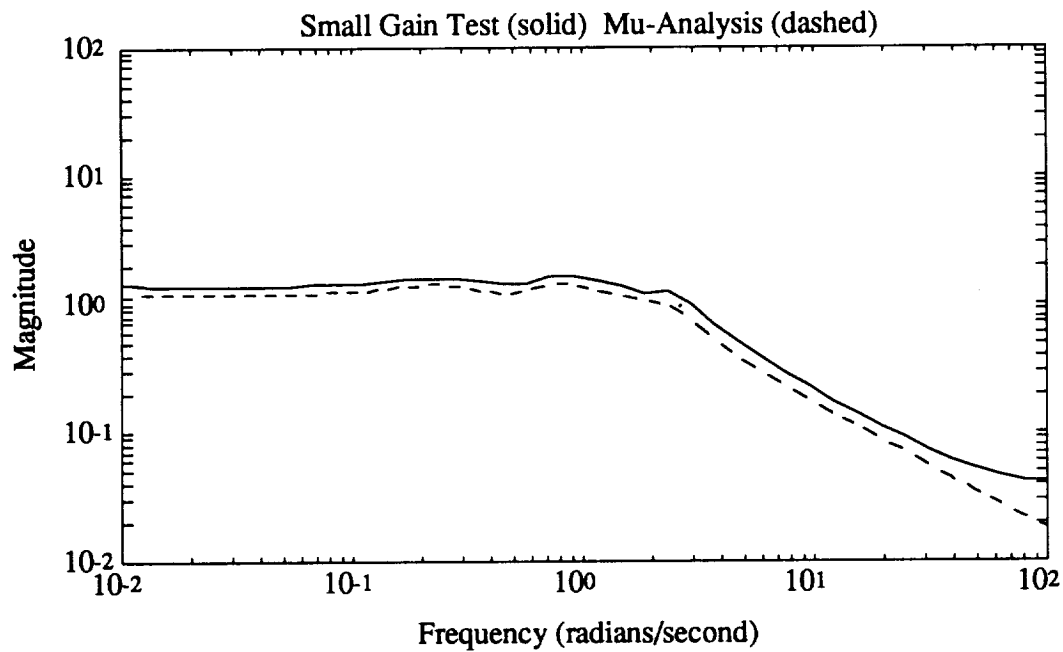


Figure 7.15. Robust Stability Analysis of the ' G_{11} ' H_∞ System

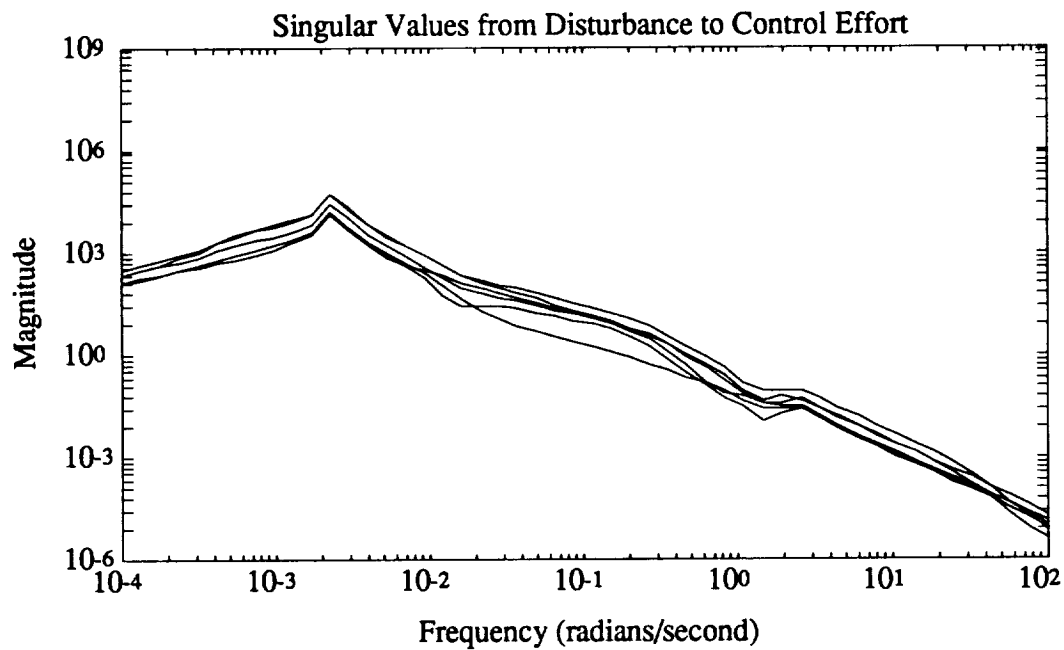


Figure 7.16. Control Effort Singular Values of the ' G_{11} ' H_∞ System

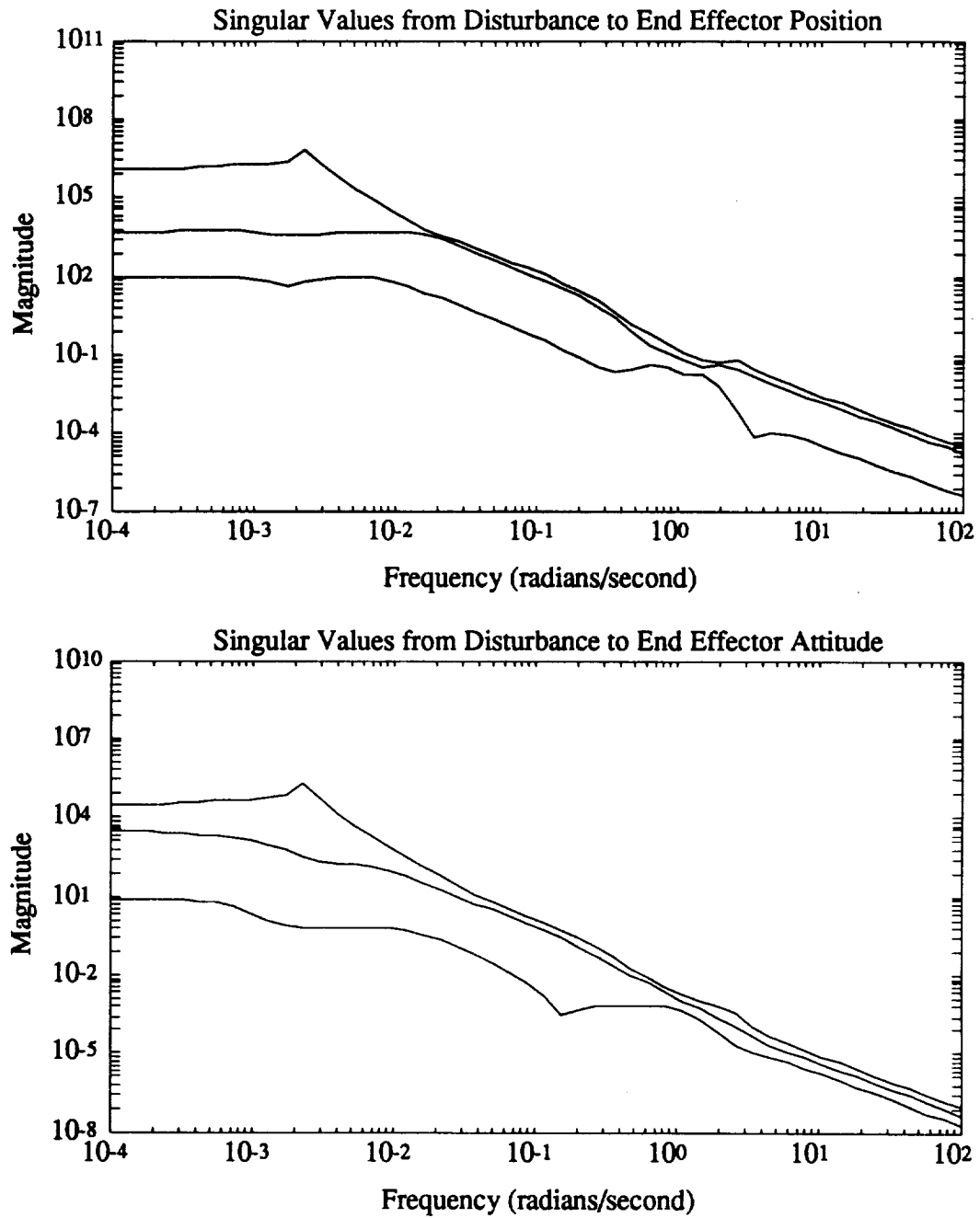


Figure 7.17. Performance Singular Values of the ' G_{11} ' H_∞ System

7.3 Summary

This Chapter presents a method for finding H_∞ optimal controllers that minimize, to a desired tolerance, the H_∞ norm of the transfer function from disturbance to error vector. This problem is closely related to the H_2 design process which is minimizing the H_2 norm of the same transfer function. Both techniques involve a two Riccati equation solution process. Both remove the requirement for full state feedback uncorrupted by noise called for in the LQR design.

With the H_∞ approach, on the nominal plant we are able to achieve performance better than the H_2 design. Performance is better in the sense that the worst case direction is of less magnitude than the H_2 design; however, this came at the expense of some of the other directions. Nevertheless, both performance objectives are met without exceeding the limits on the control effort.

Unfortunately the closed-loop H_∞ system, like the H_2 system, is not robustly stable in face of the parametric uncertainty present in the plant. As before both μ -analysis and the small gain test as well as actual eigenvalue analysis confirm the results. In an effort to achieve a robustly stable design, the problem is recast to minimize the H_∞ norm of the G_{11} transfer function. This essentially abandons all performance desires and tries only to achieve robust stability. This process fails to achieve robust stability as well.

Chapter 8

Conclusions

Three regulator designs were developed to improve the performance of the Space Shuttle Remote Manipulator System (SRMS). Designs focused on the Position Hold function of the SRMS. Position Hold is universal to normal operations of the SRMS. In Chapter 2, the SRMS system was examined in greater detail. A linear model of the nonlinear plant was developed in Chapter 3. Two of the significant nonlinearities were modelled as parametric uncertainties in an effort to capture their effect on the system. The linear model was compared to a higher fidelity nonlinear model in the time domain.

In Chapter 4, the characteristics of the open-loop plant were explored. Because of the numerical problems associated with six integrator poles, subsequent regulator designs used the current Position Hold system as the open-loop plant. In this manner, the current system moved the integrator poles off the $j\omega$ -axis. In effect, the new designs operate as stability and performance augmentation around the current system. Model reduction was applied to the new open-loop plant.

The performance and control effort of the open-loop system were presented in Chapter 4 as a baseline with which to compare subsequent regulator designs. The performance and control effort criteria were analyzed in the frequency domain by looking at three sets of singular values: disturbance to control effort, disturbance to end effector position, and disturbance to end effector attitude. A typical Shuttle attitude control jet firing pattern, which acts as a disturbance on the system, was simulated in the time domain.

Also in Chapter 4, a sufficient condition for robust stability was developed using the small gain theorem with an H_∞ norm. The structured singular value, μ , was defined and shown to

provide a necessary and sufficient condition for robust stability. In calculation, μ -analysis is reduced to a sufficient condition, but it is less conservative than the small gain test. Unfortunately these tests are conservative for lightly damped systems with real parametric uncertainties – the exact description of the SRMS model. Application of these tests on the current system determined it to be unstable. As confirmation, the eigenvalues of the system were calculated for certain values of the uncertain parameters. For conditions corresponding to low amplitude, slow motion, the current system was found to indeed be unstable. This corresponds to the slow, low amplitude limit cycling observed in the actual system.

A Linear Quadratic Regulator (LQR) was designed in Chapter 5. Its performance and control effort were a considerable improvement over the current system. Though the LQR failed both the small gain test, and μ -analysis, actual eigenvalue analysis seemed to indicate that the system may be robustly stable. Unfortunately this cannot be proved unequivocally. Since full-state feedback is not available on the SRMS, two model based compensators were designed.

In Chapter 6 the H_2 technique and in Chapter 7 the H_∞ technique were presented. There are many parallels between these two techniques. In both, an error vector is constructed from the controls and some linear combination of the states. As the name implies, the H_2 technique designs an optimal compensator that minimizes the H_2 norm of a transfer matrix using only the system measurements. Similarly, the H_∞ technique minimizes the H_∞ norm. Both designs were able to improve the performance of the nominal system considerably. However, neither design achieved robust stability. Not only did both designs fail the small gain test and μ -analysis, but actual eigenvalue analysis showed the systems were indeed not robustly stable.

In an effort to achieve a robustly stable design, In Chapter 7 the problem was recast to minimize the H_∞ norm of the G_{11} transfer function. By the small gain test, if the H_∞ norm of this transfer function falls below one, robust stability is assured. This essentially abandons all performance desires and tries only to achieve robust stability. Unfortunately, this process fails to achieve robust stability as well. This modified design did establish the trade-off present in the pursuit of robust stability at the expense of performance and control effort.

If the stability problem was caused by neglected dynamics, a solution to robust stability would be to reduce the bandwidth of the system. This could be accomplished by either further penalizing the control effort or reducing the weights on the end effector states, i.e., demand

less performance. Unfortunately, with parametric uncertainty the low frequency system poles simply aren't where the controller is expecting them. Reducing the bandwidth will not solve the problem. Considering the open-loop system itself is not robustly stable, even a zero for the compensator will not make the system robustly stable.

A possible extension for this thesis would be to gain schedule the controllers over certain regions of the nonlinearities. In this manner, the uncertainty of the parameters would be reduced allowing a family of controllers to be robustly stable over their respective regions. A 'real μ -analysis' technique would aid the design process allowing for the removal of conservatism in the gain scheduled controllers. Additionally, the model can be modified to incorporate acceleration sensors or optical measurements to provide for different measurements when NASA chooses a new sensor suite.

The SRMS model suffers from lightly damped poles that have large real parametric uncertainty. To achieve a single robustly stable design a 'real μ -synthesis' technique is needed. This technique must not only use the information of the structure of the uncertainty, but also account for exclusively real perturbations. The SRMS plant is an ideal candidate for a real μ -synthesis technique.

Bibliography

- [1] Gilbert, M.G., Scott, M.A. and Kenny, S.P., "Active Damping Application to the Shuttle RMS," *Fourth NASA/DOD CSI conf.*, Orlando, FL, 1990.
- [2] Ravindran, R. and Doetsch, K.H., "Design Aspects of the Shuttle Remote Manipulator Control," *Proceedings of the Guidance and Control Conference*, AIAA Paper No. 82-1581, 1982.
- [3] McLean, D.D. and Girling, K., *STS-3 Remote Manipulator System Press Kit*, SPAR Aerospace Limited, 1982.
- [4] Nguyen, P.K., Ravindran, R., Carr, R. and Gossain, D.M., "Structural Flexibility of the Shuttle Remote Manipulator System Mechanical Arm," *Proceedings of the Guidance and Control Conference*, AIAA Paper No. 82-1536, 1982.
- [5] Logan, B.A., Jr., "Shuttle Payload Deployment and Retrieval System," *Proceedings of the Guidance and Control Conference*, AIAA Paper No. 82-1580, 1982.
- [6] Newsom, J.R., Layman, W.E., Waites, H.B. and Hayduk, R.J., "The NASA Control-Structures Interaction Technology Program," *Proceedings of the 41st Congress of the International Astronautical Federation*, IAF Paper No. 90-290, 1990.
- [7] Barrows, T.M., *A Simplified Simulation for the Analysis of Heavy Payloads on the Shuttle Remote Manipulator Arm*, Charles Stark Draper Laboratory Report CSDL-R-1730, 1984.
- [8] Barrows, T.M., *A Simplified Simulation for the Analysis of RMS Motion with Heavy Payloads*, Charles Stark Draper Laboratory Memo TMB-84-2, 1984.

- [9] Barrows, T.M., *Development of LSAD-II, an Efficient Simulation for Computing the Motion of Heavy Payloads on the Shuttle RMS*, Charles Stark Draper Laboratory Memo DI-85-6, 1985.
- [10] Taylor, E.C., *Analytical Solution to Remote Manipulator System Joint Servo Model*, McDonnell Douglas Technical Services Co., Design Note No. 1.4-D1143-001, Houston Astronautics Division, 1979.
- [11] Appleby, B.D., "Robust Estimator Design Using the H_∞ Norm and μ Synthesis," Ph.D. Thesis, Dept. of Aero. and Astro., MIT, 1990.
- [12] Maciejowski, J.M., *Multivariable Feedback Design*, Addison-Wesley, 1989.
- [13] Stein, G., Athans, M., "The LQG/LTR Procedure for Multivariable Feedback Control Design," *IEEE Transactions on Automatic Control*, AC-32, 1987.
- [14] Safonov, M.G., Jonckheere, E.A., Verma, M., Limebeer, D.J.N. "Synthesis of Positive Real Multivariable Feedback Systems," *Int. J. Control*, vol. 45, no. 3, pp.817-842, 1987.
- [15] Doyle, J.C., "Analysis of Feedback Systems with Structured Uncertainties," *IEEE Proc.*, vol. 129, pp. 242-250, 1982.
- [16] Kwakernaak, H., Sivan, R., *Linear Optimal Control Systems*, Wiley-Interscience, 1972.
- [17] Doyle, J. C., Glover, K., Khargonekar, P., and Francis, B. A., "State-Space Solutions to Standard H_2 and H_∞ Control Problems," *IEEE Transactions on Automatic Control*, vol. AC-34, no. 8, pp. 831-847, 1989.
- [18] Francis, B. A., "A Course in H_∞ Control Theory," (Lecture Notes in Control and Information Sciences, Vol.88). New York: Springer-Verlag, 1987.
- [19] Glover, K., Doyle, J. C., "State-Space Formulae for all Stabilizing Controllers that Satisfy an H_∞ -norm Bound and Relations to Risk Sensitivity," *Systems and Control Letters*, vol. 11, pp. 162-172, 1988.

